STUDYING SURFACE PLASMONS OF INDIVIDUAL GOLD NANOPARTICLE ON SILICON SUBSTRATE USING CATHODOLUMINISCENCE

by

Arpan Maiti

(Enrolment No.-PHYS05201204008)

Saha Institute of Nuclear Physics, Kolkata

A thesis submitted to the

Board of Studies in Physical Sciences

In partial fulfillment of requirements

for the degree of

DOCTOR OF PHILOSOPHY

of

HOMI BHABHA NATIONAL INSTITUTE

July, 2017

Homi Bhabha National Institute

Recommendations of the Viva Voce Committee

As members of the Viva Voce Committee, we certify that we have read the dissertation prepared by ARPAN MAITI entitled "STUDYING SURFACE PLASMONS OF INDIVIDUAL GOLD NANOPARTICLE ON SILICON SUBSTRATE USING CATHODOLUMINISCENCE" and recommend that it may be accepted as fulfilling the thesis requirement for the award of Degree of Doctor of Philosophy.

Chairman - Prof. Krishnakumar S.R. Menon	**Date:** 10.10.2017
Guide / Convener - Prof. Tapas Kumar Chini	**Date:** 10.10.2017
Co-guide - NA	**Date:**
Examiner - Dr. G.V. Pavan Kumar	**Date:** 10th Oct 2017
Member 1- Dr. Biswarup Satpati	**Date:** 10/10/2017
Member 2- Prof. Supratic Chakraborty	**Date:** 10/10/17

Final approval and acceptance of this thesis is contingent upon the candidate's submission of the final copies of the thesis to HBNI.

I/We hereby certify that I/we have read this thesis prepared under my/our direction and recommend that it may be accepted as fulfilling the thesis requirement.

Date: 10.10.2017

Place: Kolkata

Co-guide (if applicable)

Guide

STATEMENT BY AUTHOR

This dissertation has been submitted in partial fulfillment of requirements for the doctoral degree at Homi Bhabha National Institute (HBNI) and is deposited in the Library to be made available to borrowers under rules of the HBNI.

Brief quotations from this dissertation are allowable without special permission, provided that accurate acknowledgement of source is made. Requests for permission for extended quotation from or reproduction of this manuscript in whole or in part may be granted by the Competent Authority of HBNI when in his or her judgment the proposed use of the material is in the interests of scholarship. In all other instances, however, permission must be obtained from the author.

Arpan Maiti

DECLARATION

I, hereby declare that the investigation presented in the thesis has been carried out by me. The work is original and has not been submitted earlier as a whole or in part for a degree / diploma at this or any other Institution / University.

Arpan Maiti

List of Publications arising from the thesis

Publications in peer reviewed Journals

1. *Mode Mixing and Substrate Induced Effect on the Plasmonic Properties of an Isolated Decahedral Gold Nanoparticle.*
   A. Maiti, A. Maity, and T. K. Chini, *J. Phys. Chem. C*, **2015**, 119, 18537–18545.

2. *Efficient Excitation of Higher Order Modes in the Plasmonic Response of Individual Concave Gold Nanocubes.*
   A. Maiti, A. Maity, B. Satpati, N. Large, and T. K. Chini, *J. Phys. Chem. C*, **2017**, 121, 731–740 .

3. *Plasmonic Response of Individual Gold Nano-Octahedron using Cathodoluminescence Spectroscopy and Imaging.*
   A. Maiti, A. Maity, and T. K. Chini, *Adv. Sci. Lett.* **(Accepted for publication.)**.

In conference proceedings:

1. *Plasmonic Behavior of Gold Nanorod Heterodimers with Free-Electron Feed.*
   A. Maiti, A. Maity, and T. K. Chini, *AIP Conf. Proc.*, **2015**, 1665, 080011.

Arpan Maiti

Dedicated to my "Family"

Acknowledgements

The research included in this dissertation could not have been performed without the assistance, patience, and support of many individuals. First and foremost, I thank my thesis supervisor Prof. Tapas Kumar Chini for introducing me to the exciting research area of plasmonics. He has always given me constant inspiration and encouraged me to pursue my own line of thinking throughout my PhD period. This research work would not have been possible without the sincere help and support from him. Thank you so much Tapas-da.

I gratefully acknowledge Dr. Biswarup Satpati for his help in TEM study and fruitful discussions. I would like to thank all the other professors and staff of surface physics and material science division for their guidance and help during the entire period of my research.

I must thank my senior Pabitrada for sharing his knowledge and insights in first one year of my research. I have learned so many things from him in the field of my research. I would like to thank Lumerical support team of FDTD simulations for their constant technical support. I thank Prof. Nicolas Large of University of Texas for his insight and inputs on my work. I acknowledge the help I got from Prof. Dulal Senapati and his group of our chemical science division, during the initial stages of chemical synthesis. I also thank Qingfeng Zhang and Dr. Hui Wang from the University of South Carolina for useful discussions regarding synthesis of concave nanocubes.

I would like to thank the Department of Atomic Energy (DAE), Government of India for the financial support. I thank my doctoral committee members in making yearly evaluation of my progress report and giving valuable suggestions.

Heartily thanks to my lab mate Achyut, for being a part of this five year journey. I will always remember the fruitful discussion and valuable efforts from Achyut which led many experiments to success. I would also like to thank my friends, seniors and juniors of SPMS division, as well as other students in the institute with whom I have shared invaluable moments.

I would like to express my extreme sincere gratitude to my family for the support they

provided me through my entire life. I am thankful to my parents for providing me the moral and emotional support. Without their kind blessings, I could not complete this work. I very fondly acknowledge my elder brother and his sweet wife for their love and support. I am thankful to my best friend, my better half Moumita who give me strength, happiness, support and encouragements to overcome all the doubts and difficulties. Thank you very much Mou for your love, support and understanding. Without your love, support and understanding I could never have completed this doctoral degree. Thanks to all other members of my family including parent in law, sister and brother in law, little Biva (their daughter) for the wonderful memories whenever I'm at home. I sincerely thank my elder cousin Somadi, cousin in law Buddhada, little Arin (their son) and all other relatives who were with me for their love and encouragement.

Lastly, I want to express my sincere apologies for my inability to individually acknowledge many others, who might have helped me in the completion of this Ph.D. work one way or another.

SINP, Kolkata

July, 2016 Arpan Maiti

Contents

Synopsis

In recent years, remarkable developments in synthesis techniques have led to the fabrication of a large variety of new nano-objects with properties that strongly depart from those of their bulk counterparts. Among them noble metal nanoparticles (MNPs) with sizes close to or smaller than the typical wavelength of light in the visible range, have attracted significant interest in the area of photonics research because of its' huge scientific and practical relevance. Rapidly growing interests in MNPs have been based largely on their vivid optical properties (strong light absorption and scattering ability within the visible and near-infrared range of the spectrum), which comes from their ability to sustain surface plasmons (SPs) or more specifically localized surface plasmons (LSPs) [1]. LSPs are originated from the resonant interaction between the surface charge oscillation of metals and the external electromagnetic (EM) field of the light or electron beam. During this interaction free electrons of MNPs respond collectively by oscillating in resonance with the external EM wave. LSPs, when excited resonantly by the electromagnetic (EM) wave (either light wave or evanescent wave associated with first moving electrons), can lead to a large amount of local EM field enhancement around NP's surface. A similar enhancement is also occurred at the far field due to the scattering phenomena. These enhanced EM fields can be used in wide variety of applications such as waveguiding [2], surface-enhanced Raman scattering (SERS) [3], sensing [4], photovoltaics [5], catalysis [6], and medical diagnostics [7]. Often the local EM field enhancement in the plasmonic structures is confined spatially on length scale of $\sim$ 10–50 nm and varies strongly with the morphology and composition of NPs. Consequently, experimental access to the EM field distribution associated with nanoparticle SPs, with sufficient degree of spectral and spatial resolution is very much important.

The LSP resonance (LSPR) frequency of a NP is easily influenced by the adjacent particles, meaning, the usually adopted optical imaging techniques, such as UV-VIS spectroscopy or dark-field microscopy (DFM) that measure the optical properties of the collection of particles at a time is not expected to reflect the spectral feature of an individual entity. Consequently, investigation of the EM field distribution associated with LSP requires an experimental probe not only of sufficient spectral resolution but also of sufficient degree of spatial resolution from an application point of view as well as to understanding the light matter interaction at the nanometer level. In this

regard, electron beam based spectroscopy such as electron energy loss spectroscopy (EELS) in transmission electron microscope (TEM) or cathodoluminescence (CL) in a scanning/transmission electron microscope (SEM/TEM) has shown to be an an excellent probe of plasmons that allows capturing even sub nanometer resolution information in the spatial domain [8, 9]. The advantage of doing CL in a SEM is that a large sample area on a thick substrate can be accessed without any special sample preparation step, such as maintaining electron transparency (< 100 nm) as is used in TEM.

The present thesis is devoted to the experimental study of the LSPR induced optical properties of single MNPs in high resolution spectral and spatial domain. We have used anisotropic (non-spherical) gold (Au) NPs with decahedron, concave nanocube (CNC) shape morphology because their inherent optical anisotropy and highly localized plasmon modes are important in biosensing application. The optical properties of these nanostructures are characterised by CL technique. The CL technique is implemented here by combining a spectrometer (monochromator + high sensitivity photo multiplier tube (HSPMT) as light detector) with a scanning electron microscope (SEM). The focused electron beam from SEM is either scanned over the sample or positioned on a desired spot and CL image is recorded by using an emitted light signal with the simultaneous recording of secondary electron image using the emitted secondary electrons (SEs). So, in addition to the routinely available morphological information from SE imaging, site-specific spectroscopy and photon-mapping make CL-SEM an ideal tool for studying optical properties of individual nanostructures or assembly of nanoparticles located on the top surface of a substrate. We analyse our experimental data using Finite-difference time domain (FDTD) simulations.

CL from metallic nanostructures relies upon the fact that energy of incident electrons is coupled to the plasmon modes of the NPs and these in turn decay into radiative photons that can be collected into far-field. High spatial nanometer resolution CL of individual nanostructures can be achieved with focused electron beams. The resulting CL images provide direct information of the wavelength dependent local density of optical states (LDOS)[8] of the imaged individual plasmonic nanostructures. Mapping the spatial variation of the photon emission is a direct probe of the LSP modes and, consequently, provides a direct way to map the near-field properties. The near-field scanning optical microscopy (NSOM) technique [10] can also achieve

sub-diffraction-limited optical imaging, but is constrained by the requirement of fabricating very sharp tips and suffers from tip-sample interaction which affects the signal of interest. However, CL detects the radiative modes without perturbing the local environment, which makes CL-SEM a powerful tool for direct analysis of the LDOS at the single nanoparticle level. Our main object is to directly visualize the spatial profile of the localized surface plasmon resonance modes of anisotropic noble metal (as for example Au) nanoparticles with special emphasis on the higher order modes. This is because of investigation and identification of higher-order surface plasmon modes are important from fundamental understanding and application point of view [11, 12]. However, identifying the higher order LSPR modes from these anisotropic nanoparticles in spectral and spatial domain are not trivial. Identifying the signature of higher order LSPR modes of these anisotropic NPs has been one of the concerns of the present thesis.

The LSPR frequency of MNPs can be tuned by varying their size, shape, composition, and local dielectric environment [4, 13]. The local dielectric environment, in particular, the presence of substrate [4] plays an important role in the plasmonic property of MNPs. As for example, when a MNP is immersed in a homogeneous dielectric medium, the local dielectric environment is symmetric, but when the MNP is placed on a substrate, the symmetry is broken, leading to strong modifications of the plasmonic response of the MNP, such as mode splitting. In this thesis we have shown that the presence of silicon (Si) substrate has a big role in the observed plasmonic modes of anisotropic Au nanoparticles (Decahedron, concave nanocube).

Decahedron or pentagonal bi-pyramid shaped nanostructure has drawn substantial attention due to their inherent well defined anisotropy characterized by the presence of several sharp edges, corners and two acute apexes that are favourable regions of concentrating high EM field under external excitation. So far most of the experimental studies of Au decahedral particle show clear existence of two dipolar LSP modes, one along the azimuthal (along pentagonal base) and the other along the polar direction (along 5 fold symmetry axis). However decahedron nanoparticle of size larger than 150 nm have neither been explored experimentally using local electron probe nor discussed in detail by electrodynamics based numerical simulations. Here, we performed site specific CL spectroscopy and imaging(Figure 1) in a field emission gun SEM to study plasmonic response of an isolated single Au decahedron of side

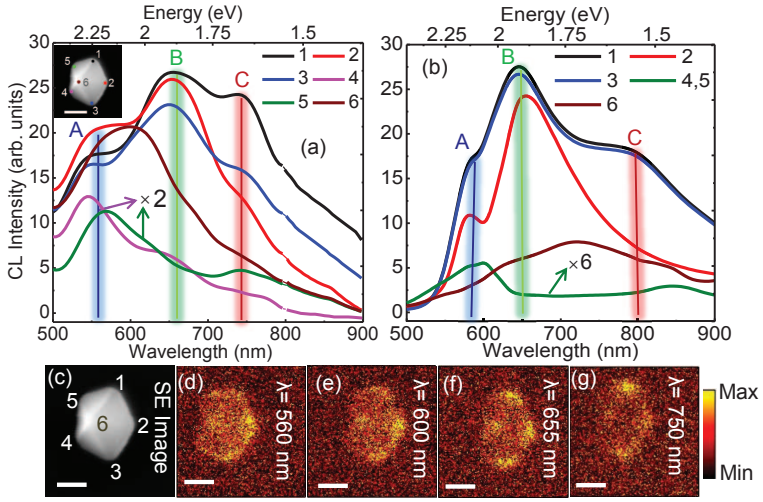

Figure 1: *(a) Experimentally obtained CL spectra from different beam injection positions (marked as 1, 2, 3...6) of the decahedron. The inset SE image shows the e-beam impact points with different colored dots. (b) 3D-FDTD simulated CL spectra of the same morphology as shown in the inset of (a). (c) The SE image of the gold decahedron and the corresponding monochromatic CL maps for the selected resonance wavelengths (d) 560, (e) 600, (f) 655, and (g) 750 nm. The scale bar in all the images is 200 nm.*

edge length (L)∼ 230 nm that is tilted by an angle 40° on a Si substrate. We found that the spectral peak intensity and peak position is very much dependent on the position of the electron beam as shown in Figure 1a. For electron beam position on point 1, we observe three resonant peaks (mode A, mode B and mode C). However for excitation over point 2, which is farthest base corner point from the substrate (Si), we found only two noticeable resonance peak (mode A and mode B). Our experimental observation is well supported by theoretically simulated CL spectrum (Figure 1b). Also monochromatic photon maps were taken at these resonance wavelength as shown in Figure 1(d)-(g). The monochromatic CL image corresponding to mode A at 560 nm (Figure 1d) shows intensity maximum along the edge whereas photon map corresponding to mode B at 655 nm (Figure 1f) shows maximum luminescence coming from the pentagonal base corner points. Also photon maps at these two modes (mode A and mode B) reveal (Figure 1d,f) a considerable luminescence from tip apex (point 6) which is also consistent with our spectroscopic data (Figure 1a). This means there might be a mode mixing (existence of transverse as well as longitudinal

mode at the same wavelength) occurring in these two modes (mode A and B). On the otherhand monochromatic photon maps corresponding to mode C at 750 nm gives rise to maximum photon emission coming from pentagonal base corner point 1 than any other point which is consistent with our spectroscopic data of Figure 1a. Also it is interesting to note that almost no photon is emitted from corner points 4 and 5. This is due to the fact that LSPR induced radiation from these two corner points are absorbed by the high index substrate (Si) (as these corner points are in touch with the substrate) resulting a reduction in the amount of light in CL detector. In order to understand the modal distribution of different resonant modes and to explore the effect of substrate, we have also performed FDTD simulations. We found that mode A has a mixture of in-plane quadrupolar and out-of-plane quadrupolar charge distribution pattern, whereas mode B has the dipolar charge pattern in both the direction. We also analyze that such mode mixing occurs at a critical side edge length 130 nm of gold decahedron by systematic numerical simulation using FDTD [14]. We also show that mode C is related to substrate induced mode.

In this thesis we have also investigated plasmonic response of individual Au con-

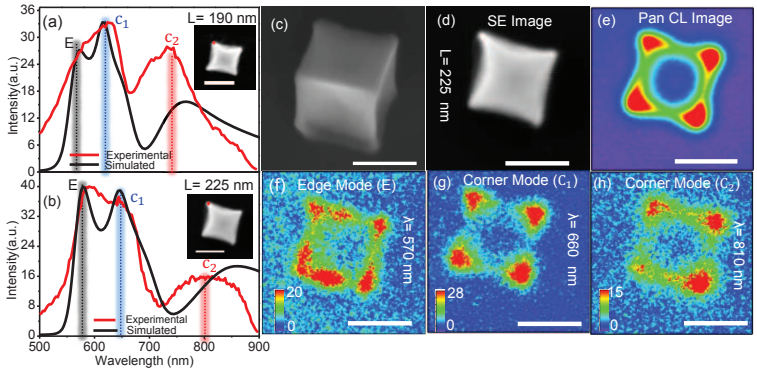

Figure 2: *(a, b) Experimental (red) and calculated (black) CL spectra for Au CNC of side edge length L = 190 and 225 nm, respectively. Beam impact position is indicated by the red colored dot on the inset SEM images. (C) Stage-tilted SEM image of the CNC which clearly shows square pyramid-shaped depressions at the centre of each facets of the CNC. (d) SE image of the CNC (edge length 225 nm) and corresponding pan CL (e) and mono CL images (f-h) of the CNC for different resonant wavelength. Scale bar is 200 nm in all the cases.*

cave nanocubes (CNCs). CNC shaped metal nanoparticles (MNPs) with high index facets have drawn special attention due to their high chemical activity and large electromagnetic (EM) field enhancements, making them good candidates for multi-functional platforms. However, most of the previously published works focused on the plasmonic properties of silver simple nanocubes of smaller dimension, i.e., within the quasi-static limit, hardly supporting efficient excitation of high-order plasmonic modes. Here, we explore the localized surface plasmon modes of the Au CNCs with relatively larger size than previously studied nanocubes. Using CL-SEM spectroscopy and imaging and employing finite-difference time-domain (FDTD) numerical simulations, we study of the plasmonic properties of individual gold CNCs with edge length of 170, 190, and 225 nm dispersed on a Si substrate. We found three prominent LSPR peaks (Figure 2(a,b)) in the substrate supported CL spectra of CNC which red shifts with increase in particle size. In addition to the panchromatic photon map (Figure 2(e)) of the CNC (edge length 225 nm) we also performed wavelength selected CL imaging (Fig.1f-h) of the three observed radiative LSP modes. The spatial variation of the intensity distribution (Figure 2(f-h)) of luminescence shows not only a strong localization of the radiative modes at the corner points but also its extension along the edges of the CNC. We show that while the corner modes are always present, the edge mode appears to be stronger with increased particle size and is associated with large EM field enhancement at the Au CNC's top surface-vacuum interface. Using FDTD simulations, we have explicitly shown that substrate plays an important role to visualize the observed LSPR modes [15]. Direct comparison of the CL and calculated spectra using FDTD numerical simulation reveals that the substrate-induced splitting of a mode generates two hybridized mode, namely, corner octupolar (mode C_1) and corner quadrupolar (mode C_2) plasmon in addition to a quadrupolar edge mode (mode E). Furthermore, we show that the edge quadrupolar mode becomes prominent with increasing concaveness, thus opening up a new way of engineering the LSP modes [15].

In summary, the experimental methodology and numerical formalism presented in this thesis, could be used to investigate a wide range of nanoparticle geometries and associated surface plasmon modes thus giving insight into the light matter interaction at nanometer scale and may help to improve the design of new plasmonic devices.

Bibliography

[1] S.A. Maier, *Plasmonics: Fundamentals and Applications.* (Springer Science+ Business Media, 2007).

[2] S. A. Maier, P. G. Kik, H. A. Atwater, S. Meltzer, E. Harel, B. E. Koel, and A. A. Requicha, Nat. Mater. **2**, 229 (2003).

[3] B. Sharma, R. R. Frontiera, A.-I. Henry, E. Ringe, and R. P. Van Duyne, Mater. Today **15**, 16 (2012).

[4] S. Zhang, K. Bao, N. J. Halas, H. Xu, and P. Nordlander, Nano Lett. **11**, 1657 (2011).

[5] H. A. Atwater and A. Polman, Nat. Mater. **9**, 205 (2010).

[6] H. Jing, Q. Zhang, N. Large, C. Yu, D. A. Blom, P. Nordlander, and H. Wang, Nano Lett. **14**, 3674 (2014).

[7] N. L. Rosi and C. A. Mirkin, Chem. Rev.**105**, 1547 (2005).

[8] F. J. García de Abajo, Rev. Mod. Phys. **82**, 209 (2010).

[9] M. Kociak and O. Stéphan, Chem. Soc. Rev. **43**, 3865 (2014).

[10] R. M. Bakker, A. Boltasseva, Z. Liu, R. H. Pedersen, S. Gresillon, A. V. Kildishev, V. P. Drachev, and V. M. Shalaev, Opt. Express **15**, 13682 (2007).

[11] Z. Yong, D. Y. Lei, C. H. Lam, and Y. Wang, Nanoscale Res. Lett. **9**, 1 (2014).

[12] Y. A. Akimov, W. S. Koh, and K. Ostrikov, Opt. Express **17**, 10195 (2009).

[13] E. Ringe, J. M. McMahon, K. Sohn, C. Cobley, Y. Xia, J. Huang, G. C. Schatz, L. D. Marks, and R. P. Van Duyne, J. Phys. Chem. C **114**, 12511 (2010).

[14] A. Maiti, A. Maity, and T. K. Chini, J. Phys. Chem. C **119**, 18537 (2015).

[15] A. Maiti, A. Maity, B. Satpati, N. Large, and T. K. Chini, J. Phys. Chem. C **121**, 731 (2017).

List of Figures

Chapter 1

General introduction

This chapter describes the basic aspects of localised surface plasmon (LSP) induced luminescence from metal nanoparticles and the application of a local probe luminescence technique like Cathodoluminescence (CL) to probe site specific luminescence property of gold nanoparticles with nanoscale spatial resolution.

1.1 Introduction

Nanoparticles have attracted huge interest in recent years due to their unusual properties that strongly depart from those of their bulk counterparts. Among various nanostructures, noble metal nanoparticles (MNPs) with sizes close to or smaller than the typical wavelength of light in the visible range, have drawn special attention because of their strong light absorption and scattering ability within the visible and near-infrared range of the spectrum. This unique ability shown by the MNPs is due to the fact that they can sustain surface plasmons (SPs) or more specifically localized surface plasmons (LSPs). They are originated from the resonant interaction between the surface charge oscillation of metals and the external electromagnetic (EM) field of the light or electron beam. During this interaction free electrons of MNPs respond collectively by oscillating in resonance with the external EM wave [1–3].

At localised surface plasmon resonance (LSPR) condition, a large amount of field enhancement occur at a sub-diffraction limited length scale, causing a highly intense EM field around the surface of the MNPs. This enhanced local EM fields are evanescent in character, i.e., falling exponentially with the distance away from the MNP and have important role for the enhancement of Raman signal in SERS, in enhanced fluorescence used in bio-sensing and in the enhanced photo-carrier generation applicable to photovoltaics. Often the local EM field enhancement in the plasmonic structures is confined spatially on length scale of $\sim$ 10–50 nm and varies strongly with the morphology and composition of NPs. Consequently, investigation of the EM field distribution associated with LSP requires an experimental probe not only

of sufficient spectral resolution but also of sufficient degree of spatial resolution from an application point of view as well as to understanding the light matter interaction at the nanometer level.

For the case of MNPs, when an energetic e-beam passes near the vicinity of the nanoparicle, it will excite LSPs of the particle, which can decay radiatively, thus contributing to cathodoluminescence (CL) signal. CL is analogous to photoluminescence (PL). The nomenclature differs only through source of excitation. While PL is excited by photons, CL is triggered by fast moving electron beam providing an ideal local probe for LSP related optical studies.

The present thesis is devoted to the experimental study of the LSPR induced optical properties of single MNP in high resolution spectral and spatial domain. The experimentally obtained spectro-microscopy data are analysed using detailed electromagnetic based numerical simulation. The methodology of the combination of experiment and simulation provides information on the modal distribution of different LSPR modes along with nearfield intensity distribution and the effect of substrate on mode splitting.

The CL technique is implemented here by combining a spectrometer (monochromator + high sensitivity photo multiplier tube (HSPMT) as light detector) with a scanning electron microscope (SEM). The focused electron beam from SEM is either scanned over the sample or positioned on a desired spot and CL image is recorded by using an emitted light signal with the simultaneous recording of secondary electron image using the emitted secondary electrons (SEs). So, in addition to the routinely available

morphological information from SE imaging, site-specific spectroscopy and photon-mapping make CL-SEM an ideal tool for studying optical properties of individual nanostructures or assembly of nanoparticles located on the top surface of a substrate. We have used anisotropic (non-spherical) gold (Au) NPs with decahedron, octahedron and concave nanocube shape morphology because their inherent optical anisotropy and highly localized plasmon modes are important in biosensing application.

1.2 Motivation

1.2.1 Surface plasmon enhanced optical properties of MNP

Noble MNPs have long been used for their bright and fascinating colors giving for example coloring pigments in stained glass windows (Figure 1.1(a)) of medieval Europe and in the Lycurgus Cup (Figure 1.1(b,c)). The Lycurgus Cup is a 4th-century Roman glass cage cup, which changes color depending on the direction of illumination. The cup appears green in reflection (Figure 1.1(b)), while during transmission it shows a reddish color (Figure 1.1(c)). The actual science behind the coloration of the Lycurgus cup was not known at that time. Nowadays, it is well established that the coloration of the Lycurgus Cup is caused by the excitation of SPs of the metallic nanoparticles embedded into the glass. The existence of SPs was first predicted in 1957 by Rufus Ritchi [4] and then Heinz Raether, E. Kretschmann, A. Otto, and many other scientists studied SPs very extensively. SPs or more specifically surface plasmon polaritons (SPP) are propagating, transverse EM waves that are trapped on the surface because of their interaction with the free electrons of the conductor [3]. On the otherhand localized surface plasmons (LSPs) or particle plasmons are

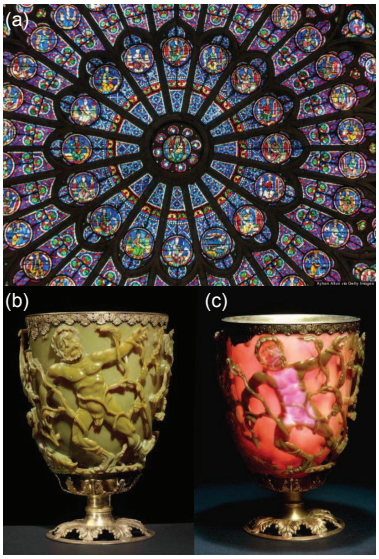

Figure 1.1: *(a) stained glass windows in Cathedral and churches of medival Europe. Roman Lycurgus Cup (British Museum, 4th century A.D.): (b) illuminated from outside (reflection) appears in greenish color and (c) illuminated from inside (transmission) appears in redish color. Image courtesy: Internet*

non-propagating collective excitations of the free-electron gas supported by MNPs. LSPs, when excited resonantly by the EM wave (either light wave or evanescent wave associated with first moving electrons), can lead to a large amount of local EM field enhancement around NP's volume having a dimension of only 10-50 nm (that is well below the diffraction limit of light) in the x,y,z direction. These enhanced EM fields, along with the large scattering cross-sections, can be used in wide variety of applications such as surface-enhanced Raman scattering (SERS) [5–11], sensing [12, 13], enhanced fluorescence [14], photovoltaics [15–17], catalysis [9, 18], enhanced photocarrier generation [17], optical trapping [19, 20], waveguiding [21–23], and medical diagnostics [24]. After the discovery, SPs have been engineered into a variety of

resonant geometries that exploit their spectral tunability, enhanced local fields, and controllable absorption for a new generation of optical research and applications. A new field of photonic research termed as 'plasmonics' has emerged which deals with routing and manipulating light at the nanoscale [1].

1.2.2 Surface plasmon based photonics: nanophotonics

Light plays a very important role in our daily life. It is invaluable for the perception of our surroundings and also very useful for many sensing and imaging applications. Moreover, light can be used to transmit large amounts of information at large speeds with low losses, potentially leading to faster computation and communication applications. Over the centuries humans are trying to develop and miniaturize the optical/photonic components with the aim of generating, detecting, guiding, or switching light at nanometer (deep subwavelength) scales. However using normal optical components, like lenses and microscopes it is impossible to focus the light at nanoscale because of the diffraction limit (Rayleigh criterion). After the discovery of SPs, it is now possible to route and manipulate light at nanometer length using subwavelength metallic structures [3]. SPs form the foundation of a rapidly growing new field of photonic research called, 'Nanophotonics' that have many potential application such as microscopy, computation, data storage, sensors and communications. SPPs (a subset of SPs) can not only propagate on planar surfaces but also along one dimensional (1D) waveguides and hold great promise of becoming the natural link between current nanoelectronics and future integrated nanophotonics, operating at frequencies that are 10^5 times higher than microchip clocks.

1.2.3 Importance of Au NPs

Noble MNPs especially Au NPs have attracted tremendous attention in recent years owing to their unique chemical and physical properties, as well as novel biomedical applications [25]. Compared with other metallic nanostructures, Au NPs have several unique advantages:

1. Au NPs are non-toxic to human cells and biocompatible, which makes them good candidates for modern medicinal applications, especially cancer diagnostics [26, 27], drug delivery [28], and photothermal therapy [26].

2. Au exhibits unmatched chemical stability in the ambient environment, and Au nanostructures preserve their properties for many years. By contrast, silver, which may initially provide better performance, loses its lustre and plasmonic properties within days.

3. Another big advantage of Au is it's use in biosensing as because its chemical interaction with organic compounds is extremely well understood. For instance, so-called 'label-free biosensing techniques', negate the need for dyes or radioactive tracers in biochemical assays. Achieving sensing selectivity requires initial 'functionalization' of a gold surface the attachment of sensed molecules which then modifies the plasmonic resonance, leading to a detectable colour change [29]. The current drive is towards miniaturization. The ability to add precise nanostructures to gold surfaces makes it possible to incorporate this technique in lab-on-a-chip systems.

4. Monodisperse Au NPs of different shape and size can easily synthesized by simple and fast chemical preparation method. Also their surface plasmon resonance (SPR) frequency can be tuned from visible to NIR region by simply changing the size, shape and surrounding environment.

5. In gold, the nonlinear response determined by plasmonic lifetime is less than 10 femtoseconds about five times faster than in silver [30]. The nonlinearity is also stronger than in silver. In fact, gold's high and fast nonlinearities may lead to optical switches that are faster than electronic ones a development that could have enormous consequences as information processing migrates into the optical realm.

1.3 Importance of single particle spectroscopy

This thesis is mainly dedicated to the study of plasmonic property of an isolated individual MNPs dispersed on silicon (Si) substrate. Complementary to the conventional ensemble measurements, single particle spectroscopy always gives rise to some new information. Although single particle experiments are very difficult due to the very small signal-to-noise ratio, they have certain advantages:

1. Often with the best available chemical synthesis approach one does not obtain a monodisperse (uniform shape and size) distribution of the NPs, rather it is mixed up with heterogeneous ensemble of NPs of various shape and size. By measuring the properties of individual particles, one recovers the full distribution of a variable in the heterogeneous ensemble of NPs. This is particularly interesting when several properties can be correlated on the same individual

particle, e.g. LSPR induced optical properties can be correlated with electron microscopy images an aspect we have studied extensively in this thesis.

2. The effects arising due to small perturbations or due to very minute changes in shape, size, composition or local surroundings can be measured with enhanced sensitivity as the inhomogeneous broadening is absent in single particle measurements. For example, LSPR frequency of a NP is easily influenced by the adjacent particles, meaning, the usually adopted optical imaging techniques, such as UV-VIS spectroscopy or dark-field microscopy (DFM) that measure the optical properties of the collection of particles at a time is not expected to reflect the spectral feature of an individual entity. In contrast, single particle measurements can do it easily.

3. Also most of the studies for real-space imaging of plasmonic resonances of MNPs utilizing optical far-field techniques (excitation and detection in the far-field) are diffraction limited and thus a spatial resolution with a length scale below 200 nm is not easily achievable. Consequently, single particle spectroscopy with high spatial resolution imaging facility is an essential tool to understand the plasmonic properties of NPs.

1.3.1 CL spectroscopy and imaging in SEM as a proper tool for probing single particle LSPR

Scanning probe microscope (SPM) based techniques, such as, photon scanning tunneling microscopy [31], scanning near-field optical microscopy (SNOM) [32], and apertureless SNOM [33] are widely used techniques to probe LSPRs at the single NP level.

However, these techniques though achieve a high spatial resolution of better than 50 nm require very delicate probe in the form of a nanoscale sharp tip and may suffer from probe-sample interactions, distorting the signal of interest.

In this context, a focused beam of fast electrons deliverable within a scanning or transmission electron microscope (SEM / TEM) has shown to be an emerging tool for studying plasmonic materials [2, 34]. The main advantage of electron microscopes is that single particle spectroscopy can be performed with truly nanometer spatial resolution because the spot size of focused e-beam can be made only few nanometre in a SEM and sub-nanometre in a TEM. Following the bombardment of a MNP by the energetic electron beam within the electron microscope, the LSP modes are excited on the surface of the nanostructure. The LSP excitations can be probed by detecting the energy loss suffered by the inelastically scattered transmitted electrons (electron energy-loss spectroscopy, EELS in a TEM) [35–43] or by detecting the optical radiation caused by plasmon decay that is subsequently emitted by the material (cathodoluminescence, CL both in SEM and TEM) [44–52]. The resulting CL images provide direct information of the wavelength dependent local density of optical states (LDOS) [2, 53] of the imaged individual plasmonic nanostructures. Mapping the spatial variation of the photon emission is a direct probe of the LSP modes and, consequently, provides a direct way to map the near-field properties. Also unlike SNOM, CL detects the radiative modes without perturbing the local environment, which makes CL-SEM a powerful tool for direct analysis of the LDOS at the single nanoparticle level.

1.4 Importance of studying higher order plasmonic modes

It is well known that for smaller NP size, the single resonance peak observed in scattering/ absorption spectra is nothing but dipolar mode [1, 54]. Also it is familiar that with increasing particle size the dipolar mode is red-shifted and additional multiple peak arises due to retardation effects which is related to the higher order (quadrupolar and beyond) modes. Investigation and identification of higher-order surface plasmon modes are important from fundamental understanding and application point of view [55, 56]. However, identifying the higher order LSPR modes from these anisotropic nanoparticles in spectral and spatial domain are not trivial. Identifying the signature of higher order LSPR modes of these anisotropic NPs has been one of the concerns of the present thesis.

1.5 Effect of substrate on plasmonic response

The LSPR frequency of MNPs can be tuned by varying their size, shape [54, 57, 58], composition [58], and local dielectric environment [13, 54, 59–62]. The local dielectric environment, in particular, the presence of substrate plays an important role in the plasmonic property of MNPs [13, 60, 62]. As for example, when a MNP is immersed in a homogeneous dielectric medium, the local dielectric environment is symmetric, but when the MNP is placed on a substrate, the symmetry is broken, leading to strong modifications of the plasmonic response of the MNP, such as mode splitting. As it has been shown in this thesis that the presence of Si substrate has a big role in the observed plasmonic modes of anisotropic Au nanoparticles (Decahedron, octahedron,

concave nanocube).

1.6 FDTD-based electrodynamic calculations for metal nano plasmonics

The reason behind the spectacular colors shown by the MNPs was first analytically explained by Maxwell-Garnett in two seminal papers in 1904 and 1906 [63, 64]. In 1908, Gustav Mie ultimately gave a quantitative explanation of the size dependent optical properties of metal nano spheres [65]. Mie's theory has provided an enormous amount of insight into the normal modes of oscillation of the EM fields of the spherical NPs and their effect on light absorption and scattering. However, Mie theory can only explain plasmon modes of very simple geometries, like the sphere or the infinite cylinder. With remarkable developments in synthesis techniques, a large variety of anisotropic MNP morphologies have been synthesized in recent years [25, 62, 66]. At the same time, there was a demanding need for the development of new computational tools which can solve Maxwell equations for complex shaped MNPs. Although computational methods was first developed by Purcell and Pennypacker using the discrete dipole approximation (DDA) [67] to simulate more complex geometries, only very recently the methodology became enormously popular in the context of plasmonic calculations [68, 69]. In the last few years, development and commercialization of several new numerical methods which are based on classical electrodynamics, like finite element method (FEM), boundary element method (BEM) and finite difference time domain (FDTD) have led to a very rapid growth of the simulation aspects

of plasmonic structures. Among different numerical techniques, FDTD becomes increasingly popular in recent times due to it's ability to solve diverse problems in electromagnetics and photonics. As FDTD method solves Maxwell equation in time-domain, it can cover a wide frequency range with a single simulation run, and treat nonlinear material properties in a natural way. Thus a full range of useful quantities, such as the complex Poynting vector and the transmission/ reflection of light can be calculated.

1.7 Synthesis of Au NPs

The LSPR frequency of MNPs can be controlled precisely by playing with their shape, size, surroundings and dielectric constant. Hence obtaining different size and shape NPs in a controlled fashion is the key aspect in studying the optical properties of these materials. Anisotropic nanoparticles are particularly interesting since their reduced symmetry allows us to tune their optical property to a huge extent. Among different synthesis procedures, seed mediated growth is an easy and efficient way to synthesize anisotropic Au NPs of several types of morphology. All the different shape and size Au NPs of in this thesis are synthesized via seed mediated growth method. In this method seeds are used as templates for the heterogeneous nucleation of anisotropic NP products.

1.8 Outline of this thesis

This thesis is concerned with synthesis and optical characterization of low dimensional anisotropic metal structures. For synthesizing anisotropic metal nano structures seed

mediated wet chemical synthesis approach have been employed. The LSPR induced optical properties of these nanostructures are characterised by CL technique in a high resolution scanning electron microscope (HRSEM). Experimental studies on the LSP induced photon emission upon excitation with energetic electron beam from anisotropic Au nanostructures has been corroborated with FDTD simulations. The thesis is arranged into the following chapters:

Chapter 2 explores basic theoretical concepts that forms the basis of metal nanoparticle plasmonics and detection of plasmons with truly nanometer scale spatial resolution using CL in a SEM. In the latter part of the chapter, the basic principle of FDTD numerical simulation and its application in CL based MNP plasmonics are also discussed.

Chapter 3 presents the details of the chemical synthesis protocols to synthesize anisotropic metal nanostructures of different size and shape. The details of the CL setup in HRSEM, which is the primary characterization tool throughout this thesis have described. Along with the actual instrumental configurations, basic principles of transmission electron microscopy (TEM), energy dispersive X-ray (EDX) are also briefly discussed.

Chapter 4 describes application of CL spectroscopy and imaging to investigate the plasmonic response of isolated single polyhedral Au NPs of two different geometry namely decahedron and octahedron. FDTD simulations are also performed to understand the modal distribution of different resonant modes and to explore the effect of substrate.

Chapter 5 describes the plasmonic properties of individual Au concave nanocubes

in the size range of 170 nm to 225 nm using CL spectroscopy and imaging technique. Optical and e-beam based FDTD simulations are performed to understand the LSPR response of different resonant modes. With the help of FDTD simulation, the origin of different plasmon modes and the effect of substrate on the plasmonic property of these concave nanocubes has been investigated extensively.

Finally in **Chapter 6**, a chapter wise summary of the thesis along with the scope for future study is outlined.

Chapter 2

Localised surface plasmons, cathodoluminescence and related optical properties: basic concepts and numerical approaches

---

This chapter describes several basic theoretical concepts including the origin of particle plasmons or localized surface plasmons. Furthermore the physics of probing plasmons, with nanometer scale spatial resolution, using CL in a SEM has also been described.

2.1 Introduction

Surface plasmons (SPs) are charge-density fluctuations at the interface between a metal and a dielectric. They are solutions of the Maxwell equations and most generally described as a mixture of photons and electrons. Surface plasmons exist mainly in two forms, as propagating SPs or surface plasmon polaritons (SPPs) and localized surface plasmons (LSPs) or particle plasmons.

SPPs sustained at a flat metal-dielectric interface are propagating electromagnetic surface waves (as shown in Figure 2.1 (a)) associated with a collective oscillation of the free electrons in the metal driven by the external electromagnetic excitation. SPPs are basically bound non-radiative 2D surface modes whose existence is characterized by opposite signs of the real part of the dielectric functions of the materials separating the interfaces. Typical dispersion curve for SPs are shown in Figure 2.1 (c), which clearly indicates a mismatch in momentum between light and SPP for same frequency. Because of the evanescent character (decaying exponentially away from the interface) of SPP, they cannot be directly coupled to propagating light and thus special technique is required to compensate for the momentum mismatch. This is usually done by using a coupling medium (such as a prism or grating) or a topological defect on the surface (such as a sub-wavelength protrusion or hole) [3].

On the other hand LSPs are non-propagating excitations of the conduction electrons of metallic nano-structures coupled to the electromagnetic field. An example of LSPs are those supported by metal nanoparticles, illustrated schematically in Figure 2.1 (b). In this case, an incident electromagnetic field causes the electron cloud in the

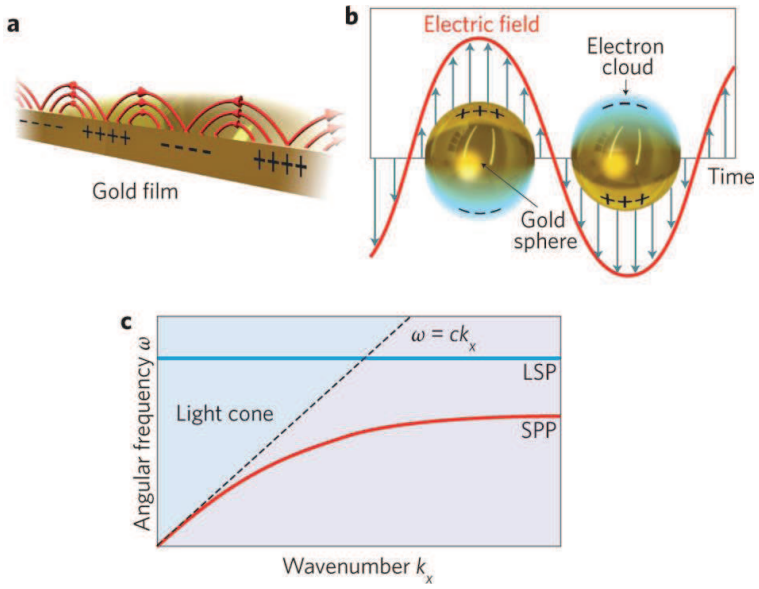

Figure 2.1: *a,b, Collective oscillation of electrons with the incident electromagnetic field at a flat gold-air interface (SPP; a) and in a gold nanoparticle (LSP; b). c, Typical dispersion curves of SPPs (red) and LSPs (blue). Image adapted from Ref. [20]*

MNP to oscillate coherently, resulting in positive and negative charge polarization. A restoring force arises from the Coulomb attraction between the displaced electrons and the positively charged nuclei, and the electron cloud oscillates at the dipolar plasmon resonance frequency. These modes arise naturally from the scattering problem of a small sub-wavelength conductive nanoparticle in an oscillating electromagnetic field. The curved surface of the particle excerts an effective restoring force on driven electrons, so that a resonance can arise, leading to field amplification both inside and in the near field zone outside the particle. This resonance is called the localized surface plasmon resonance (LSPR). In contrast to propagating SPPs, the plasmon resonances of MNP can be excited by direct light illumination where the finite size of

the MNP provides additional momentum to ensure the momentum conservation. As this thesis is mainly concerned with studying particle plasmons or LSPs, I will concentrate more on Physics of LSPRs and the applications of CL to investigate the mechanism of plasmon assisted light emission from Au NPs of different morphology.

2.2 Fundamentals of LSPR

2.2.1 Non-retarted description of spherical particle

The Physics of LSPR can be explored by considering the interaction of MNPs with an EM wave. In the non-retarted approximation, the EM interaction between different parts of the metal is almost instantaneous (i.e., the speed of light can be taken as infinite) and the delay experienced by the EM signal is neglected. Non-retarted or quasi-static (QS) approximation is only valid when the size of the object of interest is much smaller than the typical wavelength of light. In this case, terms connecting electric and magnetic fields disappear from Maxwell's equations, leading to the condition that electric and magnetic fields are longitudinal ($\vec{\nabla} \times \vec{E} = 0$, $\vec{\nabla} \times \vec{H} = 0$).

Let us assume a homogeneous isotropic sphere of radius a ($a << \lambda$) in a static electric field $\vec{E} = E_0 \hat{z}$ as shown in Figure 2.2. The surrounding medium is isotropic and non-absorbing with dielectric constant ϵ_m, and the field lines are parallel to the z-direction at sufficient distance from the sphere. The dielectric response of the sphere is further described by the dielectric function $\epsilon(\omega)$, which is taken for the moment as a complex number ϵ.

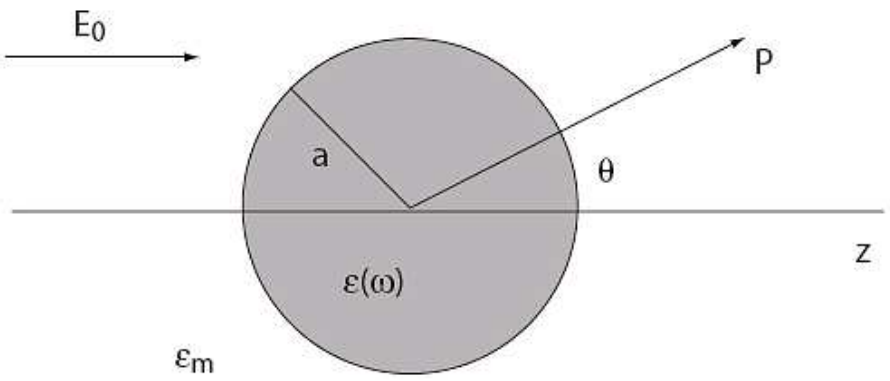

Figure 2.2: *Sketch of a homogeneous sphere placed into an electrostatic field. Image adopted from Ref. [1]*

The electromagnetic solutions to this problem can be found, in the frequency domain, by solving Laplace's equation $\nabla^2\Phi = 0$, from which one can calculate the electric field $\vec{E} = -\vec{\nabla}\Phi$. The potentials satisfying simultaneously Laplace's equation and the proper boundary conditions are

$$\begin{aligned} \Phi_{in} &= -\frac{3\epsilon_m}{\epsilon + 2\epsilon_m} E_0 r cos\theta \\ \Phi_{out} &= -E_0 r cos\theta + \frac{\epsilon - \epsilon_m}{\epsilon + 2\epsilon_m} E_0 a^3 \frac{cos\theta}{r^2}. \end{aligned} \tag{2.1}$$

Physically the Equations 2.1 can be interpreted as follows: Φ_{out} describes the superposition of the externally applied field and the field induced by an elementary electric dipole located at the center of the sphere. Φ_{out} can be rewritten in terms of the dipole moment $\vec{p}$ as:

$$\begin{aligned} \Phi_{out} &= -E_0 r cos\theta + \frac{\vec{p}\cdot\vec{r}}{4\pi\epsilon_0\epsilon_m r^3} \\ \vec{p} &= 4\pi\epsilon_0\epsilon_m a^3 \frac{\epsilon - \epsilon_m}{\epsilon + 2\epsilon_m} \vec{E}_0. \end{aligned} \tag{2.2}$$

So, the applied field induces a dipole moment inside the sphere of magnitude proportional to $|\vec{E}_0|$. If a new parameter, polarizability, α is introduced which is defined as $\vec{p} = \epsilon_0 \epsilon_m \alpha \vec{E}_0$, one gets:

$$\alpha = 4\pi a^3 \frac{\epsilon - \epsilon_m}{\epsilon + 2\epsilon_m}, \tag{2.3}$$

Equation 2.3 is the expression for complex polarizability of a small sphere of sub-wavelength diameter in the electrostatic approximation. It is clear that the polarizability experiences a resonant enhancement under the condition $|\epsilon + 2\epsilon_m|$ is minimum. For small or slowly varying Im[ϵ] the condition of resonance becomes:

$$Re[\epsilon(\omega)] = -2\epsilon_m. \tag{2.4}$$

This relationship is called Fröhlich condition and the mode associated with it is called dipolar LSPR of the MNP. The associated charge distribution is given by an accumulation of positive and negative charges on opposite poles of the sphere, known as dipolar mode. For a sphere consisting of a Drude metal with a dielectric function $\epsilon(\omega) = 1 - \omega_p^2/(\omega^2 + i\gamma\omega)$ located in air, the Fröhlich condition is met at frequency $\omega_0 = \omega_p/\sqrt{3}$, where ω_p $(= \sqrt{\frac{ne^2}{m\epsilon_0}})$ being the plasma frequency of the free electron gas.

2.2.2 Retardation effect

QS limit or non-retarded approximation is a first approximation and for particles of larger dimensions ($a \not\ll \lambda$), QS approximation is not justified due to significant phase-changes of the driving field over the particle volume. Also, due to the finite speed of the light, electromagnetic interaction between different parts of the metal is not instantaneous for larger particles and retardation effects come into play. The most

notable retarded effects are redshifts in the SP energies, coupling of light to modes other than dipolar. Multipolar plasmon modes are appeared due to the retardation effect when NP size increases with respect to the resonant EM wavelength [70], i.e. when the size parameter x is close to 1, where x is defined as : $x = \pi a/\lambda$ [71, 72]. For the case of larger objects other methods are needed such as Mie theory which takes into account retardation effects due to the spatial variation of the electromagnetic field within the object. The a = 0 limit of Mie theory gives the quasi-static limit: $\omega_l = \sqrt{\frac{l}{2l+1}}\omega_p$. However, when the geometry of the object strongly differs from the spherical shape, the use of numerical methods is required to solve this electromagnetic problem.

2.3 Light scattering and absorption by MNPs

When an light wave incident on MNPs, the NP can absorb and/or scatter part of the incoming radiation. This absorption and/or scattering is strongest when frequency (ω) of light wave lies in the vicinity of the particle's surface plasmon frequency. The most striking consequence of LSPs excitation is the strong color that noble metal particles exhibit, which depends on size, shape and environment of the particles. The efficiencies of absorption and scattering are characterized by their wavelength-dependent respective cross-sections, σ_{abs} and σ_{scat}. For a spherical NP of radius a in the QS limit, the cross-sections are given by the expressions [1, 71]:

$$\sigma_{abs}(\omega) = 4\pi k a^3 Im[\frac{\epsilon(\omega) - \epsilon_m}{\epsilon(\omega) + 2\epsilon_m}] \tag{2.5}$$

and

$$\sigma_{scat}(\omega) = \frac{8\pi}{3} k^4 a^6 |\frac{\epsilon(\omega) - \epsilon_m}{\epsilon(\omega) + 2\epsilon_m}|^2. \tag{2.6}$$

Another very important quantity is the so called extinction cross section (σ_{ext}), defined as sum of the former two cross sections (σ_{ext}=σ_{abs}+σ_{scat}) and it can be measured through the decrease of intensity of a light beam along its trajectory through a sample. It is interesting to notice that σ_{scat} scales with a^6/λ^4 whereas σ_{abs} varies with a^3/λ. Consequently, the extinction cross section for large particles is dominated by scattering, whereas for small particles it is dominated by absorption. Moreover, scattering becomes stronger at shorter wavelengths. In the QS approximation, only the dipolar mode is detected, as already discussed. However, when the particle becomes larger and reaches the retarded regime, other multipoles (quadrupole or octapole or higher order) can be excited but with a lower efficiency.

2.4 Influence of dielectric environment on LSPR

Local dielectric environment takes part a very important role in the plasmonic property of MNPs. It is clear from equation 2.4 that a change in dielectric environment (ϵ_m) corresponds to a change in the LSPR frequency on the MNPs. Also it express the resonance frequency red-shifts as ϵ_m increased. As nanoparticles are often produced on surfaces, it is important to understand how their interaction with the substrate influences their plasmon resonance properties. When the MNP is immersed in a homogeneous dielectric medium, the local dielectric environment is symmetric, but when a substrate is present beneath a NP, the local dielectric environment becomes

non uniform around the NP, the homogeneity is destroyed and the symmetry is broken. For example, when a sphere is in air or embedded in a homogeneous medium, it has three degenerate dipolar LSP modes along three directions. Hence in absence of substrate, the dipolar plasmon modes of a sphere are 3-fold degenerate. However, introduction of a dielectric substrate beneath the sphere reduces the symmetry and lifts the degeneracy, giving rise to a splitting of the dipolar LSPR [47, 73]. This interaction can be simply understood using an image charge model [61, 73, 74], where the EM fields induced by a particular multipolar nanoparticle plasmon mode are screened by the induced image charge on the dielectric substrate and acquire different multipolar components in the coordinate system centered on the nanoparticle. The image charge magnitude is reduced by a factor $(\epsilon_s$ -1$)/(\epsilon_s$ +1$)$, where ϵ_s is dielectric permittivity of the substrate. The strength of particle-image interaction is governed by the separation between the nanoparticle and the substrate, the substrate permittivity, and the polarization of the incident radiation [13, 61, 73, 75, 76]. This screening thus mediates an interaction between multipolar plasmons of different order resulting in localized hybridized nanoparticle plasmons.

Recently it has been shown that symmetry breaking in presence of substrate can also lead to the Fano resonances and gives rise to a spectrum characterized by an asymmetric line shape or sometimes a distinct dip structure [13, 60, 77, 78]. Fano resonance arises because of the weak coupling and interference between a broad bright modes and a narrow dark plasmon mode. Bright plasmon modes are those mode which possess finite dipole moments and can therefore be efficiently excited by incident light. Since the bright modes couple to light, they also radiate, and their spectral

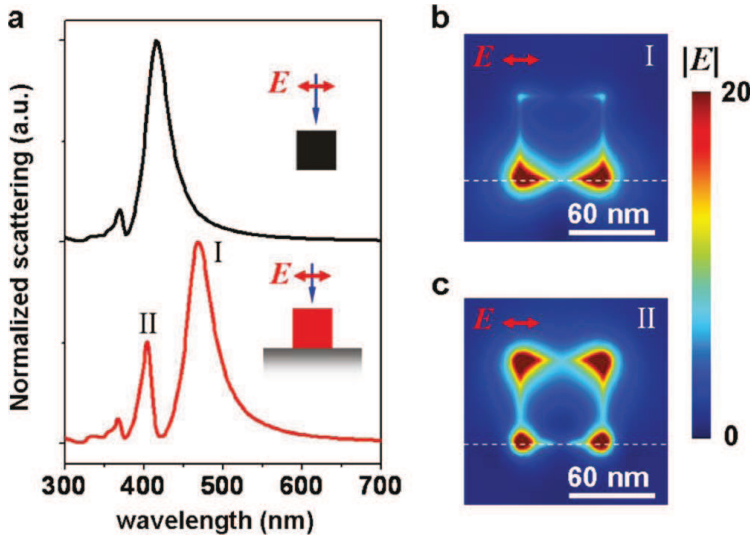

Figure 2.3: *(a) Normalized scattering spectrum of a 60 nm Ag cube in vacuum (black) and on a glass substrate (red), under normal incidence plane wave excitation calculated using FEM and JC. (b, c) Electric field amplitude —E— at peak I (469 nm) and peak II (404 nm) in (a), at a plane 1 nm away from the side surface of the cube. The incident light is polarized parallel to the cube edge. Image adapted from Ref. [13]*

features can be significantly broadened due to radiative damping. In contrast, dark plasmon modes possess zero dipole moments, do not couple efficiently to light, and are therefore not radiatively broadened. Moreover, Fano resonances are more likely to be appeared when the larger NPs are deposited on a high dielectric substrate. When the nanoparticle is large in size, multipolar plasmon modes are excited owing to the retardation effect while substrate with large dielectric constant can induces larger image charges. Both of these are essential for hybridization of different surface plasmon modes and occurrence of Fano resonance [13, 77, 78]. As for example Zhang et al. [13] theoretically demonstrated that in presence of the substrate a Fano resonance can occur in the scattering spectra of the Ag nanocube through the formation

of so called distal and proximal modes [13, 38, 39, 60](Figure 2.3). For the case of Ag nanocube, the proximal LSPR mode (peak I at 469 nm) is the bonding mode between bright dipolar and dark quadrupolar mode, has most of the field intensity towards the substrate (Figure 2.3(b)). Whereas, the distal mode (peak II at 404 nm) originates from the antibonding mode between dipolar and quadrupolar mode, has more field intensity away from the substrate penetrating into the vacuum (Figure 2.3(c)).

2.5 Electron beam excitation and CL

When a beam of energetic fast electrons hits a sample a multitude of processes can occur. Besides the generation of electron signals, a broad spectrum of EM radiation ranging from x-rays to the mid-IR is generated through a variety of incoherent and coherent processes. If the emitted EM radiation lies in the visible/NIR regime of the spectrum region then it is known as cathodoluminescence (CL), a term originating from early cathode ray tube experiments.

Before going to the details origin of CL emission from an MNPs, I will first describe the advantage of electron beam over optical excitation.

2.5.1 Electron beam as a broadband source of light

An electron moving at a constant velocity through space is accompanied by evanescent electromagnetic fields [2] as shown in Figure 2.4. The electromagnetic field that accompanies a point charge moving in vacuum can be written as :

$$E(\vec{r},\omega) = \frac{2e\omega}{v^2\gamma_\epsilon\epsilon} g(\vec{r}) \tag{2.7}$$

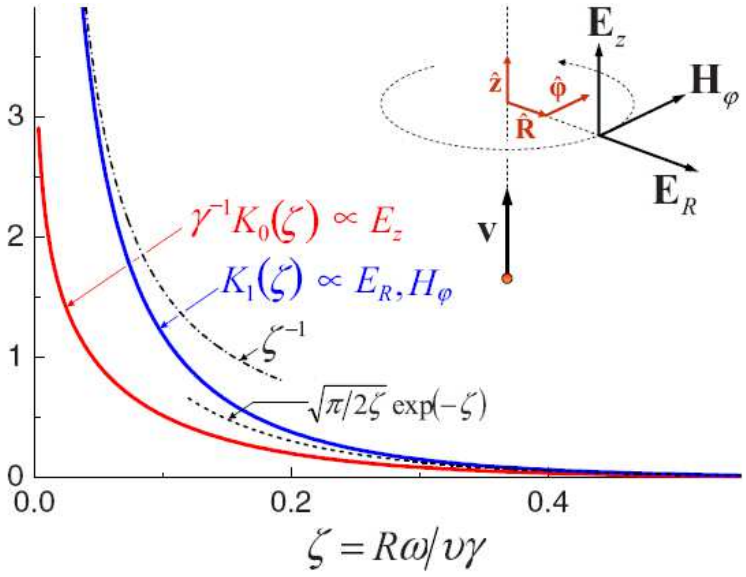

Figure 2.4: *Evanescent character of the electromagnetic field produced by a fast electron. Transverse-spatial direction dependence of the* $\exp(-i\omega t)$ *contribution to the electromagnetic field set up by an electron moving in vacuum with velocity* $v = 0.7c$ *(*$\gamma \approx 1.4$ *and kinetic energy* $\approx$ *200 keV) along the positive* z *axis. The only non-vanishing components* E_R*,* E_z*, and* H_φ *decay exponentially at large distance* R *from the trajectory. The inset shows the orientation of these components relative to the electron velocity vector. The small-*R *limit is dominated by the* $1/R$ *divergence of* E_R *and* H_φ*. Image adapted from Ref. [2]*

where

$$g(\vec{r}) = e^{\frac{i\omega z}{v}}[\frac{i}{\gamma_\epsilon}K_0(\frac{\omega R}{v\gamma_\epsilon})\hat{z} - K_1(\frac{\omega R}{v\gamma_\epsilon})\hat{R}] \tag{2.8}$$

$\gamma_\epsilon = 1/\sqrt{1-\epsilon v^2/c^2}$ is the Lorentz contraction factor and R is the distance from the electron trajectory. Similarly the magnetic field can be written as:

$$H(\vec{r},\omega) = -\frac{2e\omega}{vc\gamma_\epsilon}K_1(\frac{\omega R}{v\gamma_\epsilon})e^{i\omega z/v}\hat{\varphi}, \tag{2.9}$$

where $\hat{\varphi}$ is the azimuthal unit vector. From equations [2.7-2.9], one can see that moving electron acts as a broadband source of evanescent electromagnetic field with the

frequency components of the field moving with velocity v along the electron trajectory. This is advantageous in investigating localized excitations (such as plasmons), involving wave-vector components of the electromagnetic field that lie outside the light cone. Another interesting consequences of fast electrons is that they can not only generate SPPs when passing near a metal surface but also can excite non-dipolar modes in small particles [79], which would be difficult to resolve using external light instead.

2.5.2 A theoretical description of CL for plasmon measurement

The mechanism of CL emission can be broadly classified into two categories (coherent and incoherent CL) according to their degree of coherence with respect to their field of impinging electrons. Both coherent and incoherent processes give rise to CL emission. Incoherent emission is commonly related with creation of electron-hole pairs or other electrical excitations which subsequently recombine and emit radiation. This incoherent CL is very much dependent on material and widely used in semiconductor technology and mineralogy for the characterization of materials. In metals electronic relaxation channels are much faster than radiative recombination, so that incoherent radiation is only a minor contribution to CL.

Coherent CL radiation includes Cherenkov radiation, transition radiation and diffraction radiation. The generation of SPs can be considered as an indirect emission process, but also falls into the group of coherent emission.

The CL emission comes from the skin depth under the sub-surface of metals ($\sim$ 20 nm in the visible and NIR for noble metals) which drastically erases any effects arising

from the electron solid collision cascade produced by the impinging electron probe in deeper region. Moreover radiative inelastic decay has insignificant contribution to CL in metals because electronic relaxation channels are faster by several orders of magnitude. Therefore, the CL signal arising from metallic nanostructures, is dominated by exciting plasmon modes. Quite different from SPPs, localized plasmons can decay radiatively, thus contributing to CL. Thus the CL signal resulting from plasmon decay offers an opportunity to perform plasmon spectroscopy with truly nanometer spatial resolution.

When a first moving electron beam is focused onto or close to the nanostructure of interest, it will transfer some part of it's energy to the nanostructure via electromagnetic interaction [2]. During this interaction the electron beam loose some energy while the NP gain same amount of energy that electron is lost. The amount of energy that is lost by the electron during electron-sample interaction is measured by EELS. However the sample re-emits a part of the absorbed energy in the form of photon to return to equilibrium via a radiative decay channel, gives rise to the CL signal. Accessing the energy of the emitted photons, as is done in CL, thus allows recovering the energy characteristics of the radiative decay channel, which can be different from the energy of the excitation if fast non-radiative decay channels are available. In particular, CL probes the scattering physics, while EELS probes the extinction one [80]. For the case of MNPs, CL is generally computed by estimating the energy carried by the induced field and propagating to the far-field. The probability of CL emission can be calculated by integrating the Poynting vector over the emission directions. The

emitted energy per incoming electron is given by [2]:

$$\Delta E = \frac{c}{4\pi} \int dt r^2 \int d\Omega \hat{r} \cdot [\vec{E}^{ind}(\vec{r},t) \times \vec{H}^{ind}(\vec{r},t)] \tag{2.10}$$

where $\hat{r}$ is the unit vector along the radial direction, and $\vec{E}^{ind}$ and $\vec{H}^{ind}$ the induced electric and magnetic fields on the specimen, respectively. Finally one can decompose ΔE into photon energy components $\hbar\omega$ as:

$$\Delta E = \int_0^\infty \hbar\omega d\omega \int d\Omega \Gamma_{CL}(\Omega,\omega), \tag{2.11}$$

where

$$\Gamma_{CL}(\Omega,\omega) = \frac{1}{4\pi^2\hbar k}|f(\Omega)|^2 \tag{2.12}$$

is the number of photons emitted per incoming electron, per unit solid angle of emission Ω, and per unit of photon frequency range ω.

2.5.3 Plasmon mapping using CL

The rebirth of plasmonics was partially triggered by our ability to visualize surface plasmons through imaging with nm scale spatial resolution. The significance of imaging plasmons lies on the control over the propagation and control over the localization. And in this context, the electron microscopy techniques like EELS and CL are at the forefront. In 2001 Yamamoto [81] et al. showed for the first time that CL can be used to image plasmon excitations. Although the CL signal is much week compared to EELS, CL is advantageous since it can be performed in SEMs, which are more widely available than TEMs, and it works for thick samples since there is no need to collect transmitted electrons.

In CL imaging, one basically map the wavelength dependent radiative electromagnetic local density of optical states (EMLDOS), projected along the electron beam path direction of an individual plasmonic nanostructures [44, 53, 82, 83]. This EMLDOS is a direct probe of resonant modes of the nanostructures and, consequently, provides a direct way to map the local electric fields experimentally. The ability to experimentally visualize the EMLDOS at the single NP level makes CL-SEM a powerful tool in the field of plasmonics. An important point to emphasize here is that CL mapping for metallic nanostructures reveals the efficiency with which electron energy is coupled to the far-field radiation as a function of electron injection position and not the distribution of light emission. The resolution of the technique is slightly larger than the beam spot size with an upper limit dictated by the extension of the evanescent electric field of the electron ($\sim v/2\omega$), where v is the electron velocity and ω is the light frequency (e.g., $v/2\omega = 16$ nm for 30 keV electrons at a wavelength of 600 nm) [82]. This means that plasmon related emission can occur even though the beam does not touch the structure physically.

2.6 Numerical approaches

Although Maxwell's equations provide an accurate description of complete understanding of the fascinating optical properties of metal nanostructures, it is very much difficult to obtain exact analytical solutions for particles of geometries other than spheres, ellipsoids or infinite right cylinders. Alternatively, there are many numerical methods (such as discrete dipole approximation (DDA), boundary element method (BEM), finite element method (FEM) and finite-difference time-domain (FDTD)

method) that can be used to solve the Maxwell's equations for arbitrarily-shaped nanoparticles. The Finite-difference time-domain (FDTD) Method was used to obtain the numerical results presented in this thesis. I briefly introduced here the FDTD method and its application in CL based MNP plasmonics.

2.6.1 Finite-difference time-domain (FDTD)

The FDTD method was first introduced by Yee [84], is an effective computational tool for finding numerical solutions of Maxwell's equations for complex and arbitrary shaped geometries [85]. FDTD solves Maxwell's equations in discretized space and discretized time. This method is based on the approximation of the derivatives by central differences (leapfrog integration algorithm) and to follow the response of a material to any applied EM field. Yee's algorithm centers the E- and H-components in a three-dimensional space grid as shown in Figure 2.5. According to Yee scheme, Cartesian volume element of sides Δx, Δy, Δz and total volume Δ, is used for the space discretization. In this cubic volume element, E and H components are staggered at half increments in space and time (where Δt is the step size for time discretization).

According to Maxwell's equation:

$$\frac{\partial \vec{E}}{\partial t} = \frac{1}{\epsilon}[\vec{\nabla} \times \vec{H} - \vec{J}] \tag{2.13}$$

$$\frac{\partial \vec{H}}{\partial t} = -\frac{1}{\mu}[\vec{\nabla} \times \vec{E} - \vec{M}], \tag{2.14}$$

where ϵ is the permittivity and μ the permeability of the medium. The electric and magnetic current density, $\vec{J}$ and $\vec{M}$ respectively, are given by:

$$\vec{J} = \vec{J}_{Source} + \sigma \vec{E} \tag{2.15}$$

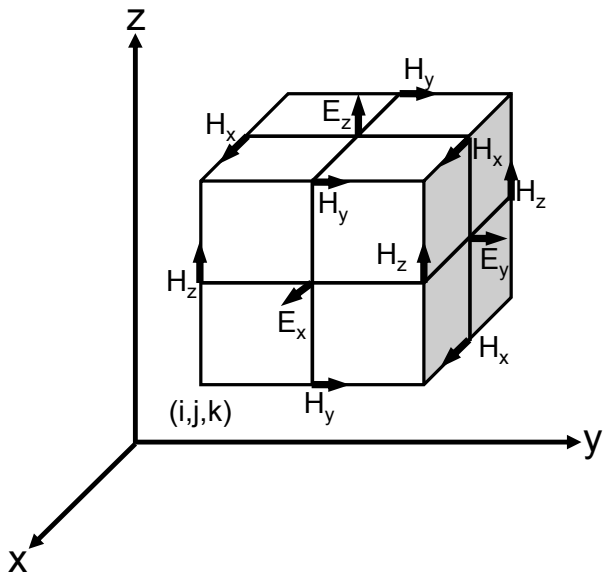

Figure 2.5: *Position of the various field (electric and magnetic) components within the Yee grid. Image adapted from Ref. [84]*

$$\vec{M} = \vec{M}_{Source} + \sigma^* \vec{H}, \tag{2.16}$$

where, σ is the electric conductivity of the medium and σ^* is the equivalent magnetic loss.

If Equations 2.15 and 2.16 are put in Equations 2.13 and 2.14 and the vector components are evaluated, one gets a system of coupled equations which is the heart of FDTD algorithm. As for example, the E_x component is defined as:

$$\frac{\partial E_x}{\partial t} = \frac{1}{\epsilon}[\frac{\partial H_x}{\partial y} - \frac{\partial H_y}{\partial z} - J_{source_x} + \sigma E_x]. \tag{2.17}$$

Utilizing Yee's definition of rectangular coordinate system, one can formulate a finite difference equation from Maxwell's equation in discrete form. According to this, the E_x component at the time step $(n + 1/2)$ at one space point of the lattice $(i, j +$

$1/2, k+1/2)$ that stands for the spatial location $(i\Delta x, j\Delta y, k\Delta z)$ is given by:

$$\frac{E_x|^{n+1/2}_{i,j+1/2,k+1/2} - E_x|^{n-1/2}_{i,j+1/2,k+1/2}}{\Delta t} = \frac{1}{\epsilon_{i,j+1/2,k+1/2}} \cdot \left[\frac{H_z|^n_{i,j+1,k+1/2} - H_z|^n_{i,j,k+1/2}}{\Delta y} - \frac{H_y|^n_{i,j+1/2,k+1} - H_y|^n_{i,j+1/2,k}}{\Delta z} - J_{Source_x}|^n_{i,j+1/2,k+1/2} - \sigma|_{i,j+1/2,k+1/2} E_x|^n_{i,j+1/2,k+1/2}\right] \quad (2.18)$$

As the coefficients are fixed throughout the simulation, so they can be pre-calculated:

$$E_x|^{n+1/2}_{i,j+1/2,k+1/2} = C_a(m) E_x|^{n-1/2}_{i,j+1/2,k+1/2} + C_b(m)(H_z|^n_{i,j+1,k+1/2} - H_z|^n_{i,j,k+1/2} + H_y|^n_{i,j+1/2,k} - H_y|^n_{i,j+1/2,k+1} - J_{Source_x}|^n_{i,j+1/2,k+1/2}\Delta), \quad (2.19)$$

where $C_a(m)$ and $C_b(m)$ are constants associated with the medium [84]. A more detailed and rigorous derivation can be found in Ref. [85]. It is evident from Equation 2.19 that the electric field components at each point in space and in time can be calculated from the previous time step's electric component, the neighbouring magnetic field components of the space lattice and the material properties. The equations are implemented in a leapfrog manner. The software calculates the field components at each space point, for a specified time from the data stored and calculated previously. Then the software increases the time step and repeats the process. In the same way, similar equations can also be derived for the H field. By placing a simulation 'monitor' at a certain location in the simulation mesh, the software records the field components and power at each time step and outputs them for analysis at the end of the simulation. By taking the discrete Fourier transform of the stored time data at the end of simulation the E and H field behavior at each frequency, for a cell, can be

calculated.

For numerical stability there is some restriction on Δt and the cell size. The fields (electric and magnetic) must not change significantly between the cells and hence the cell dimensions must be significantly less than the illumination wavelength. The minimum time step and/or cell size is determined by the Courant condition:

$$S = \frac{c\Delta t}{\Delta}, \tag{2.20}$$

where, S is the Courant number and it should be $\leq \frac{1}{\sqrt{no.of dimension}}$ for numerical stability. Hence for 3D simulation it should be $\leq 1/\sqrt{3}$ [85]. Usually in practical FDTD simulations, the cell size Δ is defined first to ensure sufficient resolution to define the structure geometry. The cell size is typically given by:

$$\Delta \leq \frac{\lambda_{min}}{10 n_{max}}, \tag{2.21}$$

where, λ_{min} is the shortest wavelength present and n_{max} is the highest refractive index present in the simulation region. So, after defining the cell size the minimum Δt can be calculated using Equation 2.20.

In order to understand plasmon assisted photon emission from MNPs, a commercially available FDTD package (from Lumerical FDTD solutions, Canada) is used in the present thesis. In this section, I will describe some salient features of this software package.

2.6.1.1 CAD layout editor

At the user end of the graphic interface of the Lumerical FDTD solutions, there is a CAD layout editor which has two modes of operation: 'layout mode' and 'analysis

mode'. 'Layout mode' is used for setting up the simulation. In this mode simulation objects can be added, modified and deleted. The layout editor automatically switches to 'analysis mode' just after a simulation is complete. In 'analysis mode', it is not possible to edit the simulation objects. The layout editor also shows graphical representation of the simulation from an XY, XZ, YZ and 3D perspective view. There is an in-built object library that includes a wide range of basic and complex objects with a documented script that can be modified to change the shape and size. More complex structures can be generated using combinations of basic structures.

2.6.1.2 Sources

Sources are another important component of a simulation. FDTD Solutions supports a number of different types of sources such as point dipoles, beams, plane waves, a total field scattered-field (TFSF) source, a guided-mode source for integrated optical components, and an imported source to interface with external photonic design softwares.

2.6.1.3 Meshing

When many FDTD cells are combined together to form a three-dimensional volume, the result is an FDTD grid or mesh. The FDTD algorithm also supports a graded mesh of Cartesian (rectangular) cells. This means that the size of the mesh cells can vary as a function of position throughout the simulation region. Such a non-uniform mesh can make FDTD calculations more accurate, while requiring less memory and less computation time than a comparable uniform mesh. Fundamental simulation quantities (material properties and geometrical information, electric and magnetic

fields) are calculated at each mesh point. Lumerical FDTD Solutions provides a number of features, including the conformal mesh algorithm, that allow one to obtain accurate results, even when using a relatively coarse mesh. By default, the simulation mesh is automatically generated. To maintain accuracy, the meshing algorithm creates a smaller mesh in high index (to maintain a constant number of mesh points per wavelength) and highly absorbing (resolve penetration depths) materials. In some cases, it is also necessary to manually add additional meshing constraints. Usually, this involves forcing the mesh to be smaller near complex structures (often metal) where the fields are changing very rapidly.

2.6.1.4 Material database

The materials database allows one to manage (create, modify, delete) the materials that are available for use in simulations. The material database stores the material data to be used in the simulation. Experimental data can also be loaded into the database. A number of materials database are provided with the product installation. As a time domain technique, a single simulation can be used to provide simulation results at many frequency points. This provides the ability to analyze and optimize the design across a wide wavelength range but this is only true to the extent that the models used to describe the dispersive nature of the constituent materials are themselves accurate over the wavelength range of interest. To overcome the multi-wavelength challenge, Lumerical's multi-coefficient materials (MCMs) have been used. MCMs rely on a more extensive set of basis functions to better fit dispersion profiles that are not easily described by Drude, Debye, and Lorentz materials.

With a comparable cost in model complexity and computation speed, the resulting MCM model is superior to the Lorentz-Drude model. The dielectric constant / refractive index used in the calculations are obtained from generalized MCM that fits the experimental dispersion data obtained from different tabulated databases [86–88] that fits better. In Figure 2.6 the fitted plot of the real and imaginary part of the refractive index of gold has been shown where the material data has been obtained from the tabulated values in CRC handbook [88].

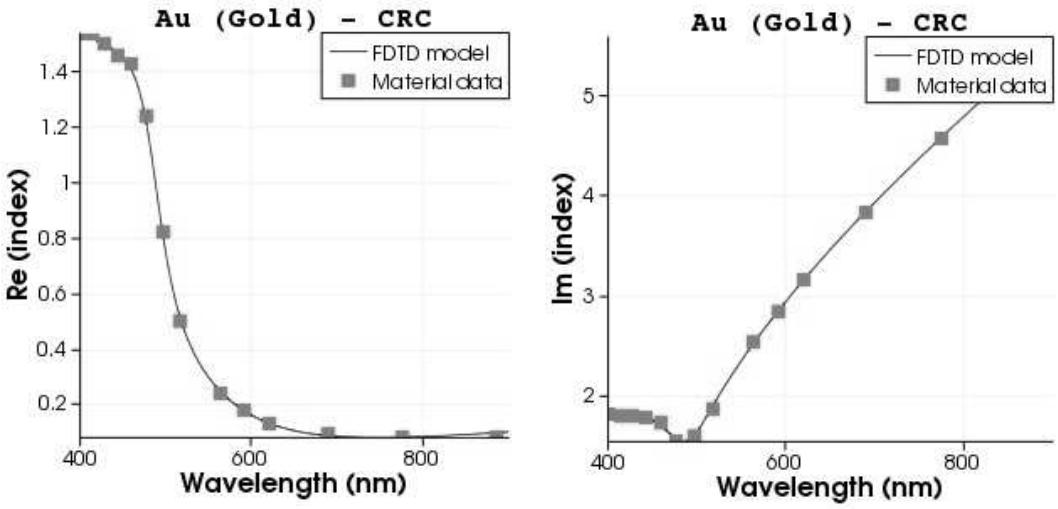

Figure 2.6: *Real and imaginary part of refractive index plotted according to MCM model for gold in the wavelength range 400– 900 nm.*

2.6.1.5 Boundary conditions

Boundary conditions (BCs) are very crucial in electromagnetics and simulation techniques. FDTD Solutions/propagator supports a range of boundary conditions, such

as perfectly matched layer (PML), metallic,periodic, Bloch, symmetric and anti-symmetric.

Perfectly matched layer (PML) boundaries absorb the electromagnetic energy that is incident upon them. Plasmonic simulations very often employ absorbing BCs that allows the radiation to propagate out of the computational area without interfering with the field inside. PML is particularly useful when absorbing radiation in normal incidence. The number of layers depends on the mesh size. More layers causes the simulation to consume more memory. In all simulations presented in this thesis PML BCs have been used.

Other BCs like metal BCs are used to specify perfectly reflecting boundaries allowing no energy to escape along the boundary from the simulation volume. Periodic BCs can be applied when both the structures and the electromagnetic fields are periodic. Bloch BCs can be used where the structures and the electromagnetic fields are periodic but a phase shift exist between each period. Symmetric BCs can be used when the structure has one or more planes of symmetry. Both the structure and the source must be symmetric. Anti-symmetric BCs can be used when the problem exhibits one or more planes of symmetry. Anti-symmetric boundaries are anti-mirrors for electric fields and mirrors for magnetic fields.

2.6.1.6 Monitors

A number of monitors options are available in FDTD Solutions, which are mentioned below:

- **Index monitors:** Index monitors records the n and k value as a function of frequency/wavelength in a simulation.

- **Time-domain monitors:** These monitors provide time-domain information for field components over the course of the simulation. Time-domain monitors can consist of point, line, or area monitors to capture this information over different spatial extents within the FDTD simulation region.

- **Movie monitors:** Movie monitors capture a desired field component over the region spanned by the monitor for the duration of the simulation.

- **Frequency-domain field monitors:** In the FDTD Solutions Frequency-domain field monitors are used to collect the field profile in the frequency domain from simulation results across some spatial region within the simulation. These monitors are commonly used to collect Poynting vector, individual field components, and power flow as a function of frequency and position. These monitors record the field profile where they are exactly placed.

2.6.2 FDTD simulation with electron beam as excitation source

In the subsequent chapters of this thesis, the application of CL to probe plasmon modes over a single metal nanoparticle of different shape and size has been demonstrated. For detailed understanding of the plasmon assisted photon emission and the corresponding features, such as charge distribution, near field intensity maps, and effect of substrate on the different shape and size Au NPs, we have performed 3D-FDTD numerical simulation (from Lumerical solutions, Canada). In our CL experiments,

we have used electron beam energy of 30 keV and beam current of 12 nA. This means the electron impact to the sample on an average in every 11 ps, which is $\sim$ 5000 times longer than one typical optical cycle in the visible spectral range and $\sim$ 200 times longer than the typical electron relaxation time in gold. So, we can neglect the electron-electron interaction and simulate the photon emission for one single electron impact. To numerically investigate the electron beam induced photon emission in a CL set up, we have modelled electron beam as a line current density source. The current density due to moving electron can be represented as follows

$$J(t, \vec{r}) = -ev\hat{u_z}\delta(z - vt)\delta(x - x_0)\delta(y - y_0) \tag{2.22}$$

where e is the electronic charge, and v is the velocity of electron, (x_0, y_0) represents the position of the electron beam, z is the direction of electron velocity, and $\hat{u_z}$ is the unit vector along the z direction. Here current density due to a moving charge is modelled as a series of dipoles with temporal phase delay (z/v), that is related to the electron velocity v (here $v = 0.32c$ corresponding to the 30 keV electron energy used in the present experiment with c being the velocity of light in free space). In the absence of any structure, the electron beam will not generate any radiation because it is moving at a constant velocity. But in FDTD, one is obliged to simulate only a finite portion of the electron path and the sudden appearance and disappearance of the electron will generate radiation. To solve this problem, a second, reference simulation has also been run where all the structures have been removed, and one can calculate the electromagnetic fields at angular frequency ω by taking the difference in fields between the simulations. This makes the analysis slightly more complex because the difference must be taken before calculating quantities like the Poynting

vector or electric field intensity $|E|^2$. To get an accurate difference, the simulation mesh has been forced to be exactly the same with and without the structure. For this reason, Lumerical's mesh override regions has been used over all the structures. To simulate the emission spectra, the radiative energy component of the induced EM field is calculated by integrating the Poynting vector normal (P_z) to an arbitrary large surface in the upper z half-plane for wavelength range as necessary.

To describe the wavelength dependent dielectric constant of gold metal we use experimentally measured gold permittivity data from CRC Handbook of chemistry and physics [88]. We have used Si substrate as a non-dispersive material with fixed refractive index 4 [46, 48] and having a dimension of 5 μm $\times$ 5 μm $\times$ 2 μm throughout our numerical simulation.

2.6.3 FDTD simulation with light beam as excitation source

Optical FDTD simulations in three dimensions is also performed for understanding of the plasmonic properties of MNPs. During optical excitation, we use a total-field scattered-field (TFSF) source to calculate the absorption (σ_{abs}) and scattering (σ_{scat})cross-sections. The TFSF source separate the computation region into two distinct regions: one contains the total field (i.e. the sum of the incident field and the scattered field), while the second region contains only the scattered field. The incident field is a plane wave with a wave-vector normal to injection surface. σ_{abs} (the rate at which energy is removed from the incident plane wave by absorption) is calculated by an analysis group located inside the TFSF source. The analysis group calculates the net power flow into the particle and hence the σ_{abs} using the

optical theorem. Similarly, σ_{scat} is calculated by an analysis group located outside the TFSF source. This group measures the net power scattered from the particle. The extinction cross-section is the sum of the absorption and scattering cross-sections $\sigma_{ext}(\omega)=\sigma_{abs}(\omega)+\sigma_{scat}(\omega)$.

Chapter 3

Experimental methods: synthesis of nanoparticles and characterization techniques

---

This chapter describes chemical routes to synthesize anisotopic Au nanostructures and also describes the CL-SEM instrument that is used as a main optical characterization tool throughout the thesis. Apart from this basic operational principle of TEM is also discussed.

3.1 Introduction

The experimental studies presented in this thesis include chemical synthesis of gold nanoparticles of different shape and size while characterization of plasmonic property of such individual nanoparticle was extensively done by CL-SEM. TEM is also used as an additional characterisation tool for obtaining the morphological, crystallographic and compositional information of as-synthesized nanostructures.

In this chapter, we will first discuss about seed mediated chemical synthesis approach for synthesizing various anisotropic NPs. Next, we will describe about detail operational principle of the CL-SEM system which is used to demonstrate the SP induced optical properties of individual Au NPs. We will also present a brief operational principle of TEM.

3.2 Material synthesis

3.2.1 Cleaning

Cleaning is always a very important issue for getting desired shaped nanoparticles. First of all, the beakers and test tubes were cleaned by using aquarigia because this help to remove metallic impurity. Then deionized (DI) water (Milipore, resistivity 18.5 MΩcm) was used for cleaning and after that all the beakers and measuring cylinders were washed with ethanol. All the Au NPs (CNC, decahedron and octahedron) discussed in the present thesis are synthesized via room temperature seed-mediated wet chemical growth approach. Decahedrons were synthesized following the protocol used by Wu et al. [89, 90]. Whereas, Au CNCs and octahedrons were synthesized following the protocol used by Mirkin et al. [91] with minor modification.

3.2.2 Synthesis of Au decahedron

3.2.2.1 Preparation of Au nanoparticle seed

First of all a volume of 0.2 ml of .025 M sodium citrate (Sigma-Aldrich, $\geq$ 99.9%) solution was added to 19.8 ml of aqueous solution containing 2.5$\times$ 10^{-4} M $HAuCl_4$, $3H_2O$ (Sigma-Aldrich, $\geq$ 99.9%) and stirred for 3 minute. Immediately, 10 ml of 0.01 M $NaBH_4$ (Sigma-Aldrich, 98%) solution was prepared by adding $NaBH_4$ to 10 ml of ice cold 0.025 M sodium citrate solution. Next, 0.6 ml of the freshly prepared $NaBH_4$ solution was taken in a micropipette and added it to the $HAuCl_4$ solution at a time. Immediately the resulting solution becomes orange red, indicating the formation of gold nanoparticles of size approximately 2.5 nm. Particles in this solution were used as seeds within 2-5 h after preparation.

3.2.2.2 Preparation of growth solution

Aqueous solution of of 100 mL of 2.5 $\times$ 10^{-4} M $HAuCl_4$ aqueous solution was prepared in a 250 mL flask. Then 3.645g of cetyltrimethylammonium bromide (CTAB) was added to the solution with continuous stirring until the CTAB powder was completely dissolved. This solution was used as the growth solution.

3.2.2.3 Preparation of Au nanoparticles

Figure 3.1 shows schematic diagram of three step preparation of Au NPs. Two flasks A and B each of 25 mL and another flask C of 100 mL is taken. In flasks A and B, 25 μL of 0.1 M ascorbic acid was added to 4.5 mL of growth solution with stirring until the solution becomes colourless. In flask C 45 mL of growth solution was taken and mixed with 250 μL of ascorbic acid (0.1 M) and 400 μL of nitric acid (0.1 M).

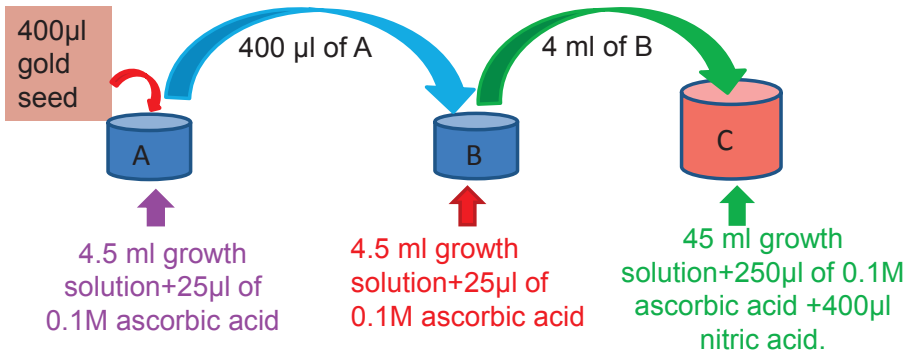

Figure 3.1: *Schematic of three step preparation of Au nanoparticles.*

Next, 400 μL of the Au seed solution was added to the solution in flask A and stirred slightly for few second. Then, 400 μL of the solution in flask A was immediately added to the solution in flask B and stirred for 5 s. Finally, 4 mL of the solution in flask B was transferred to flask C and stirred for 5 s. The solution of flask C was left undisturbed at room temperature for 12 h. Next, the supernatant was discarded and the precipitate was dispersed in 10 mL fresh DI water. The dispersed solution was centrifuged twice with 5000 rpm for 20 minutes each. Each time supernatant was removed and the precipitate was dispersed with fresh DI water. Since our aim was to perform single particle spectroscopy the final solution used was much diluted. The diluted Au solution was dropcoated on a cleaned Si (100) substrate and then loaded into the SEM chamber after sufficient drying in ambient condition. This synthetic approach produces a mixture of nanodecahedrons, triangular prisms, nanorods of different sizes scattered throughout the whole dropcasted region. Among the randomly distributed nanoparticles, isolated single decahedron was identified in SEM for CL measurements.

3.2.3 Synthesis of Au concave nanocube and octahedron

3.2.3.1 Preparation of Au Seeds

Briefly, Au nanoparticle seed were prepared by quickly injecting 0.30 mL (10 mM) ice cold $NaBH_4$ into rapidly stirring aqueous solution containing 10 mL cetyltrimethylammonium chloride (CTAC) (100 mM) and 0.25 mL (10 mM) $HAucl_4$. This seed solution was left undisturbed for two hours to decompose excess borohydride before use.

3.2.3.2 Preparation of growth solution

The growth solution was prepared by successively adding 0.50 mL of $HAucl_4$ (10 mM), 100 μL of AgNO3 (10 mM), 200 μL of HCl (1.0 M), then 100 μL of ascorbic acid (100 mM) into 10.0 mL of 0.1 M CTAC.

3.2.3.3 Preparation of Au nanoparticles

Next, the seed solution was diluted 1000 fold using 100 mM CTAC solution. Finally, desired amount (2-10 μL) of diluted seed solution was added to the growth solution for formation of CNCs. The resultant solution was left undisturbed overnight at room temperature. The colloidal Au solution was centrifuged at 6000 rpm for 15 min, twice, and redispersed in a suitable amount of water. Finally, a few microliters of the diluted solution were drop coated on a cleaned Si (100) substrate and carbon-coated copper grid for SEM and TEM measurement respectively. This synthetic approach produces a mixture of nanostars, CNCs and octahedrons of different sizes scattered throughout the whole dropcasted region. Among the randomly distributed nanoparticles, isolated single CNCs and octahedron were identified in SEM for CL measurements.

3.3 Characterization tools

3.3.1 Scanning electron microscope (SEM)

3.3.1.1 Basics

A SEM is a type of electron microscope which is used to examine surface features of very small object size with length scale down to nanometer. The gradually increasing popularity of the SEM stems from its capability of producing 10–1000000 times magnified, three dimensional-like image of surface features of length scale varying from micrometer to nanometer regime.

When an energetic beam of electrons interact with a sample surface variety of signals are produced (shown in Figure 3.2) due to electron-sample interactions. Depending on the detection of different kind of emitted signals, different aspects of electron-solid interaction based characterization of materials are possible, which is an unique feature of SEM. Emission of electrons or radiation due to electron-target atom interaction comes from a three dimensional region designated as 'interaction volume', which is generated in the sample by the incident energetic electron, as shown in Figure 3.2 (a). The dimension of the interaction volume depends upon the parameters like incident electron energy, atomic mass and density of the target specimen and typically varies from a minimum of around 100 nm at 1 keV electrons to a maximum of around 4 μm at 30 keV electrons. Inside this interaction volume, the incident primary electrons undergo inelastic collisions with the loosely bound outer shell electron of the target atoms and knock them out. These knocked out outer-shell electrons are called secondary electrons (SEs). Maximum energy of SEs can be up to 50 eV. However, 90% of the SEs have energy in the range 0–10 eV. Since the SEs escape with such low energy,

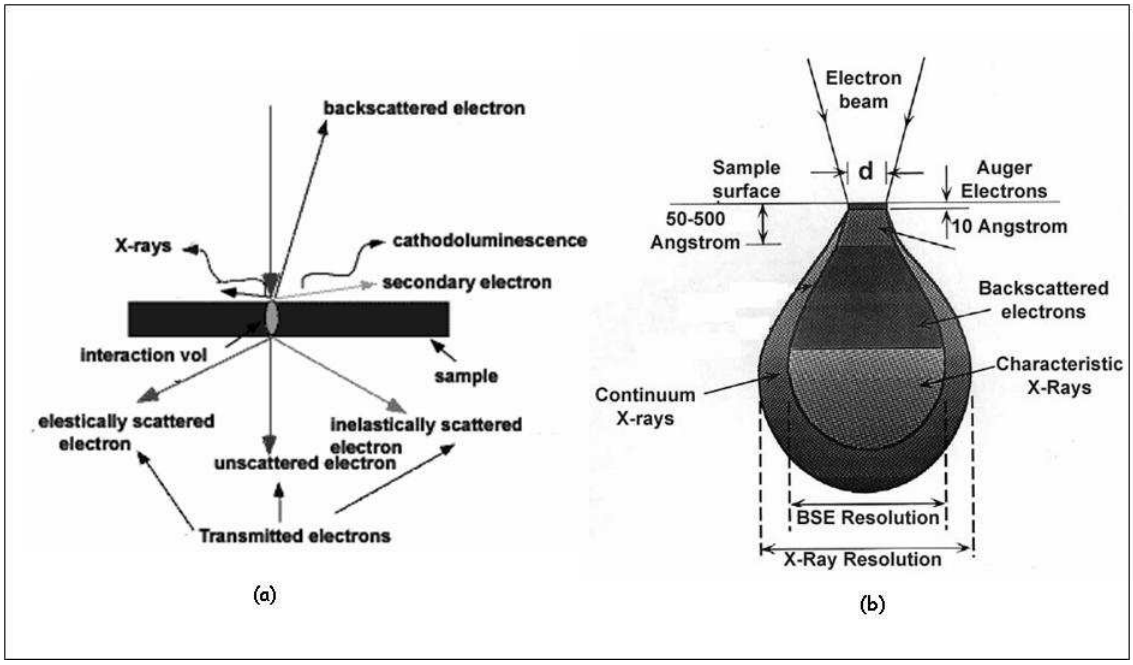

Figure 3.2: *(a) Emissions from an interaction volume due to electron bombardment (b) Enlarged view of the interaction volume. Image courtesy: Internet*

only those generated within a small distance of the surface, typically 50–500 Å, can come out of the surface as shown in Figure 3.2 (b). For this reason, SEs are very sensitive to topography of the surface and are used for imaging the morphology of the samples. On the other hand, electrons of the primary beam can also be scattered in any direction with unchanged energy when the electron undergoes elastic collisions with the nucleus of an atom. Some of the elastically scattered electrons come out of the surface. Energy of these backscattered electrons (BSE) varies from zero to incident electron energy. As these back-scattered electrons are more energetic than the SEs, they can escape from a greater depth of the surface. These backscattered

electrons are used for imaging samples when there is a substantial mass difference between the sample and the substrate that support the sample. During SEM imaging, a finely focused electron beam is made to scan over sample surface in a raster pattern and secondary or backscattered electrons which are generated during interaction of sample with the primary beam, are used to form the SEM images. In SEM, the sample needs to be conducting to prevent charging (accumulation/build up of static electric charges) of the sample surface due to electron emission. To eliminate/reduce this charging in case of non-conducting samples, a very thin gold layer is coated over the sample surface or special beam conditions such as less accelerating voltage or high beam spot size and special detectors are used.

With respect to Figure 3.2 another important technique called energy dispersive X-ray spectroscopy (EDX) has also been established both in SEM and in TEM as an associated analytical tool by using the emitted characteristic x-ray during electron bombardment on sample. Characteristic x-ray is emitted when energetic electron knocks out core level electron of material and electron from higher level comes down to that level. The energy of characteristic x-ray radiation is a characteristic of a particular element from which it comes. During EDX spectroscopy these characteristic X-rays are detected with the help of three components: (1) X-ray detector, (2) processing electronics (3) computer. Here, to detect X-rays Si (Li) detector is commonly used.

3.3.2 CL-SEM facility at SINP

Throughout this thesis, CL in a FESEM has been used extensively as the major characterization tool. The description of each unit with its components will provide a general idea about the system. In this section the working principle and operation of the CL-SEM setup will be discussed.

The CL-SEM system was designed at the Saha Institute of Nuclear Physics (SINP), Kolkata and was custom fabricated by Carl Zeiss, Germany and Gatan, UK, by integrating two main units, namely a field emission gun SEM (SUPRA 40, Zeiss) and a CL system (MonoCL3, Gatan) for light detection. The actual photograph of the CL-SEM set-up and schematic diagram are shown in Figure 3.3 and 3.4 respectively. Zeiss Supra 40 SEM consists of several units such as column chamber, specimen chamber, detectors and vacuum unit. The CL unit consists of a light-collecting paraboloidal mirror, optical monochromator followed by a photon detector and photon-counting electronics. The Gatan MonoCL3 system was controlled by using the Digital Micrograph™ software. Details of the CL-SEM unit has been described elsewhere [92].

3.3.2.1 Configuration of SEM

The Zeiss Supra 40 SEM consists of a high stability Schottky field emission (FE) electron gun system followed by an electron beam column with a single condenser, resulting in a cross free beam path to get good contrast/brightness even at low kilovolt (kV) operation. Inside the system chamber, the specimens are mounted and secured

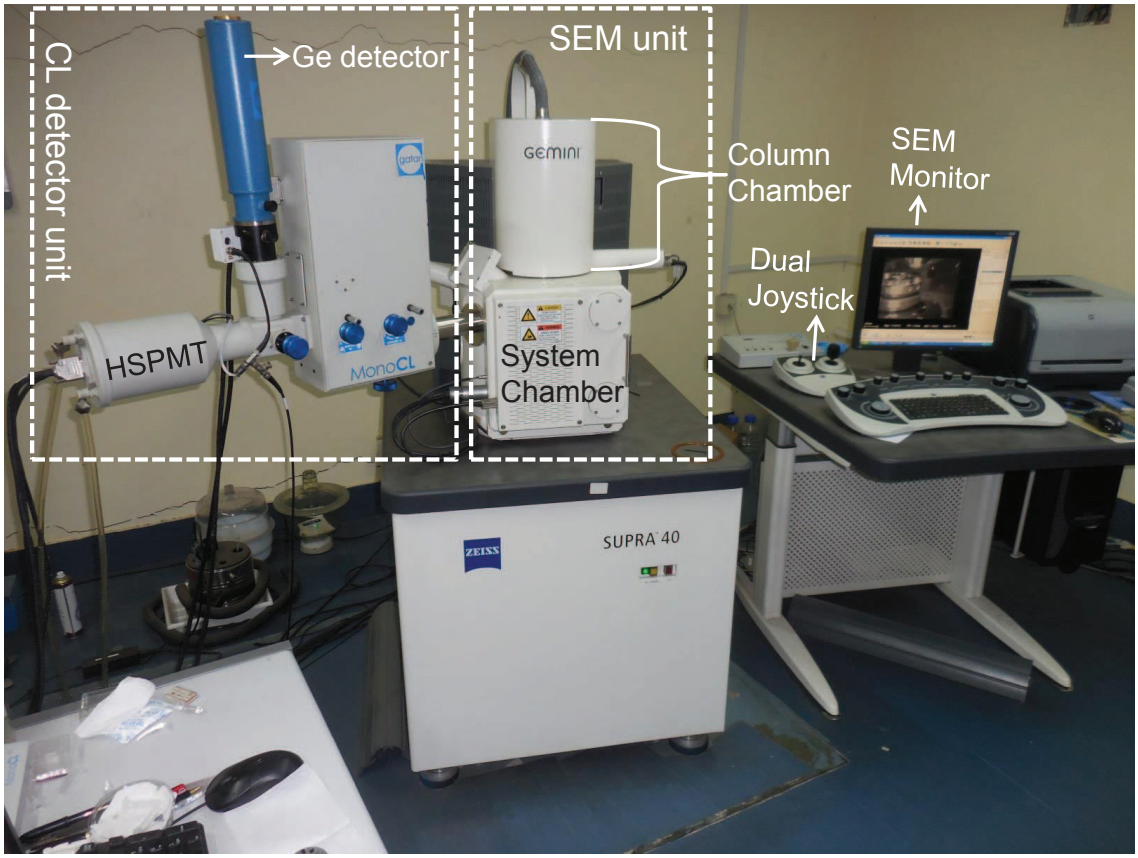

Figure 3.3: *Photograph of the CL-SEM system installed at the Saha Institute of Nuclear Physics, Kolkata.*

onto the sample stage which is a five axes (x, y, z, tilt and rotation) motorized eucentric goniometer stage. The specimen stage can be controlled by the dual joystick controller or by using the soft joystick in the SmartSEM software. The electron accelerating voltage can go from 0.1 to 30 kV, whereas beam current ranges from 0.1 to 40 nA. The vacuum in the specimen chamber is maintained by a a turbo pump backed by a rotary pump having oil trap and oil mist filter that guarantees contamination free vacuum environment. The chamber pressure is always maintained below 1×10^{-5}

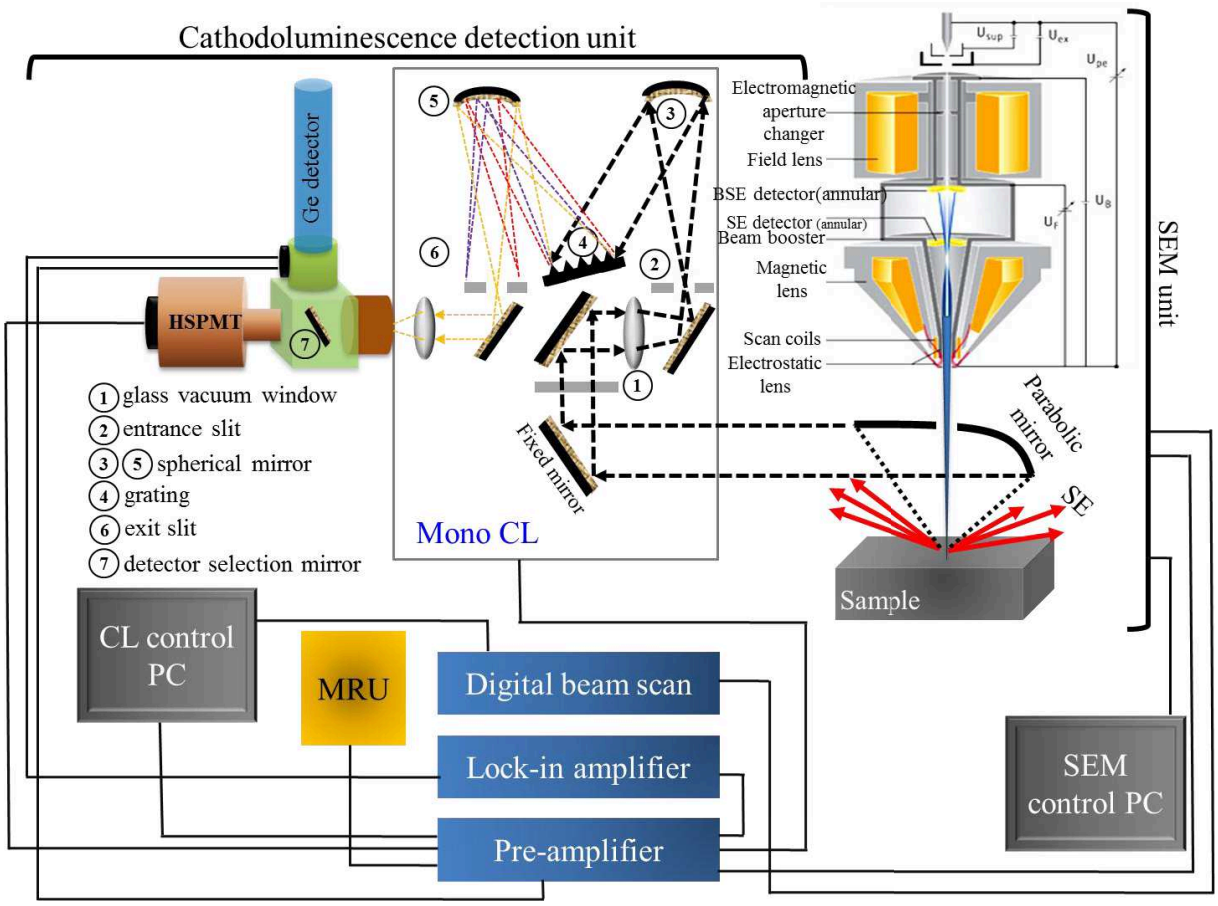

Figure 3.4: *Schematic diagram of the cathodoluminescence in scanning electron microscope (CL-SEM) system.*

mbar and it is measured by a Penning gauge. Whereas an ion getter pump (nominal pumping speed for dry N2 is 53 l/s) is used to maintain the field emission gun (FEG) at ultra-high vacuum (pressure level 10^{-10} mbar) level. The Supra 40 SEM employ an Everhart-Thornly detector (E-T detector) to collect the backscattered and secondary electron. In addition to the SED and BSD detector, the Supra 40 SEM is also equipped with high efficiency annular in-lens SE detector integrated within

the column. As the in-lens detector is located in the beam path, it can map the actual surface of the sample with great accuracy. Commercially purchased carbon film containing gold particles (standard sample used for resolution test) is used for the resolution test of our installed FESEM. It shows a resolution of 1.0 nm at 20 kV and 2.1 nm at 1 kV electron beam during the resolution test [92].

3.3.2.2 Gatan mono CL3 unit

During CL operation, the retractable paraboloidal light collection mirror is inserted manually to a position directly beneath the pole piece of SEM so that the electron beam passes through the 1 mm diameter hole of the mirror. Actual photograph of the mirror which is placed beneath the pole piece of SEM is shown in Figure 3.5 (a). Zoomed view of the CL parabolic mirror (views from top and bottom) is shown in Figure 3.5(b).

In order to get maximum efficiency of light collection, the top surface of the sample should be placed at the focal plane of the paraboloidal mirror (commonly called as 'hot spot'), otherwise no meaningful CL spectroscopy and/or imaging is possible due to very small signal to noise ratio. For setting up the 'hot spot' following procedure was taken: First the top surface of the sample was placed approximately 1 mm below the bottom plane of the mirror by a rough eye estimation. Next the the z value i.e. the distance from the mirror to the sample was adjusted several times with small step until panchromatic CL image of the shape shown in Figure 3.6(b) was detected on the CL control computer monitor from the luminescent portion corresponding

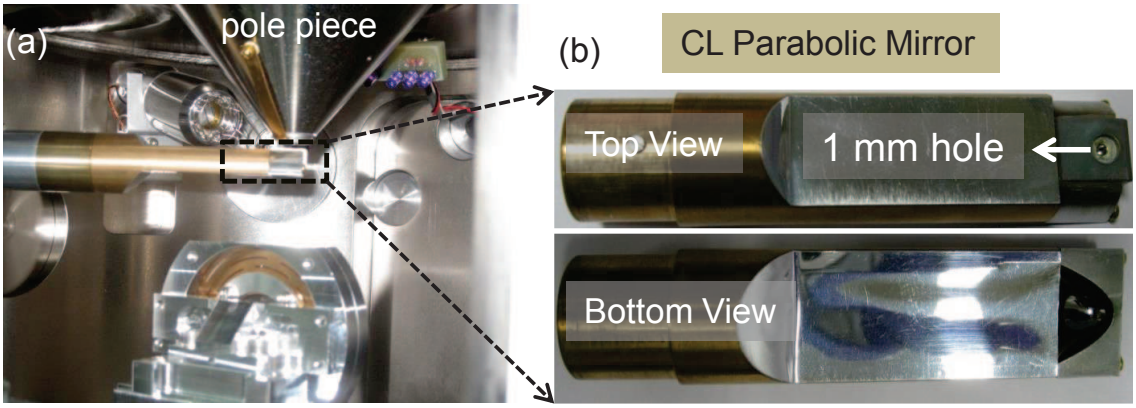

Figure 3.5: *(a) Photograph of the CL parabolic mirror and SEM pole piece. (b) Zoomed view of CL parabolic mirror (views from top and bottom).*

to the SE image (Figure 3.6(a)) of the area of the sample set at low magnification. This procedure was followed at the beginning of each experiment to ensure that the scattered light from the region of interest after reflecting from the mirror is correctly collimated. The mirror collects emitted light from the sample surface within a large opening angle 1.42π sr of the full 2π sr of upper hemisphere and collimate it through a hollow aluminum tube to a 300 mm Czerny-Turner type optical monochromator with a spectral band pass of approximately 11 nm. Finally the signal is fed to a Peltier cooled high sensitivity photomultiplier tube (HSPMT)(Figure 3.3 and 3.4) which can collect emitted photons in the optical range 160–930 nm. All the spectra presented here were taken in the serial mode, i.e. the grating was positioned for a particular wavelength and the reading was taken for a length of time which is known as dwell time, before the grating was moved to the next wavelength by a stepper motor.

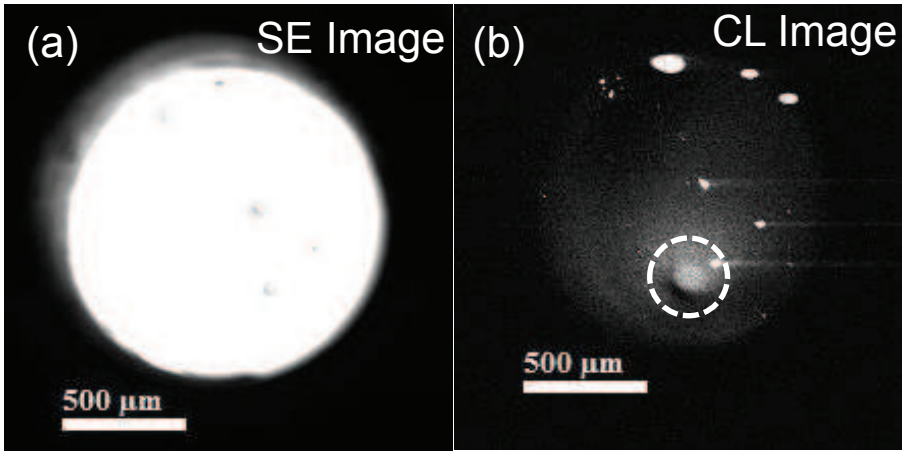

Figure 3.6: *(a) SE image at the lowest possible magnification of the sample and corresponding (b) Panchromatic CL image after height adjustment between the mirror and sample surface. The brightest zone encircled by white dots is the focal position of the specimen.*

3.3.2.3 Operational modes of the CL-SEM system

The combined CL-SEM system can be operated in either monochromatic mode or panchromatic mode. In monochromatic mode of CL operation, light passing through the monochromator allows taking the spectrum as well as CL images at a selected peak wavelength. In the monochhromatic mode of operation a dispersive element is included between the CL collector and the detector. As a dispersive element a diffraction grating monochromator has been used (in our case either 1200 lines/mm or 600 lines/mm), since this enables a desired spectral wavelength to be selected with ease. Before taking CL spectra from the sample under investigation, the wavelength calibration of the system is always checked using 404.66 nm mercury spectral line of an inline discharge lamp [92]. During taking spectra, the electron beam is scanned over the area of interest on the specimen or is kept at a fixed point (spot mode)

and the emitted luminescence spectrally analyzed. Final spectra are taken after averaging over 3 to 4 spectrum for each e-beam position and corrected from the substrate background. The monochromatic photon map is then built up at a selected peak wavelength of the emission spectrum by scanning the e-beam over the sample. For each e-beam position, the luminescence is collected over the entire sample. The bright pixels then correspond to the regions where the strongly excited plasmon mode emits the photons. Adding all the position dependent partial maps, obtained for each e-beam position, we obtain a full CL map of the plasmon mode associated with a particular wavelength. On the other hand, in panchromatic mode of imaging, light avoids the monochromator, and light containing all the wavelength is directly carried to the HSPMT to form the panchromatic photon maps. So in the CL image the contrast is caused by the variation of the photon counts or light intensity between any two points.

3.3.3 Basics of transmission electron microscope (TEM)

The crystalline structure analysis of as synthesized nanoparticles was carried out using a high resolution transmission electron microscope (HRTEM) (model: FEI, Technai G2 F30, S-Twin) operated at 300KV as shown in Figure 3.7. Transmission electron microscope (TEM) is a microscopy technique in which a high energy (200-300KV) beam of electrons is transmitted through an ultra-thin (electron transparent) specimen and interacts with the specimen as it passes through it. The interactions between the electrons and the atoms can be used to observe various features of the samples such as morphology, crystal structure and defects, crystal phases and composition.

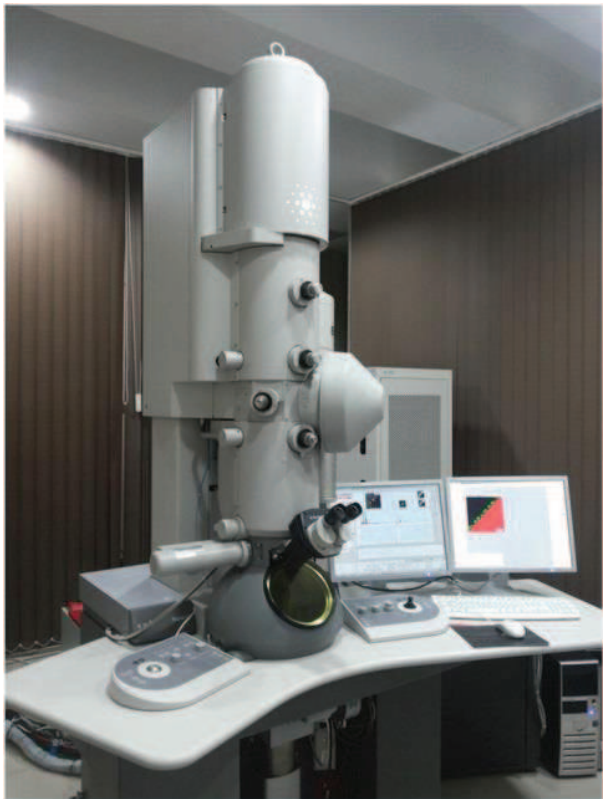

Figure 3.7: *The TECNAI G2 F30, S-TWIN FEI transmission electron microscope.*

The configuration of a TEM is shown schematically in Figure 3.8. The dashed vertical line shows the optic axis of the microscope. Field emission type electron gun made of LaB_6 crystal filament is commonly used in TEMs in modern days to achieve high current. Electrons from the gun (situated at the top of the microscope) are extracted using high voltage anodes and the diverging beam is focused and narrowed by a pair of condenser lenses, which are electro-magnetic in character. Some of the electrons in the beam, which travel at relatively larger angles with respect to the optic axis, are restricted from falling on the sample by a condenser aperture of controllable size placed below the condenser lenses. The specimen to be examined is usually placed at

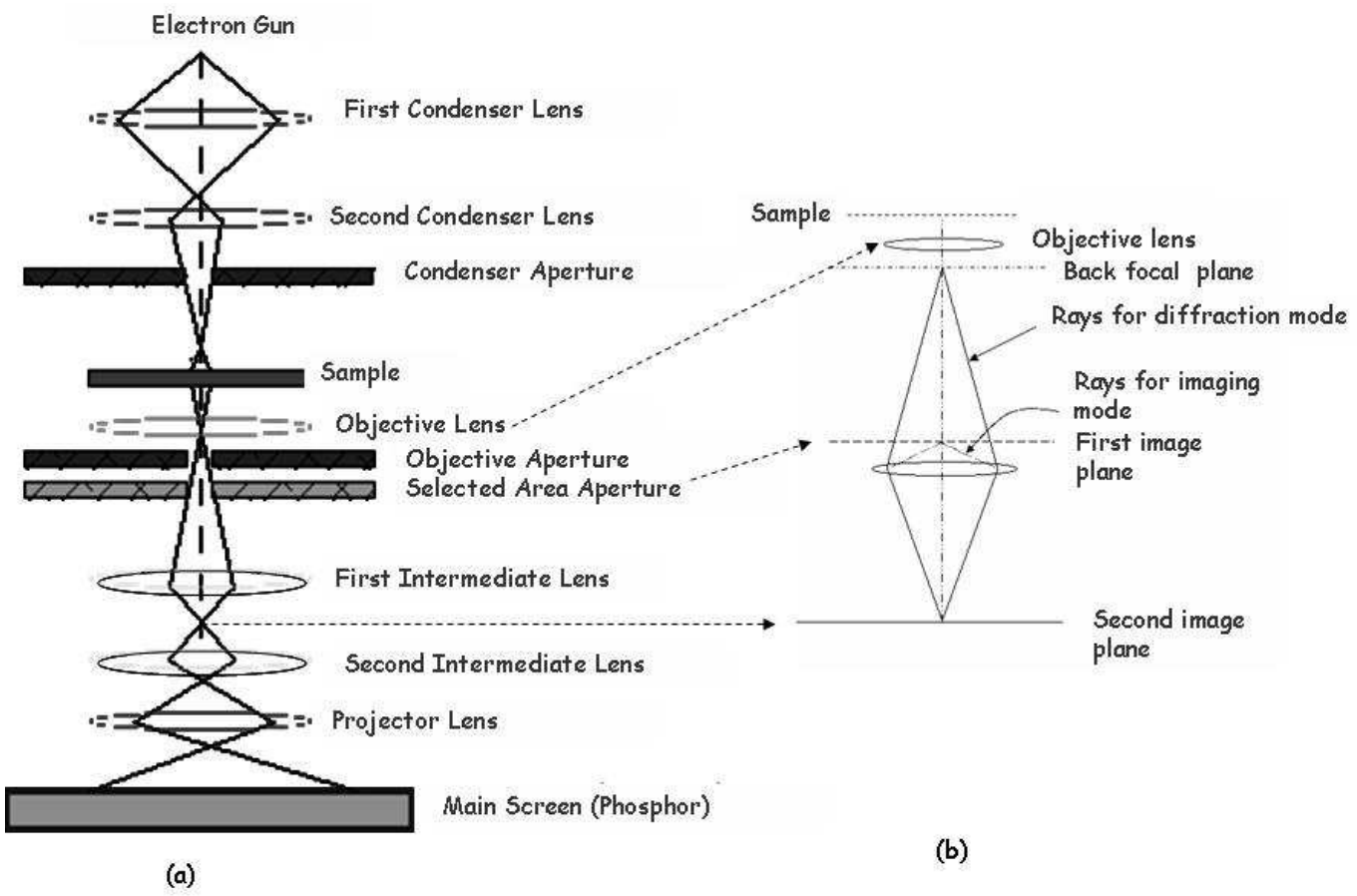

Figure 3.8: *A schematic layout of a transmission electron microscope and the focussing method for SAD and imaging.*

the object plane of the objective lens of the TEM. To obtain a clearly visible image on the phosphor screen, the sample is required to be electron transparent, i.e., thin enough, so that a large portion of the incident electron beam is transmitted through the sample. The transmitted portion of the electron beam is focused by the objective lens. An electron diffraction pattern of the sample area, illuminated by incident parallel beam of electrons, is formed at the focal plane of the objective lens (called back focal plane). The image of the illuminated sample area is formed at the image plane

(called the first image plane) of the objective lens. The electron diffraction pattern or the image, formed at image plane, is magnified on the viewing screen by the first and second intermediate lens and the projector lens assembly. In diffraction mode of operation, the first intermediate lens is adjusted in such a way that the back focal plane of the objective lens becomes the object plane of the first intermediate lens. In this case an electron diffraction pattern is seen on the viewing screen, which consists of a bright central spot on the optic axis and spots due to the diffracted electrons. An aperture of controllable size (called the selected area aperture) is placed at the first image plane. An area of interest can be selected from the sample image formed at first image plane by the selected area aperture. This selected area acts as a virtual source for the intermediate lens assembly so that only electron diffraction from this area can be observed in the viewing screen and is known as selected area diffraction imaging. In imaging mode of operation of the TEM, a spot from the electron diffraction pattern can be chosen for imaging by another aperture placed above the selected area diffraction (SAD) aperture which is called the objective aperture. To obtain an image of the sample, the first intermediate lens is adjusted so that the first image plane becomes its object plane. Depending upon the nature of selected electron beams contributing to the image, two types of images can be taken. One is the bright field image and other is the dark field image. If only the direct beam is selected for imaging by the objective aperture then the TEM image is called a bright field image. On the other hand, if any other diffracted beam with a specific direction is selected for imaging then the image is called a dark field image. During the transmission of electron beam through a sample, regions that are thicker or of higher density will

scatter the electron more strongly and hence more electrons will be scattered through an angle greater than 10^{-2} mrad making these areas appear darker in the image. This simple mass-thickness contrast is exhibited by all specimens, whether amorphous or crystalline.

In this thesis work, compositional analysis of chemically synthesized NPs have been performed with an energy dispersive spectrometer attached to the TECNAI G2 F30, S-TWIN FEI TEM (Figure 3.7), operated at 300 KV.

Chapter 4

Studying surface plasmons of isolated single polyhedral gold nanoparticles using CL combined with FDTD

CL spectroscopy and imaging of plasmon modes have been performed on isolated polyhedral gold nanoparticles. Two types of geometries namely decahedron and octahedron have been studied. The experimental results corroborate well with the FDTD numerical simulation.

PART I

4.1 Revealing the effect of substrate and observation of mode mixing on the plasmonic properties of an isolated decahedral gold nanoparticle

4.1.1 Introduction

Among metallic nanostructure of different geometry (like sphere, triangular prism, nanostar, decahedra, nanorod, etc.) the decahedron or pentagonal bi-pyramid shaped nanostructure has drawn substantial attention due to their inherent well defined anisotropy characterized by the presence of several sharp edges, corners and two acute apexes that are favourable regions of concentrating high electromagnetic (EM) field under LSPR condition. Consequently, the decahedron gold structures have important applications for LSP based biorecognition [66, 93–95] and SERS [96]. So far most of the experimental studies on the spectroscopy of Au decahedral particle [66, 93, 97] have been concerned with the optical properties of the collection of particles showing clear existence of two dipolar LSP modes, one along the azimuthal (along pentagonal base) and the other along the polar direction (along 5 fold symmetry axis). Moreover, it has already been reported from boundary element method (BEM) simulation with optical excitation [93] and dark-field microscopy (DFM) study [97], that with increase in particle size, these two modes are red shifted, broadened and new higher order (like, quadrupolar) mode arises. Strong electric field confinement at the corner points and apex of an isolated Au decahedron particles of size 60-120 nm have been a common observation in monochromatic CL or EELS images obtained from recent

local electron beam spectroscopy studies [43, 48]. Such local photons or electric field confinements are usually attributed with dipole active LSP modes for small particle size of around 65 nm [43]. For larger decahedron with a side edge length of around 110 nm one also observes additionally a transverse quadrupolar charge pattern [48]. With electron beam spectroscopy studies Myroshnychenko et al. [43] have shown mode splitting in contact with a substrate. Thus site specific electron probe provides additional spectral features that are not easily accessed by other optical tools.

With the increase of size of the decahedron particle, the size of corner edges running from pentagonal base to the apex becomes of appreciable sizes and the role of substrate also becomes important due to the enhanced contact area with the substrate supporting the particle. However, under external EM excitation the nature of the local EM field distribution around such corner edges and resulting changes in the modal distributions including the effect of substrate for such large decahedron noble MNP (of size larger than 150 nm) have neither been explored experimentally using local electron probe nor discussed in detail by electrodynamics based numerical simulations. The present study emphasizes on these aspects using CL spectroscopy and imaging in a SEM. Here, we report on the observation of mode mixing (existence of a mode along azimuthal and transverse direction at same wavelength) for an individual large Au decahedral NP (side edge length $\sim$ 230 nm). Detail analysis of the experimental spectra using FDTD simulations reveals two prominent LSP modes in the visible region of the emission spectra where the shorter wavelength (560 nm) mode has a mixture of in-plane quadrupolar and out-of-plane quadrupolar charge distribution pattern and the longer wavelength (655 nm) mode has the dipolar charge pattern

in both the direction. We also show that how the effect of substrate can give rise to a new LSPR mode in the near-infrared region of the observed CL spectrum.

4.1.2 Methods

4.1.2.1 Experimental

The synthesis of decahedral Au nanoparticles were performed using seed mediated chemical growth process, the details of which have been described in Chapter 3. CL spectroscopy and imaging on isolated single Au decahedral nanoparticle was performed in a ZEISS SUPRA40 SEM equipped with the Gatan MonoCL3 CL system. We have already described the details of CL-SEM system in Chapter 3. In the present study, data were recorded with an electron acceleration voltage of 27 kV and beam current of about 12 nA with a beam diameter of approximately $\sim$ 5 nm. The spectral band pass is $\sim$ 11 nm during spectrum acquisition. In monochromatic mode, the focused e-beam is either scanned over the sample or positioned on a desired spot while light emitted from the sample passes through the monochromator allowing us taking the emission spectra to be recorded serially in the wavelength range 500-900 nm with a step size of 4 nm and a dwell time of 0.5s. The monochromatic photon maps, presented in this Chapter are recorded with 150 $\times$ 150 pixels and each pixels corresponds to a length of 5.2 nm.

4.1.2.2 FDTD simulations

For detailed understanding of the plasmon assisted photon emission and the corresponding features, such as charge distribution, near field intensity maps, and effect of

substrate on the Au decahedral nanoparticle, we have performed 3D-FDTD numerical simulation (from Lumerical solutions, Canada). The details of FDTD Simulations have already been described in Chapter 2. To describe the wavelength dependent dielectric constant of gold metal we use experimentally measured gold permittivity data from CRC Handbook of chemistry and physics [88]. In our FDTD modelled structure, we introduce roundness with a radius of curvature of 15 nm in all the corners and in both the apexes of decahedra in order to achieve convergence, which is also consistent with the morphology obtained from the SEM image. We have used Si substrate as a non-dispersive material with fixed refractive index 4 [48] and having a dimension of 5 μm $\times$ 5 μm $\times$ 2 μm throughout our numerical simulation.

4.1.3 Results and discussions

In the present study, we report specifically on spectral and spatial probing of different surface plasmon modes in an isolated single Au nanodecahedron of side edge length (L)$\sim$ 230 nm. The morphology of the decahedron under study is depicted in the SE image of Figure 4.1 (a), where pentagonal base corner points and apex are marked as 1-5 and 6 respectively. To obtain a clear picture of the original morphology of the decahedron we have tilted the sample stage at an angle $\sim 60^{\circ}$ and the corresponding tilted image is shown in the SE image of Figure 4.1 (b). Although tilting the stage is allowed for SE imaging, we are restricted to perform CL experiment in the non tilted configuration (Figure 4.1 (a)) of sample stage due to the preconfigured parabolic mirror and sample stage combination optimized for maximum light collection. From Figure 4.1 (b), it is clear that decahedron in this present study is supported on

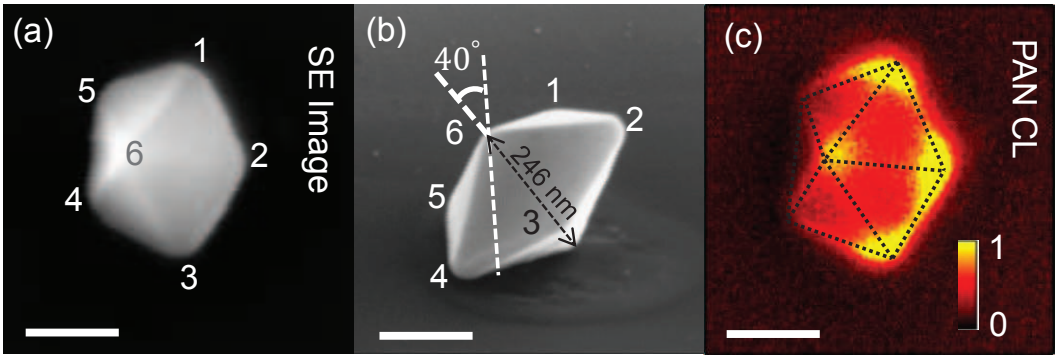

Figure 4.1: *(a) Secondary electron (SE) image of an isolated single gold decahedron on silicon (100) substrate. (b) SE image of the decahedron in tilted condition. (c) Panchromatic CL image of the decahedron shown in (a). The scale bar in all the images is 200 nm.*

the silicon (Si) substrate with one of its faces (in this case along side 4-5) touching to the substrate. For a regular pentagonal bipyramid the well known geometrical relationship between geometrical height (h) and side edge length (L) is given by the formula

$$h = \frac{1}{10}\sqrt{50 - 10\sqrt{5}}L \tag{4.1}$$

where h is defined as the distance from the center of pentagonal base to tip apex. After necessary tilt correction, we have measured the distance between two tips (apex), 2h, to be $\sim$ 246 nm. So, the experimentally measured h of 123 nm for the decahedron under consideration is very close to the h value estimated from the geometric formula of the pentagonal bipyramid whose side edge length, L = 230 nm. The panchromatic CL image of the decahedron corresponding to the left SE image (Figure 4.1 (a)) is shown in Figure 4.1 (c), which clearly shows localized surface plasmon induced luminescence. It is interesting to note that strongest photon emission is observed only from the three corner points marked as 1, 2, 3 of the pentagonal base and apex (point

6) of the decahedron where as radiated photon emission from corner points 4 and 5 is very much weak (Figure 4.1 (c)). This is due to the fact that LSPR induced radiation from these two corner points are absorbed by the high index substrate (Si) (as these corner points are in touch with the substrate) resulting a reduction in the amount of light in CL detector. Similar observation is already reported by Das et al. recently [48]. In order to get spectrally resolved features, CL spectroscopy and imaging have been performed in the monochromatic mode as shown in Figure 4.2. In Figure 4.2 (a), we have examined site specific CL spectra in the wavelength range 500-900 nm taken from different positions of the decahedron indicated on the SEM image (inset). The complete spectra were taken in two different wavelength ranges, 500-800 nm and 800-900 nm and then merged after proper normalization. In the experimental CL spectra (Figure 4.2 (a)), three major resonant peaks are detected at $\sim$ 560 nm (mode A), $\sim$ 655 nm (mode B) and 750 nm (mode C) respectively when the electron beam impinges at point 1. These resonant peaks appear at 580 nm (mode A), 650 nm (mode B) and 790 nm (mode C) respectively in the calculated spectra for excitation over point 1. However, when the electron probe moves to point 2, which is farthest base corner point from the substrate (Si), we found only two noticeable resonance peak around 564 nm (mode A) and 660 nm (mode B). Our experimental observation is well supported by theoretically simulated CL spectrum which shows that only mode A and mode B exist for excitation over point 2. As point 1 and 3, are two symmetric base corner points with respect to height from the Si substrate, one should expect similar type of spectral behaviour for excitation over point 1 or 3 which is indeed revealed in our FDTD simulated spectra. However, in our experimental spectra, when

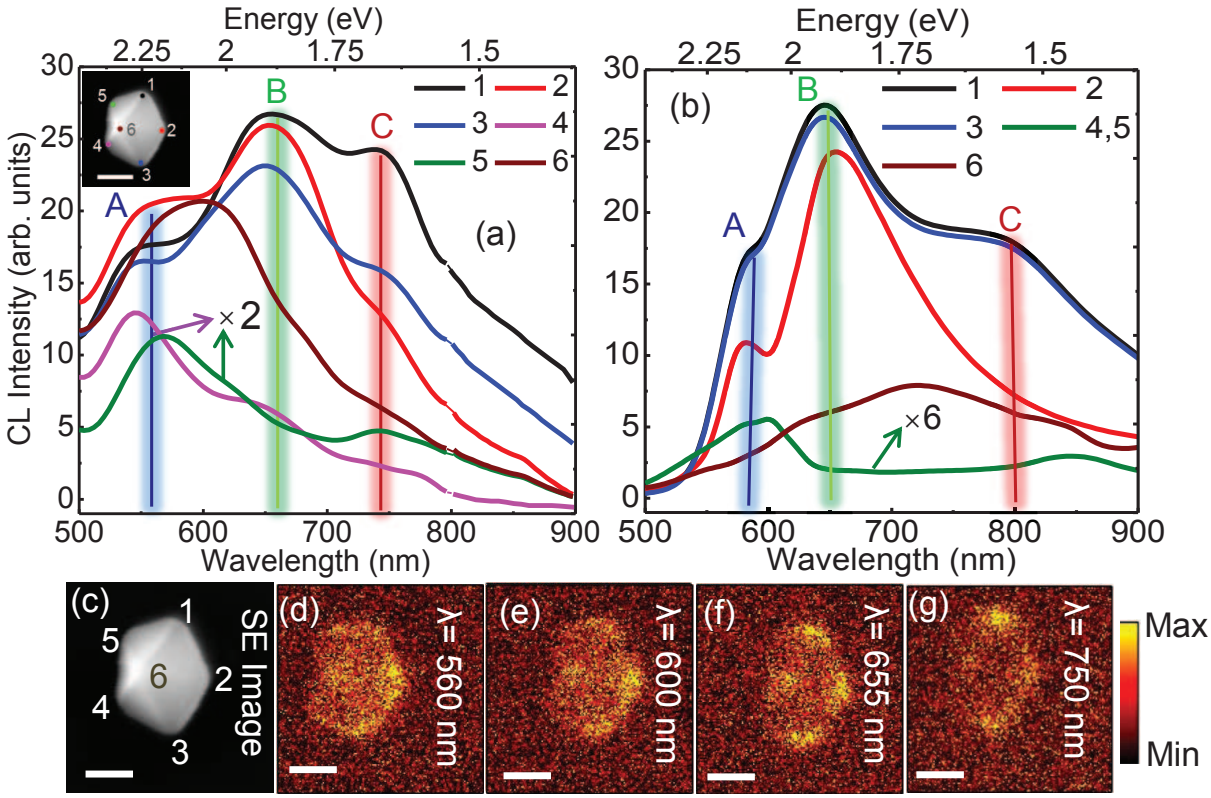

Figure 4.2: *(a) Experimentally obtained CL spectra from different beam injection positions (marked as 1, 2, 3...6) of the decahedron. The inset SE image shows the e-beam impact points with different colored dots. (b) 3D-FDTD simulated CL spectra of the same morphology as shown in the inset of (a). (c) The SE image of the gold decahedron and the corresponding monochromatic CL maps for the selected resonance wavelengths (d) 560, (e) 600, (f) 655, and (g) 750 nm. The scale bar in all the images is 200 nm.*

we excite at point 3, we observed all three modes (mode A, mode B and mode C) remain almost at the same position when compared to that excited at point 1, but intensity of the mode C is reduced drastically as compared to that for excitation over point 1. The mismatch in spectral peak position and peak intensity between experimental and simulated spectra can be attributed to several factors, such as imperfect modelling of the decahedron morphology, possibility of presence of CTAB surfactant

layer between particle and substrate causing a change of dielectric environment not considered in the simulation, small drift of the specimen during spectral data acquisition etc. Now,when the electron beam impact point is shifted towards point 4 or 5, a very weak resonance peak was observed around 550 and 570 nm respectively with intensity about 4.5 times smaller than observed highest intensity, which is also reflected from pan CL image. When we excite at point 6 i.e. apex region of the decahedron, a strong polar mode with a broad resonance peak was found around 600 nm (fwhm 160 nm) with an intensity about 1.3 times smaller than highest observed peak intensity at 655 nm. In the previous CL studies on Au decahedron of side edge length $\sim$ 110 nm by Das et al. [48], the polar mode was weak compared to the present one and appeared at 530 nm with relatively lower fwhm (70 nm) for excitation over the apex. Thus, experimentally, we observe more than two fold increase in the broadening and red shift of about 70 nm of the polar mode caused by about two fold increase in the size of the decahedron used in the present study as compared to our previous study [48]. However,in our calculated spectra (Figure 4.2 (b)), the polar resonance peak was found at around 720 nm with two small shoulders at around 560 and 610 nm respectively. This might be due to the fact that throughout our FDTD simulations we have used same curvature (15 nm) for the entire pentagonal base corner as well as tip apexes which may not match those of the decahedron morphology observed in SEM. It is well known that edge and tip curvature [97, 98] can strongly effect the spectral position and width of the plasmon bands. Also, in the simulation, the point 6 is excited assuming it as a mathematical symmetry point, whereas experimentally due to finite width of e-beam, uncertainty in the perfect alignment with respect to the

point 6 may give rise to the discrepancy between the calculated and experimentally observed CL spectra.

After having spectral distribution (Figure 4.2 (a,b)), we proceed to collect information of the resonant modes in spatial domain which is depicted in the monochromatic CL maps of Figure 4.2 (d-g) for different resonant wavelengths (560 nm, 600 nm, 655 nm, 750 nm). From the monochromatic CL images, a change in spatial distribution in the intensity of the emitted photons over a length scale much smaller than the wavelength of light is clearly observed. The bright spots in the photon maps arise when LSP modes are resonantly excited by the evanescent field associated with electron beam. The monochromatic CL image corresponding to mode A at 560 nm (Figure 4.2 (d)) shows intensity maximum along the edge whereas photon map corresponding to mode B at 655 nm (Figure 4.2 (f)) shows maximum luminescence coming from the pentagonal base corner points. Also photon maps at these two modes (mode A and mode B) reveal (Figure 4.2 (d,f)) a considerable luminescence from tip apex (point 6) which is also consistent with our spectroscopic data (Figure 4.2 (a)). This means there might be a mode mixing (existence of transverse as well as longitudinal mode at the same wavelength) occurring in these two modes (mode A and B). On the otherhand monochromatic photon maps corresponding to mode C at 750 nm (Figure 4.2 (g)) gives rise to maximum photon emission coming from pentagonal base corner point 1 than any other point which is consistent with our spectroscopic data of Figure 4.2 (a).

4.1.3.1 Substrate influence on the LSPR spectrum

Recently, decahedral nanocrystals have been proposed as a biosensors [66, 93, 97]. In order to fabricate a biosensing device, the particle should be supported on a substrate. So investigation on the effect of substrate on CL spectra is very much crucial. For an anisotropic particle like decahedron, the effect of substrate is not trivial. In order to examine the effect of substrate, we vary the distance between a face of the decahedron particle and Si substrate in our FDTD simulations (Figure 4.3 (a)), keeping the e-beam excitation on point 1. As we increase the distance between particle and substrate (Figure 4.3 (a)), mode A and mode B remain at the same position. However, mode C shows a blue shift and ultimately disappears when the separation between particle and substrate becomes $\sim$ 10 nm, clearly indicating the role of substrate to the origin of mode C. To further understand these results, in Figure 4.3 (c,d), we vary substrate refractive index (R.I.) from 1 (air) to 4 (Si) and examine the calculated CL spectra for different point of excitation on decahedron (Figure 4.3 (b)). We noticed from Figure 4.3 (c), that for electron beam impact at point 1, lower wavelength peaks in the visible region, i.e., mode A and mode B remain almost at the same position. However, if the R. I. is increased from 1 (R.I. of air) to 1.5 the mode C starts to appear as a small hump around 720 nm. For further increase in the R. I. of the substrate, the mode C becomes prominent and a gradual red shift (shown by a dotted arrow in Figure 4.3 (c)) with increasing substrate index is clearly discernible. Finally, the mode C appears at 790 nm while the R. I. reaches at a value 4 (Si substrate). The red shift (of substrate induced mode C) is consistent with all known literature, and also with Figure 4.3 (a), where a shift is seen as a function of separation between

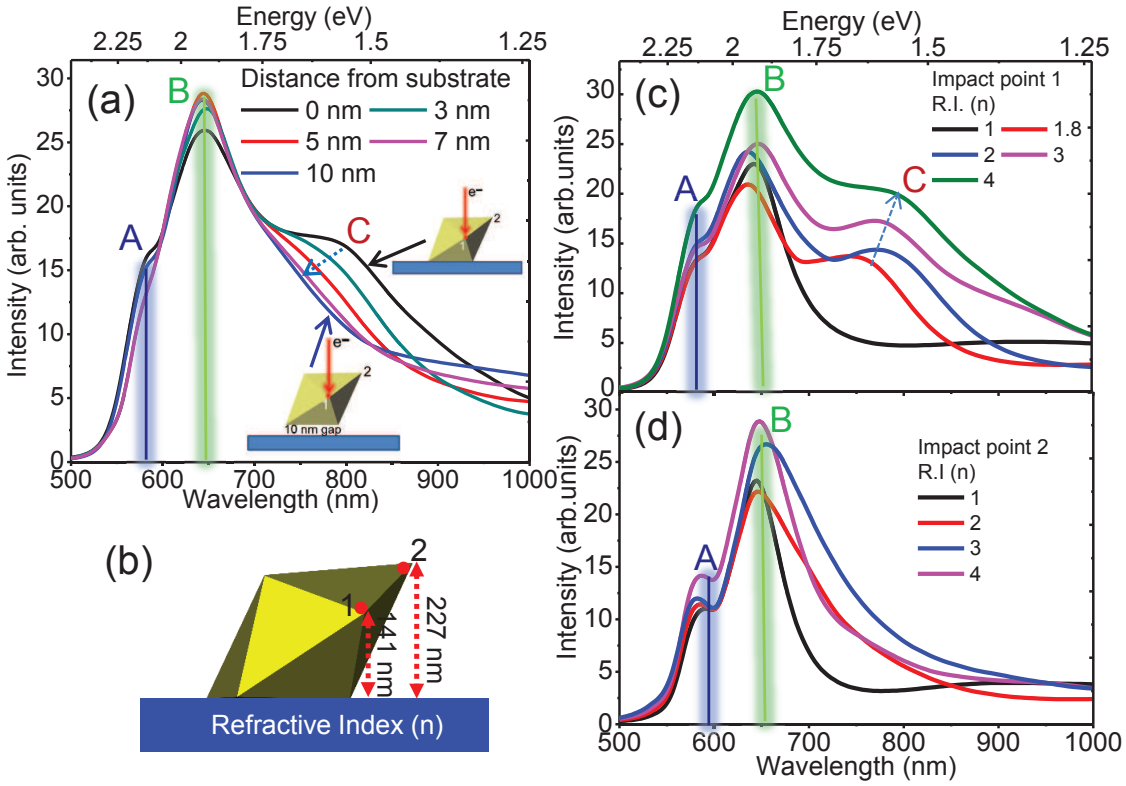

Figure 4.3: *(a) Calculated CL spectra showing mode C gradually disappears with increasing separation between particle and substrate. The inset in (a) shows the model structures used. (b) Distance of the corner points 1 and 2 from the substrate for the decahedron used in the modelling. (c)-(d) Effect of variation of substrate refractive index (R.I.) on simulated CL spectra for two different e-beam impact points (marked as 1 and 2 as shown in (b)).*

one face of the tilted decahedron and Si substrate (which can be seen as the varying influence of a varying index that depends on the distance between the particle and the substrate to a first approximation). The simulation also shows that for excitation over point 2, although mode A and mode B sustain, but mode C is not observed with the similar variation of the refractive index of the substrate. The nature of calculated emission spectra agrees reasonably well with the experimental one for e-beam excitation over point 1 and 2 except that mode C in the experimental spectrum

is blue shifted compared with the theoretical one. The appearance of the new peak at 750 nm (experimental) / 790 nm (calculated) in case of excitation over point 1 as observed in experiment and numerical simulation might be due to the fact that point 2 being situated far away from the substrate (227 nm away from substrate) as compared to the point 1 (141 nm away from substrate) and thereby not affected significantly by substrate. So we can say that the resonance peak mode C is due to particle-substrate interaction. Appearance of a new peak for a single silver nanocube in presence of a glass substrate is observed by sherry et al. [60], at the lower wavelength region when nanocube approaches towards dielectric substrate. In contrast to this we have found a substrate induced LSPR mode (mode C) in the higher wavelength region (near infrared). Previous CL study on gold decahedron (side edge length $\sim$ 110 nm) by Das et al. [48] also illustrated the effect of substrate on the LSP modes. Ringe et al. [58] reported appearance of transverse quadrupolar mode for the excitation of a corner point of the nanocube located farthest from the substrate and a dipolar mode for the excitation of the corner point nearest to the substrate which they call as distal and proximal mode respectively for silver nanocube. In the next session we will explore the origin of the different modal distribution corresponding to different resonance modes.

4.1.3.2 Assignment of luminescent modes

In Figure 4.4 (a), we have examined nature of the CL spectra using FDTD simulations for different tilt angle of the decahedron i.e. from actual configuration (tilt angle 40°) to vertically oriented decahedron (tilt angle 0°), keeping the electron beam fixed at

point 2. From Figure 4.4 (a), it is very much clear that mode A and mode B remain almost unaffected during tilt angle variation except the increase in intensity while going from 40° to 0°. In the lumerical FDTD software used here, the 2D power monitor (the rectangular planes XY, XZ and YZ shown in Figure 4.4 (b)) that calculate the

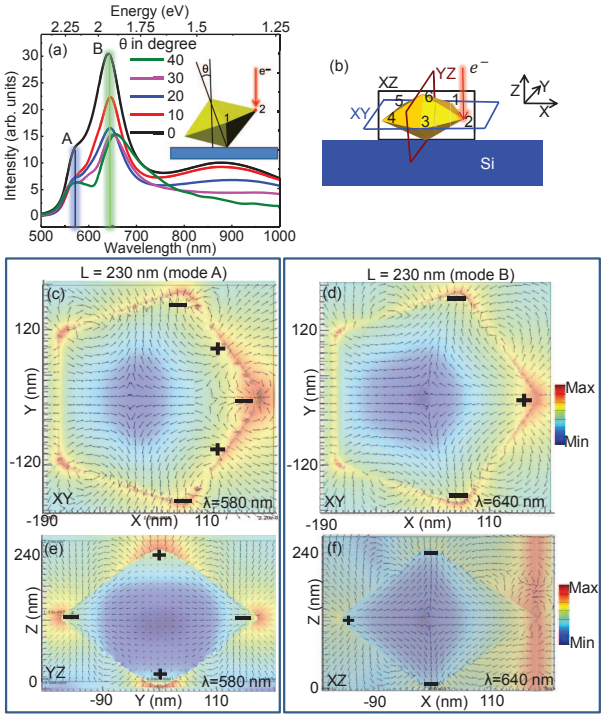

Figure 4.4: *(a) Calculated CL spectra for e-beam excitation at corner point 2 for different tilt angle (θ) of gold decahedron with respect to the substrate normal.(b) Geometrical configuration along with the coordinate system of the non-tilted decahedron of side edge length 230 nm on Si substrate used in the numerical modelling. Power monitors were placed in XY, YZ and XZ plane in order to calculate the near field intensity and charge distributions. Simulated near field E intensity ($|E|^2$) maps and corresponding vector plot of E field overlaid on it at different resonant wavelengths (c) 580 nm in the XY plane (d) 640 nm in the XY plane (e) 580 nm in the YZ plane (f) 640 nm in the XZ plane.*

electric field maps can be oriented either vertically or horizontally, i.e., in mutually orthogonal positions and no options exists for inclined positions. For this constraint

we are not allowed to calculate the field distribution for the tilted configuration of the decahedron. Consequently, for proper investigation of different modes of LSP oscillations arising in the gold decahedron, we carried out FDTD simulation assuming the decahedron particle to be aligned vertically (tilt angle 0°) on Si substrate and electron impact at point 2 as shown schematically in Figure 4.4 (b). In this non-tilted configuration all five base corner points (labeled as 1, 2,...5) of the equatorial plane are equivalent with respect to 5 fold symmetry axis. The simulated electric-field intensity maps and the corresponding vector plots of the electric field distribution overlaid on it for the mode A and mode B is shown in Figure 4.4 (c-f). The simulated vector maps of Figure 4.4 (c,e) reveal that the mode A (580 nm) consists of an azimuthal quadrupolar induced charge pattern oscillation (Figure 4.4 (c)) along the in-plane edges of the pentagonal base and a transverse quadrupolar charge pattern oscillation (Figure 4.4 (e)) along the out of plane corners edges of the decahedron. Similar vector plots, however for mode B (640 nm) reveals the dipolar nature where charges with opposite polarity (±) could be accommodated at two nearby corners like 1-2, 2-3 etc. in the azimuthal (Figure 4.4 (d)) direction (i.e. along the in-plane pentagonal base) or in the out-of-plane direction along the corner edges (Figure 4.4 (f)). From the induced near-field electric intensity ($|E|^2$) maps (Figure 4.4 (c-f)), we see that the mode B corresponding to the combination of azimuthal and transverse dipolar charge oscillations show large field enhancement at the pentagonal base corner points and at the apex of the decahedron which is consistent with the enhanced luminescence observed experimentally (Figure 4.2 (f)) in the monochromatic CL image corresponding to the CL peak wavelength 655 nm. On the otherhand, the mode A which comprises

of azimuthal quadrupole plus out-of-plane quadrupolar charge pattern, exhibits the near-field enhancements at the pentagonal base corners, side edges as well as the apex of the decahedron consistent with the enhanced luminescence observed experimentally (Figure 4.2 (d)) in the CL map at the peak wavelength 560 nm. It is obvious that the modes A and B at the resonant wavelengths 580 nm and 640 nm considered in the modelling for an non-tilted decahedron refers to the resonant peaks 560 nm and 655 nm of the CL spectra obtained experimentally (Figure 4.2 (a)) from the tilted decahedron supported on the Si substrate of the present case.

It is interesting to note that in the the previous studies on gold decahedron (side edge length $\sim$ 110 nm) by Das et al. [48] it was shown that a transverse quadrupolar mode appeared at 544 nm for excitation at corner point 2 of the decahedron whereas excitations at the other corner points (point 1 and 3) were dominated by azimuthal dipolar resonance at 580 nm (fwhm 82 nm). However, in the present study, where the dimension of the Au decahedron is more than double of the previous one, our analysis clearly reveals that the mode B (655 nm with a broadening of 113 nm) is not a pure azimuthal dipolar mode rather it is mixed with a transverse dipolar charge pattern along the corner edges (that meet the apex) of the decahedron. Similarly the shorter wavelength resonance (560 nm with a broadening of 62 nm), i.e., mode A does not correspond to a pure azimuthal quadrupolar mode, instead consists of a mixture of azimuthal quadrupolar (along pentagonal base) and transverse quadrupolar (along the corner edges meeting the apex) charge patterns. The higher order charge distribution other than dipolar distribution as reflected from the vector plots of Figure 4.4 (c,e) arise from retardation of the electromagnetic field as it propagates along the extension

of the particle. Obviously, the increase in the axial height (pentagonal base to the apex) caused by the increase of the lateral size increases also the lengths of the corner edges running from base to the tip. This in turn, favours to accommodate charge distribution pattern along the corner edges (Figure 4.4 (e,f)) and as a result one observes luminescence from the corner edges in the experimentally obtained mono CL image (Figure 4.2 (d,f)). Consequently, they are more pronounced in larger particles employed in the present study as compared to the small decahedron particle used in our earlier study [48]. This means in the present case, we have more efficient coupling to the external light (here evanescent wave associated with the electron probe) via a larger polarizability. A stronger coupling signifies shorter lifetimes of the particle-bound modes under consideration because of leaky nature of the freely propagating light. As a result, one encounters the effect of mode mixing in a manner that spectral features originate on a background coming from the broadening of other features. Observation of such mode mixing for large decahedron structure of Au has not been reported so far using single particle spectroscopy tool to the best of our knowledge, although results on similar mode mixing for large decahedron particle (size smaller than the present particle) were predicted through BEM numerical simulation [93] for optical excitation. One of the advantages of the local electron beam excitation over optical excitation is that a fast moving electron beam has evanescent field both along the direction of propagation as well as perpendicular to the e-beam. For this reason, electron beam can efficiently excite both the modes along the beam and perpendicular to the beam with increasing the size of the decahedron.

4.1.3.3 Dependence of mode mixing on decahedron size

In the present synthesis of the decahedral Au particle we don't have substantial variation of the size of the particles to study experimentally the dependence of the CL spectra on the particle size for analyzing the critical size of the Au decahedron where mode mixing occurs. So, for deeper understanding on the dependence of the mode mixing on the Au decahedron particle size, we have performed systematic analysis using FDTD numerical method. To understand the effect of mode mixing as a func-

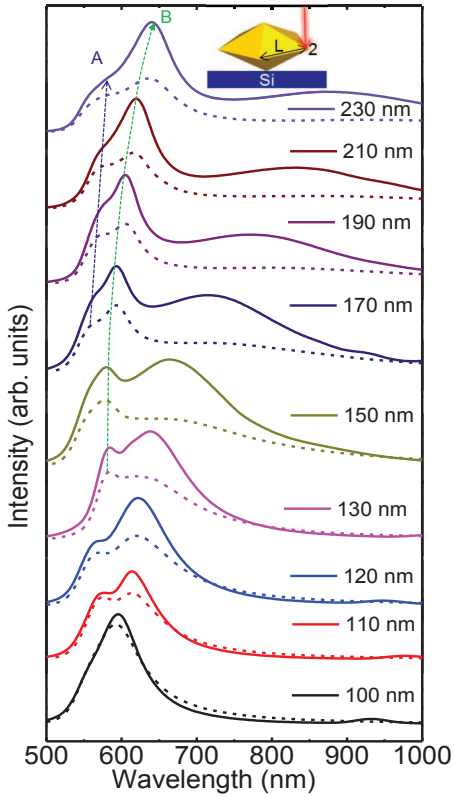

Figure 4.5: *Simulated CL spectra of Au decahedra for different side lengths where the solid curve denotes the presence of substrate and the dashed curve implies absence of substrate. All the spectra are taken in the non-tilted configuration of the decahedron, keeping e-beam fixed at corner point 2 (as shown in inset).*

tion of size parameter, we have calculated CL spectra (Figure 4.5) of a single Au

decahedron by varying its edge length from 100 nm to 230 nm. In Figure 4.5, all the CL spectra are calculated assuming vertical (non-tilted) orientation of the decahedron with e-beam excitation at pentagonal base corner 2 (as shown inset Figure 4.5). The red shift and broadening of the LSPR modes with the increase of the particle size are

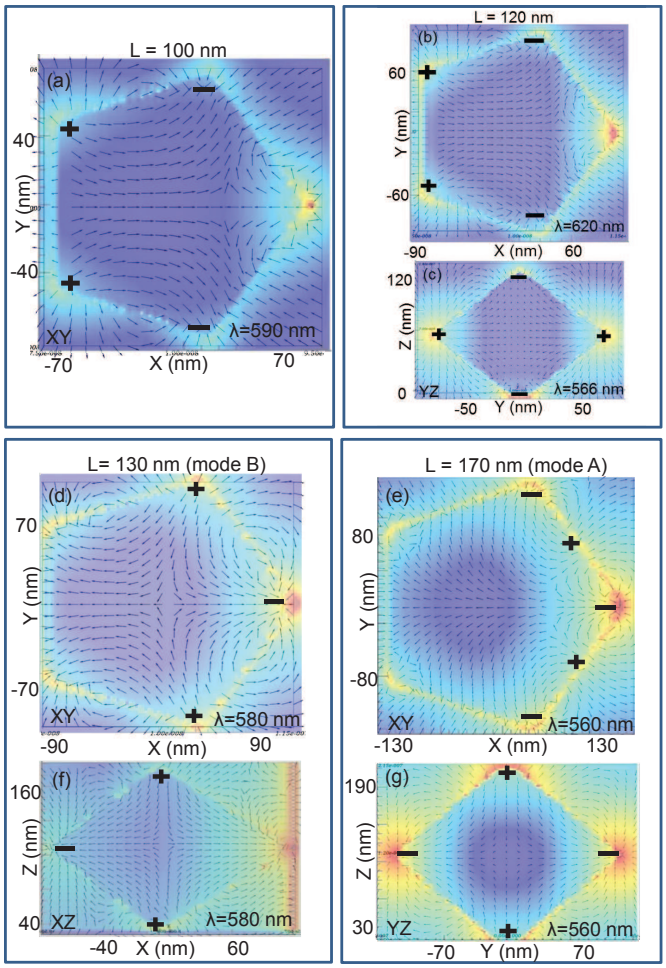

Figure 4.6: *(a-g) Simulated near field E intensity ($|E|^2$) maps and corresponding vector plot of E field overlaid on it at different resonant wavelengths for different particle sizes. Mode mixing occurs at a critical side edge length of 130 nm.*

clearly observed from the calculated spectra of Figure 4.5 which is well-known in the

metal nanoplasmonics. The peak observed at 590 nm for 100 nm edge length is a pure azimuthal dipolar mode as shown in vector plot of Figure 4.6 (a). When the particle edge length becomes 120 nm the dipolar mode (as confirmed from the vector plot of Figure 4.6 (b)) red shifts to 620 nm and a new peak arises at the lower wavelength of about 566 nm which shows a pure transverse quadrupolar charge oscillation (vector plot of Figure 4.6 (c)). This is consistent with the previous finding by Das et al. [48] where they have identified a pure transverse quadrupolar mode at 563 nm and a pure azimuthal dipolar mode at 610 nm on a non-tilted gold decahedron of edge length 110 nm. However, when the particle size becomes 130 nm, we find a mixed mode B

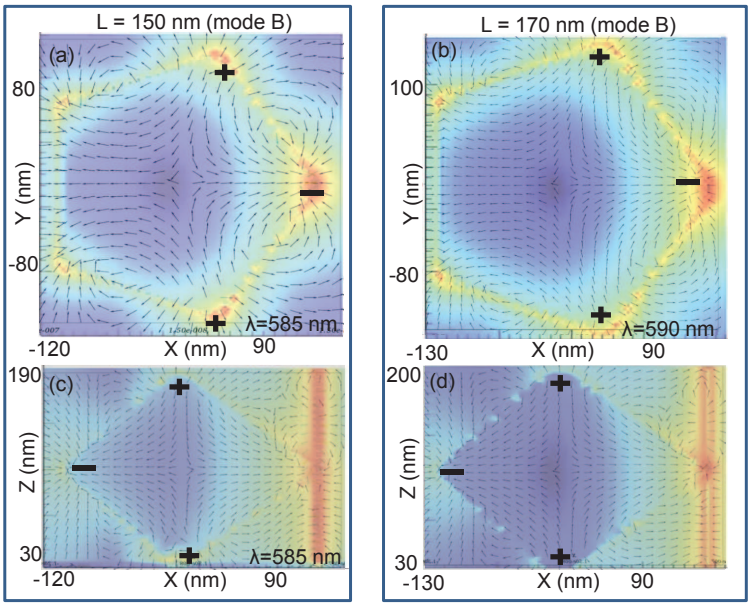

Figure 4.7: *(a)-(d) Simulated near field intensity map and corresponding vector map of the electric fied overlaid on it at different resonant wavelength for decahedron of edge length 150 nm and 170 nm.*

(dipolar charge pattern along both azimuthal and transverse direction) appearing at 580 nm (corresponding vector plots shown in Figure 4.6 (d,f)). With further increase

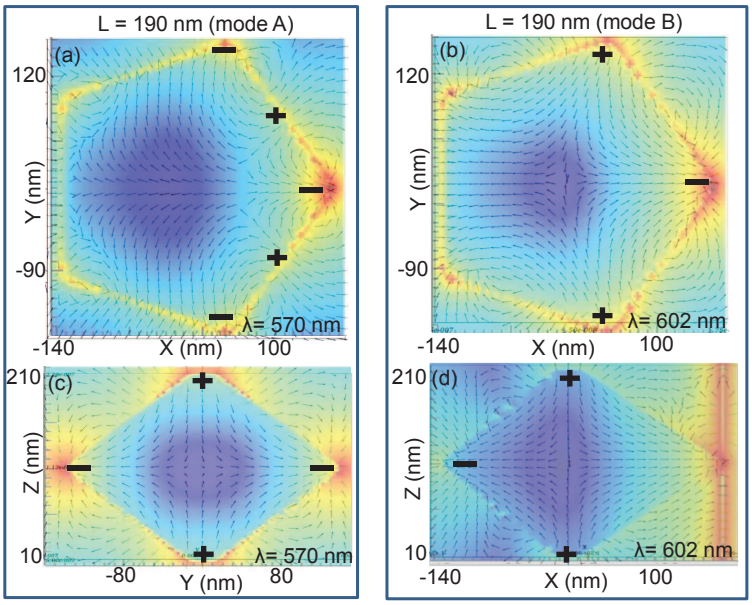

Figure 4.8: *(a)-(d) Simulated near field intensity map and corresponding vector map of the electric fied at 570 nm and 602 nm for decahedron of edge length 190 nm.*

of particle size the mode B is gradually red shifted and a new mode (mode A) starts to appear at the shorter wavelength of about 560 nm for the decahedron with edge length of 170 nm. The vector plots in Figure 4.6 (e,g) clearly reveal that the nature of this mode A is nothing but a mixed one (quadrupolar charge pattern along both azimuthal and transverse direction). Finally, the mode A and B appears at around 580 and 640 nm in our calculated CL spectra for the decahedron of edge length 230 nm. So from above analysis we can conclude that the mode mixing starts to begin for a Au decahedron with an edge length of 130 nm for a single resonance peak (mode B) below 600 nm. However, existence of two mixed modes A and B is only possible when the decahedron edge length is about 170 nm or above. The vector plots of mode mixing for the decahedron with intermediate side lengths are shown in the Figure 4.7, 4.8, and 4.9 respectively. It is also interesting to note that the pure azimuthal dipolar

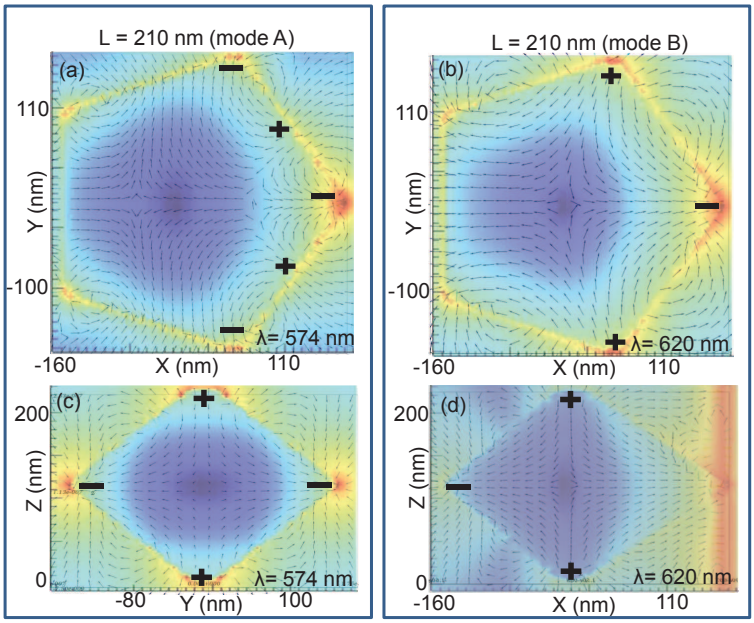

Figure 4.9: *(a)-(d) Simulated near field intensity map and corresponding vector map of the electric fied at 574 nm and 620 nm for decahedron of edge length 210 nm.*

mode which appears at 590 nm (both in presence and absence of substrate) for an Au decahedron with edge length 100 nm gradually redshifts and broaden with increasing particle size. However, above 150 nm edge length, we find that this mode almost vanishes in absence of substrate (dashed curve) but shows a weak peak in presence of substrate with enhanced broadening as the edge length increases. Very recently, it is shown by Li et al. [35] that for truncated Ag sphere in free space, electron beam preferentially interacts low order modes i.e dipolar mode for small size particles but it almost vanishes for a particle with a size of about 200 nm which is quite consistent with the present analysis in absence of substrate (spectra with dashed curve in Figure 4.5). But in our case, a weak peak was observed in the higher wavelength region for size above 150 nm in presence of substrate. This might be attributed to the contribution from the transverse component of LSPR mode to the CL spectra as discussed

in detail in our earlier studies of facted nano rod [47] in presence of substrate using the so called image charge model.

As we have shown that the origin of mode C is related to the substrate, for deeper understanding of LSP oscillation of mode C, we calculate CL spectra for different tilt angles (θ) of the decahedron with respect to substrate normal, keeping the e-beam fixed at corner point 5 (Figure 4.10 (a)). It is noted that with increasing tilt angle, mode B (at 640 nm) is gradually red shifted with reduced intensity in addition to the appearance of peaks around 550 nm and 600 nm in the visible region. Increase of tilt

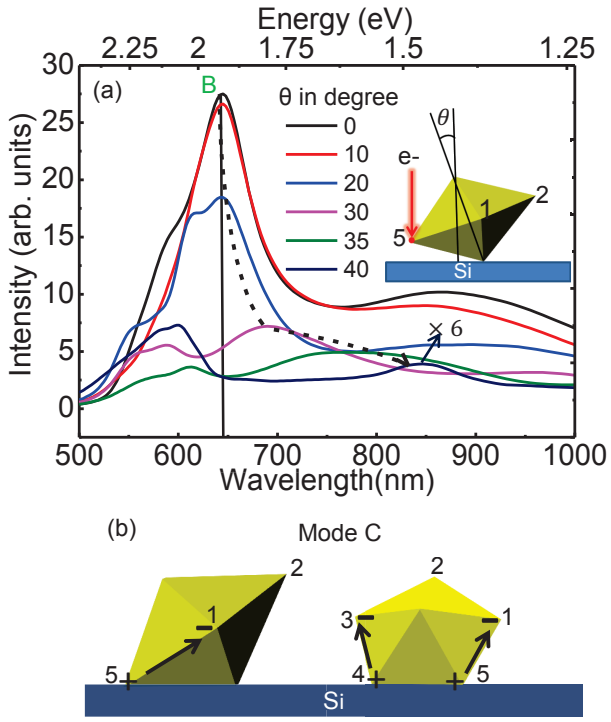

Figure 4.10: *(a) FDTD simulated CL spectra for e-beam excitation at corner point 5 for different tilt angle (θ) of gold decahedron with respect to the substrate normal. Dotted arrow shows that the dipolar mode is red shifted to around 840 nm (w.r.t to the peak at 640 nm for non-tilted configuration) in tilted configuration. (b) Schematic of the orientation of the decahedron on Si substrate and probable model charge oscillation of mode C in this tilted configuration.*

angle basically means, point 5 gradually becomes more closer to the substrate and the emitted photons are mostly absorbed into the substrate making the loss channel for the far field radiation a dominant one to show up reduced intensity at the resonance peak beyond 640 nm for the tilted configuration of the particle. It is well known that red shift increases with the increasing refractive index of the substrate and the proximity of the particle with the substrate [13, 61, 73]. Consequently, when one of the faces of the decahedron touches to the substrate (tilt angle 40°), i.e. coincides with the actual configuration of the experimental situation, mode B red shifts (shown by a dotted line in Figure 4.10 (a)) from 640 nm (for non tilted case) to around 840 nm (tilted case) for excitation over point 5. Along with this red shift and decrease in intensity, we also found broadening in the mode B due to increase of radiative damping with increasing tilt angle of the decahedron. In our theoretical study we found mode C appears (Figure 4.2 (b) or Figure 4.3 (a)) for the tilted configuration of the decahedron around 790 nm for excitation over point 1 or 3. Due to increase in radiative damping, it is possible that mode C shows a redshift and appears at 840 nm, for excitation over point 4 or 5, as these corner points touches with the substrate. So we can say mode C might correspond to a dipolar charge oscillation from point 5 to 1 or point 4 to 3 (as shown in Figure 4.10 (b)). As a result of this we found maximum photon emission corresponding to mode C at 750 nm (experimental) from point 1 rather than point 2 in our experimental CL image (Figure 4.2 (g)). But similar luminescence can't found from point 4 or 5 as most of the radiative emission going into Si substrate from these two corners. So we can say, mode C might be substrate induced dipolar peak. In the EELS studies on gold decahedron (side edge

length 65 nm) supported by a mica substrate Myroshnychenko et al. [43] clearly showed splitting and red shifting of the degenerate dipolar mode in contact with the substrate.

4.1.4 Conclusions

In summary, site specific CL spectroscopy and imaging in a high resolution SEM have been used to understand the local plasmonic response of an isolated tilted gold decahedron of side edge length 230 nm supported on a Si substrate. Finite-difference time-domain (FDTD) simulations have been performed to understand the modal distribution of different resonant modes and to explore the effect of substrate. The CL-SEM technique combined with FDTD simulations have helped us to identify two prominent LSP modes in the visible region along with a substrate induced LSPR mode in the near-infrared (750 nm) region. While the shorter wavelength (560 nm) mode has a mixture of in-plane quadrupolar and out-of-plane quadrupolar charge distribution pattern, the longer wavelength (655 nm) mode has the dipolar charge pattern in both the direction. That such mode mixing occurs at a critical side edge length 130 nm of gold decahedron has been demonstrated by systematic numerical simulation using FDTD. Also, in contrast to earlier e-beam based study on gold decahedron [43, 48], here we have found occurrence of multiple resonance peak for e-beam excitation over different corner points, which is related to the phase retardation of electromagnetic signal with larger particle size used in this present study. In addition to the substrate induced new LSP mode, observation of mode mixing with a kind of charge distribution pattern not reported so far for a decahedral gold nanoparticle

supported on Si substrate of the present work shed new light on the area of metal nanoplasmonics.

PART II

4.2 Probing plasmonic properties of individual gold nano-octahedron

4.2.1 Introduction

Octahedral shape NPs have attracted significant research interest due to their exceptional geometric shape with several sharp corners and edges which can sustain large EM field (hot spots) that is favorable for various plasmonic applications [99, 100]. However, high spatial resolution imaging of plasmonic modes as well as effect of substrate for the case of Au octahedron at the single particle level has never been experimentally investigated. In the present work, we present a combined experimental and theoretical CL study of the plasmonic properties of individual Au octahedron of edge length 170 nm dispersed on a silicon (Si) substrate. We also present spatially resolved images of the radiating LSPR mode supported by the octahedron NP. Using FDTD simulations we also reveal the effect of substrate on the observed LSPR peak.

4.2.2 Methods

4.2.2.1 Experimental

In the present work, the Au octahedrons were synthesized by a seed mediated growth method, details of which have been described in Chapter 3. CL spectroscopy and imaging was performed in a ZEISS SUPRA 40 SEM extended with the Gatan MonoCL3 cathodoluminescence system. In the present study, data were recorded with an electron acceleration voltage of 30 kV and beam current of about 12 nA with a beam diameter of approximately ~ 5 nm. In the present study, all the spectra were taken

in the wavelength range of 500-700 nm and corrected from the substrate background. The spectral step size of 4 nm and a dwell time of 0.25s with a band pass of 11 nm were maintained while acquiring the CL spectrum in the present experiment.

4.2.2.2 FDTD simulations

To have a detailed understanding of the surface plasmon assisted photon emission from the Au nano-octahedron and to access the effect of substrate precisely we have also performed 3D FDTD simulations (from Lumerical solutions, Canada) details of which have been described in Chapter 2.

4.2.3 Results and discussions

Figure 4.11 (a) shows the SE image of the Au octahedron particle, where square base corner points and apex points of the octahedron are marked as 1-4 and 5, 6 respectively. In order to understand the orientation of the octahedron on Si substrate, we have tilted the sample stage at angle 30° . Stage tilted SEM image of the octahedron is shown in Figure 4.11 (c), which confirms that octahedron in the present case is supported on the silicon (Si) substrate with one of its faces (in this case alongside 2-3) touching to the substrate. Schematic diagram of such a supported octahedron is shown in Figure 4.11 (d). Figure 4.11 (b) shows the panchromatic CL image of the octahedron corresponding to the SE image of Figure 4.11 (a). From the pan CL image, we observe strongest photon emission only from the three points (1, 4 and 5) of the octahedron.

Figure 4.12 (a) shows experimentally obtained CL spectra taken from different beam injection positions (colored dots on the SEM images in the insets of Figure 4.12 (a)) of

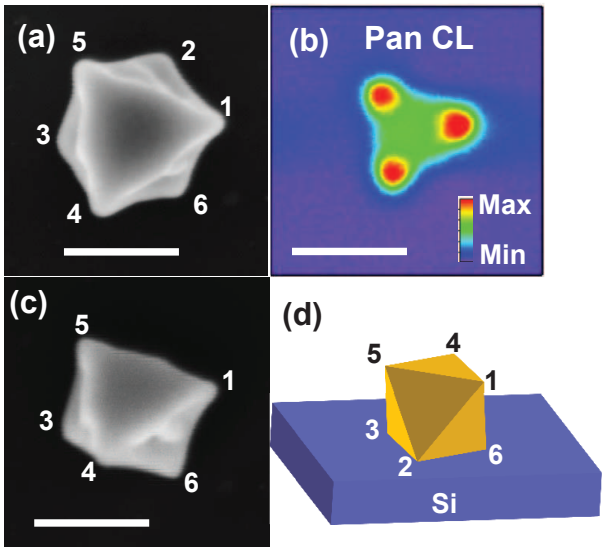

Figure 4.11: *(a) SEM image of an isolated single Au octahedron on Si (100) substrate. (b) Panchromatic CL image of the octahedron shown in part a. (c) Stage tilted SEM image of the octahedron, confirm that point 1, 4 and 5 are situated far from the substrate. Scale bar is 200 nm in all the case. (d) Geometric model of the octahedral NP on Si substrate.*

the octahedron. Experimental CL spectra of Figure 4.12 (a) depict that the spectral peak intensity and peak position is highly dependent on point of electron beam excitation. A single resonance peak is observed at wavelength 580 nm when the electron beam excites around the points 1, 4, and 5 of the octahedron. For e-beam impact near the points 2, 3 and 6, which are touching with the Si substrate, the radiated intensity is about 11 times smaller than the highest intensity obtained at point 5, which is also reflected from pan CL image. Our experimental observation is well supported by theoretically simulated CL spectra (Figure 4.12 (b)). Monochromatic CL images at 580 nm (resonance condition) and 680 nm (off resonance condition) are shown in Figure 4.12 (d) and (e) respectively. From these monochromatic CL images it is very much clear that strongest photon emission is only observed at the resonance

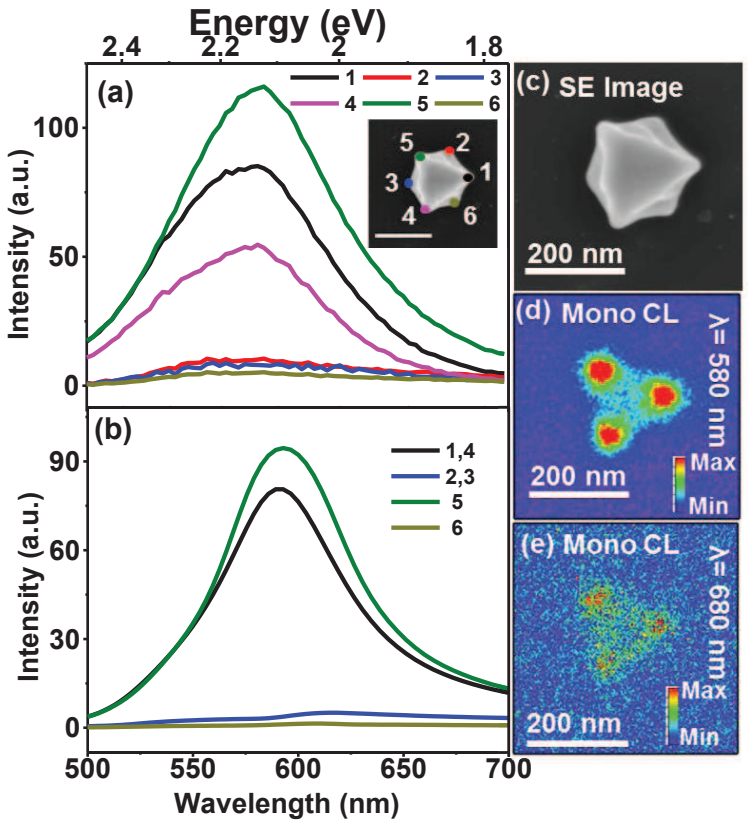

Figure 4.12: *(a) Experimental CL spectra taken at different beam injection positions (indicated on the marked inset SEM image) on a Au octahedral NP of side edge length 170 nm. (b) 3D-FDTD simulated CL spectra of the same morphology as shown in the inset of part a. (c) SE image of the octahedron and corresponding monochromatic CL images at different wavelength (d) at 580 nm (resonance condition) (e) 680 nm (off-resonance condition). The scale bar in all the images is 200 nm.*

condition, when LSP modes associated with NP are resonantly excited by the evanescent field associated with electron beam. Also it is interesting to note that strongest photon emission occurs from those points (marked as 1, 4 and 5) of the octahedron which are situated far from the substrate. Whereas almost no photon emission is observed from those points (marked as 2, 3 and 6) of the octahedron which are in touch with the substrate. The reason can be explained as follows: LSPR induced

radiation from the points which are in contact with the substrate will tend to radiate mostly into the high index Si (n=4) substrate [101]. As a result of which a negligible amount of emitted photons will reach to the CL detector which is situated at upper hemisphere. So we cannot observe any luminescence from these points (marked as 2, 3 and 6) in our experimental CL images. Similar observation is also reported for the case of Au decahedron particle in our previous study [48, 49].

4.2.3.1 Substrate effect on LSPR spectra

When a substrate is present beneath a NP, it's plasmonic properties alter a lot compare to the free standing one because of substrate induced inhomogeneous EM field experienced by the particle . At this point it is interesting to note what significant changes arise in the plasmonic properties of Au octahedron in presence of dielectric substrate compare to the free standing one. In Figure 4.13 (b), we have shown FDTD simulated CL spectra of an individual Au octahedron of side edge length 170 nm on Si substrate for different particle substrate gap variation keeping the e-beam excitation on point 1. Schematic diagram of this configuration is shown in Figure 4.13 (a). In absence of substrate, i.e. when the distance between particle and substrate is infinity, two resonant peaks appear at 570 nm and 642 nm respectively in the simulated CL spectra. Now as the octahedron approaches towards the substrate higher wavelength peak (642 nm) gradually redshifts, weakens and ultimately disappears when it touches the Si substrate. Whereas the lower wavelength peak redshifts very slightly with decreasing particle substrate separation and ultimately appears as 580 nm when the octahedron touches the Si substrate. The higher wavelength peak observed at

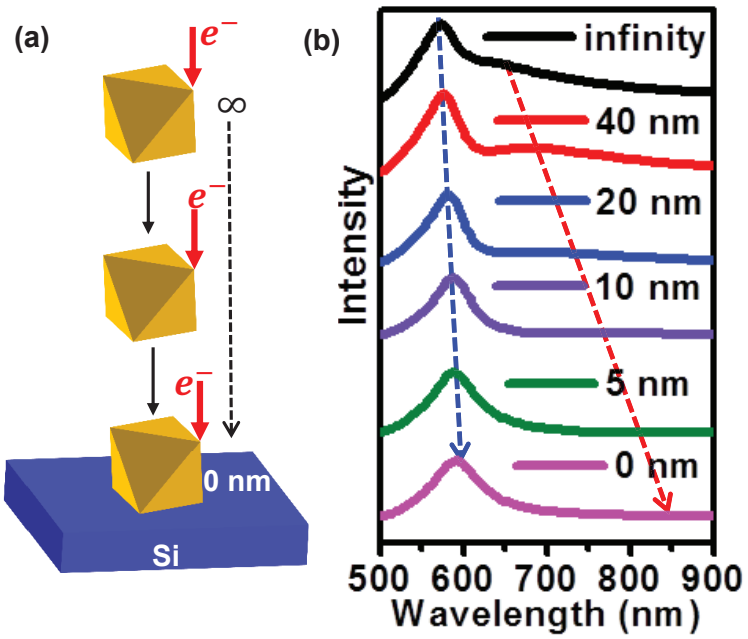

Figure 4.13: *(a) Schematic diagram of particle to substrate gap variation during FDTD simulation. (b) FDTD simulated CL spectra of an individual Au octahedron of side edge length 170 nm on Si substrate for different particle substrate gap variation as shown in part (a).*

642 nm in absence of substrate is dipolar resonance peak which gradually redshifts, weakens with decreasing particle separation and can't observed in the present experimental configuration i.e. when the octahedron touches the Si substrate. However the single resonance peak observed at 580 nm in the actual experimental situation is thought to be originated from higher order mode. In order to understand the specific origin of the observed resonance peak, we are trying to calculate the related near electric field vector plots using FDTD simulations. For this purpose, we have used 2D power monitors. However, these power monitors can be oriented either vertically or horizontally, i.e., in mutually orthogonal positions and no options exist for inclined positions. However, in the present scenario (i.e. in the tilted configuration of the

octahedron), it is very much difficult to understand the field distribution of the tilted octahedron using non-tilted 2D power monitor only. So exact origin of the observed mode for the case of tilted octachedron, is not possible at the moment. Further numerical analysis is needed in order to confirm the exact origin of the observed mode which is underway.

4.2.4 Conclusion

In summary, we have examined the local plasmonic response of an isolated tilted gold octahedron of side edge length 170 nm on a Si substrate using CL spectroscopy and imaging technique. We have also shown spatially resolved images of the radiating LSPR mode supported by the octahedron NP. Our experiment demonstrates that for the case of octahedron particle stronger photon emission is observed in the visible region from those corners and tip of the octahedron which are situated far from the substrate. FDTD simulations have been performed to explore the effect of substrate and to understand the origin of the experimentally observed peak. The experimental methodology and numerical analysis presented would enrich the understanding of light matter interaction at nanometer scale and may help to improve the design of new plasmonic devices.

Chapter 5

Efficient excitation of higher order modes in the plasmonic response of individual concave gold nanocubes

CL spectroscopy and imaging of plasmon modes have been performed on an isolated gold concave nanocubes of side edge length 170–230 nm.

5.1 Introduction

Recently, a new class of anisotropic MNPs with high index facets have emerged [6–8, 15, 62, 91, 102]. Among them, concave nanocube morphologies have drawn special attention due to their high chemical activity and large EM field enhancements compared to their simple cubic counterpart with flat surfaces [9]. These structures have a cube shape with well-defined sharp corners but with square pyramid-shaped depressions at the center of each of the six faces. It has been shown that by simply changing

the concaveness in different facets of the CNCs, one can tune the LSPR spectra from visible to NIR region [7]. Moreover, because of the very intense localized EM fields around their sharp edges and corners, CNC particles are particularly attractive for SERS and sensing applications [6–8, 62], and photovoltaic [15].

Recently, substrate-mediated plasmonic hybridization of simple Ag nanocubes with edge lengths varying from few to several hundred nanometers have been reported [13, 36–39, 58–60]. Moreover, due to the smaller size of these MNPs around the quasistatic limit, the resulting hybridized plasmon modes are in general a superposition of dipolar and quadrupolar modes. However, the larger the nanoparticle, the more it is capable of sustaining higher order modes. Investigation and identification of higher order surface plasmon modes are important from fundamental understanding and application point of view [55, 56]. Moreover, due to the deviation from ideal planar / flat surfaces of simple nanocubes, the effect of the MNP-substrate contact area on the substrate-mediated hybridized plasmon modes for concave cubic shaped MNPs is not yet fully addressed in the published works [62]. Here, we explore the localized surface plasmon modes of the Au CNCs with relatively larger size than previously studied nanocubes [13, 36–39, 58–60, 62]. Using CL-SEM spectroscopy and imaging and employing FDTD numerical simulations, we study of the plasmonic properties of individual gold CNCs with edge length of 170, 190, and 225 nm dispersed on a Si substrate. Direct comparison of the CL and calculated spectra using FDTD numerical simulation reveals that the substrate-induced splitting of a mode generates two hybridized mode, namely, corner octupolar and corner quadrupolar plasmon in addition to a quadrupolar edge mode. The spatial variation of the intensity distribution

of luminescence shows not only a strong localization of the radiative modes at the corner points but also its extension along the edges of the top surface. We show that while the corner modes are always present, the edge mode appears to be stronger with increased particle size and is associated with large EM field enhancement at the Au CNC's top surface-vacuum interface.

5.2 Methods

5.2.1 Experimental

Au CNCs were synthesized by a seed mediated growth method following a previous protocol [8, 91], the details of which have been described in Chapter 3. CL spectroscopy was performed in a ZEISS SUPRA 40 SEM extended with the Gatan MonoCL3 cathodoluminescence system. The details of CL-SEM system have already described in Chapter 3. In the present study, all the spectra were taken in the wavelength range of 500-900 nm and corrected from the substrate background. The complete spectra are taken in two different wavelength ranges, 500-800 nm and 800-900 nm and then merged after proper normalization. All the measurements were performed at an electron accelerating voltage of 30 keV (beam current $\sim$ 12 nA) with a beam diameter of approximately 5 nm. The spectral step size of 4 nm and a dwell time of 0.25 s with a band pass of 11 nm were maintained while acquiring the CL spectrum in the present experiment.

5.2.2 FDTD simulations

5.2.2.1 Electron excitation

In order to understand surface plasmon-assisted photon emission from Au CNC and to explore the effect of substrate on the Au CNC precisely, we have performed 3D FDTD simulations (from Lumerical FDTD Solutions, Canada) details of which has been shown in Chapter 2. To describe the wavelength dependent dielectric permittivity of gold we use experimentally tabulated data from CRC Handbook of chemistry and physics [88]. The Si substrate is taken as semi-infinite (*i.e.*, extended through the PMLs) with a constant refractive index n=4 [48]. In all the simulated spectra presented here, the indentation angle of the CNC is taken as 150° unless otherwise specified.

5.2.2.2 Optical excitation

For better understanding of the optical properties of CNC in vacuum we have also performed optical FDTD simulations. We use a total-field scattered-field (TFSF) source to calculate the absorption and scattering by CNC. Absorption and scattering cross-sections (σ_{abs} and σ_{scat}, respectively) are computed by monitoring the net power inflow in the total-field region near the particle and net power outflow in the scattered-field region, respectively. The extinction cross-section is given by σ_{ext}=σ_{abs}+σ_{scat}. The CNCs are considered to be in a vacuum environment with a refractive index n=1.

5.3 Results and discussion

5.3.1 Structural and compositional analysis:

The present synthesis produces a mixture of nanostars and CNCs of different sizes dispersed throughout the whole drop casted region. Among the randomly distributed Au nanoparticles, an isolated single Au CNC (SEM image, Figure 5.1 (a)) was identified for CL measurements. The geometry of an ideal CNC is characterized by 24 equivalent indented facets whose Miller indices are determined by the degree of indentation (schematics, Figure 5.1 (c)). The tetragonal indentation and the boundaries between adjacent indented facets of the present as-synthesized Au CNC particles are clearly visible when the SEM image was recorded by tilting the sample mounting stage (Figure 5.1 (b)). The TEM employed here to obtain the crystallographic information also provides additional morphological information on the as-synthesized Au CNC particle (Figure 5.1 (d-f)). The signature of concave facets of the present nanocube is clearly discernible in the dark-field as well as in bright-field TEM images of an isolated particle. The Au CNC particle appeared to exhibit darker contrast in the interior regions compared to the edge regions in the bright-field TEM image (Figure 5.1 (e)). The degree of indentation or concaveness is measured from the TEM image of Figure 5.1 (d). The average measured indentation angle (dihedral angle between indented facets) is $\sim 150^{\circ}$ which is very close to the indentation angle 148° of the Au CNCs enclosed by {720} facets synthesized by Mirkin and co-workers [62, 91], thus indicating that most of our Au CNCs are presumably enclosed by 24 high-index {720} facets. In Figure 5.1 (f), we show the selected area electron diffraction (SAED)

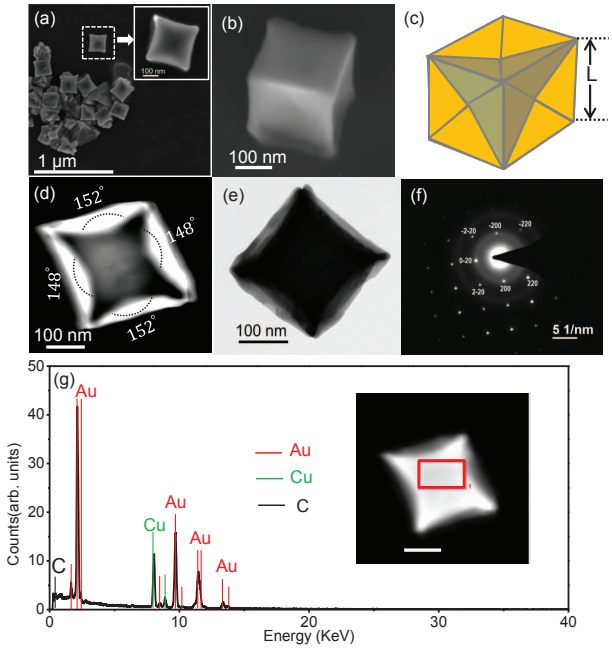

Figure 5.1: *(a) SEM image showing the aggregation of CNCs along with the mixture of nanostars. Among them an isolated single Au CNC is taken for CL measurement (inset). (b) Stage-tilted SEM image of the CNC. (c) Schematics of the model geometry of CNC of edge length L. (d) Dark-field TEM image of one individual CNC clearly showing the concave facets. (e) Bright-field TEM image of an isolated CNC and (f) corresponding selected area electron diffraction (SAED) pattern. The electron beam is projected along the [001] zone axis. (g) EDX spectrum for the CNC (area chosen is shown in the inset).*

pattern from the isolated Au CNC particle shown in Figure 5.1 (e), which confirms its single crystalline fcc structure. Furthermore, the presence of strong Au signal in the energy dispersive X-ray (EDX) spectrum (cf. Figure 5.1 (g)) obtained within the TEM from such as-fabricated sample confirms the compositional purity of Au CNC particles. The C and Cu signals in the EDX spectra originated from the carbon-coated Cu-grid used during the TEM analysis.

5.3.2 CL spectroscopy and imaging

Here, we have performed site specific CL spectroscopy and imaging over isolated single Au CNC particles of varying sizes with the edge length, L, ranging from 170 to 225 nm deposited on Si substrate. Figure 5.2 (a) shows experimentally obtained CL spectra from the L = 170 nm CNC, taken at different beam impact positions (colored dots on the SEM images in the inset of Figure 5.2 (a)). The acquired CL spectra reveal three major LSPRs, observed at around 560 nm (fwhm $\sim$ 80 nm), 620 nm (fwhm $\sim$ 65 nm), and 680 nm (fwhm $\sim$ 120 nm), respectively, when the e-beam probes the corners of the CNC (marked as 1-4). The panchromatic image of the particle shown in the inset of Figure 5.2 (a) gives an intuitive visualization of the plasmon resonances at play in the present CNC structure. However, they do not provide wavelength specific information that would help us identify the specific plasmon modes giving rise to the radiative response. The wavelength selected CL imaging will be discussed in the later part of this section. The FDTD calculated spectra (Figure 5.2 (b)) of the same CNC (L=170 nm) also confirm the three plasmon resonances with the peaks located at around 564 nm (mode E), 600 nm (mode C_1), and 700 nm (mode C_2), respectively, in excellent agreement with the experimental spectra. When exciting at the center of the CNC (point 5), a very weak CL response is observed in both experimental and calculated spectra with no significant LSPR features. As the CNC possesses a four-fold rotational symmetry, all the four corners should be equivalent and identical spectra should be measured for excitation over the four corners as shown in Figure 5.2 (b). However, in the experimental spectra (Figure 5.2 (a)), the peak position and relative peak intensity of the different modes vary slightly from corner to corner.

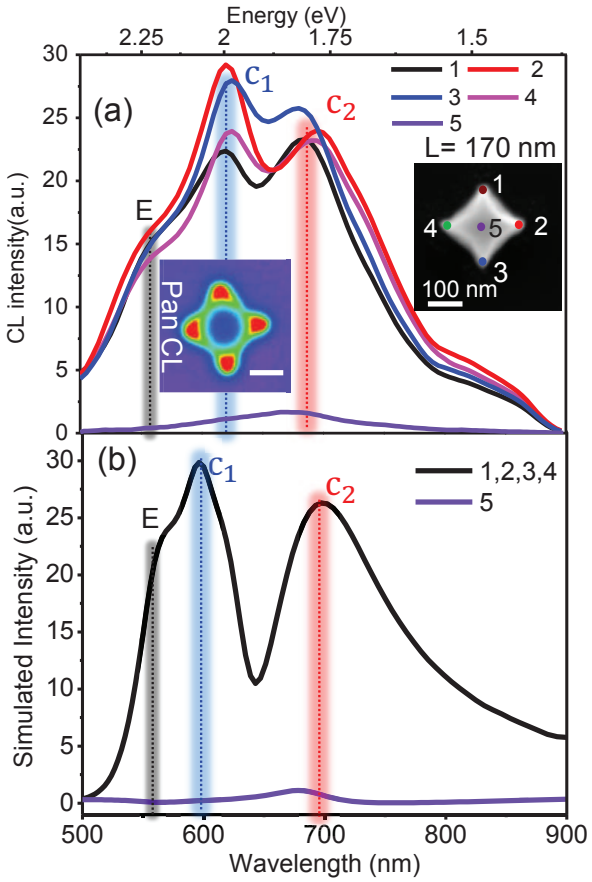

Figure 5.2: *(a) Experimental CL spectra taken at different beam impact positions (indicated on the marked SEM image, inset) on a Au CNC of side edge length L=170 nm. The panchromatic CL image is shown as an inset. (b) FDTD-calculated CL spectra of the same CNC as indicated in panel a.*

These spectral differences are most certainly attributed to the slight differences in the morphological features such as the curvature of the corners or small drift of the specimen during spectral data acquisition. Alteration of the position and intensity of the associated LSPR modes by the local change of the nanocube morphology has also been confirmed by Mazzucco *et al.* [36]. The presence of three LSP modes is also confirmed for two other large Au CNC particles. Experimental (red) CL spectra along with calculated (black) spectra for Au CNC of L= 190 and 225 nm are shown

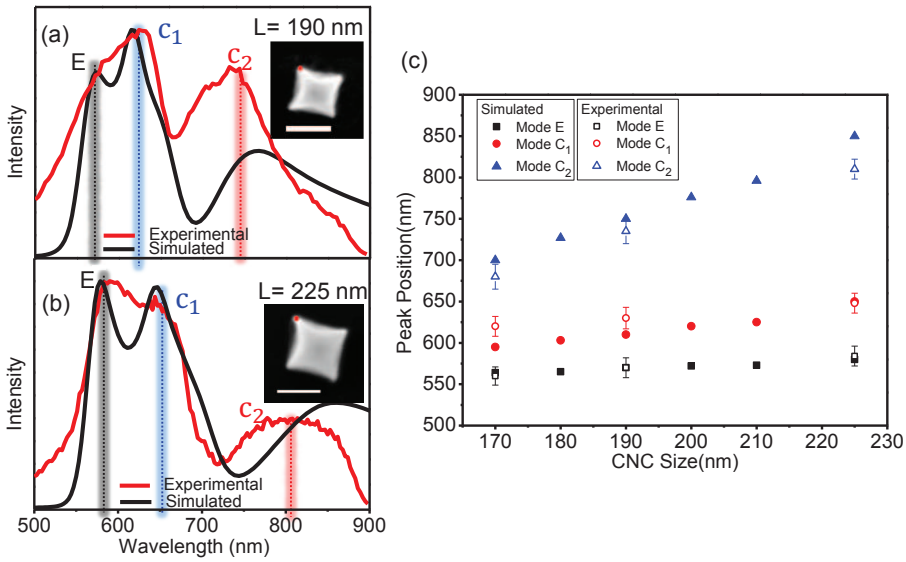

Figure 5.3: *(a-b) Experimental (red) and calculated (black) CL spectra for Au CNC of side edge length L=190 and 225 nm, respectively. Beam impact position is indicated by the colored dot on the inset SEM image. Scale bar is 200 nm for the inset SEM image. (c) Combined experimental and calculated evolution of the three LSP modes with the CNC size.*

in Figure 5.3 (a,b). The experimentally obtained CL data for the CNCs are highly reproducible. The reproducibility of our results has been checked by more measurements as shown in Figure 5.4.

Interestingly, the formation a large spectral dip observed between C_1 and C_2 (Figure 5.3 (a,b)) results from a stronger substrate-CNC interaction. The influence of dielectric substrate on plasmon resonance of a nearby nanoparticle can be described qualitatively using an image charge approach, explaining the screening effect, as shown by Nordlander, Halas and co-workers [61, 73]. In this framework, the magnitude of these induced surface charges directly depends on the dielectric permittivity of the substrate ϵ_s, as $(\epsilon_s$ -1$)/(\epsilon_s$ +1). The presence of such dip is also clearly confirmed in the calculated CL spectra (Figures 5.2 (b) and 5.3 (a,b)) as well with the depth

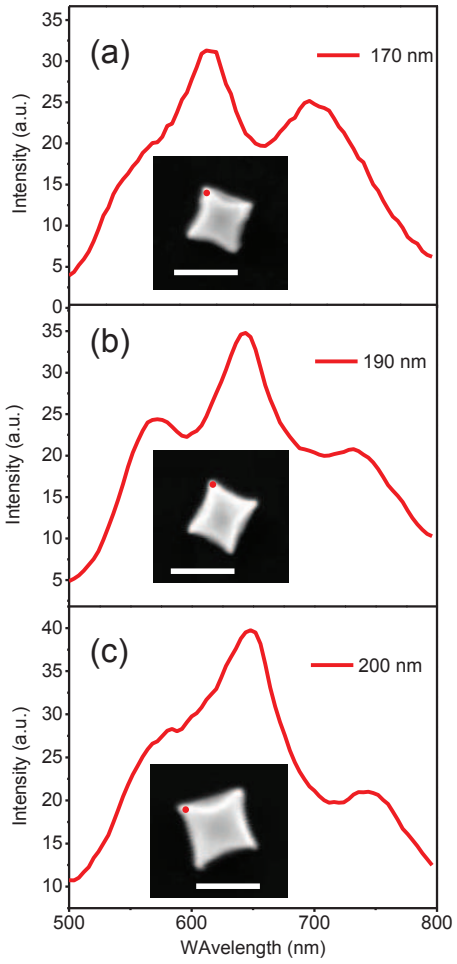

Figure 5.4: *Experimental CL spectra taken at corner excitations on Au CNCs of side edge length (a) 170 nm, (b) 190 nm, and (c) 200 nm. Scale bar is 200 nm in all the case.*

and location of the dip being slightly larger in the calculated spectra. Figure 5.3 (c) shows the spectral evolution (both experimental and calculated) of all these modes as a function of the CNC particle size. Calculated CL spectra for three other particles (L=180, 200, and 210 nm) are shown in Figure 5.5. It is interesting to note that the C_2 mode, which appears at 680 (fwhm $\sim$ 140 nm) and 700 nm in the experimental and calculated spectra, respectively, for the CNC L=170 nm, dramatically red-shifts

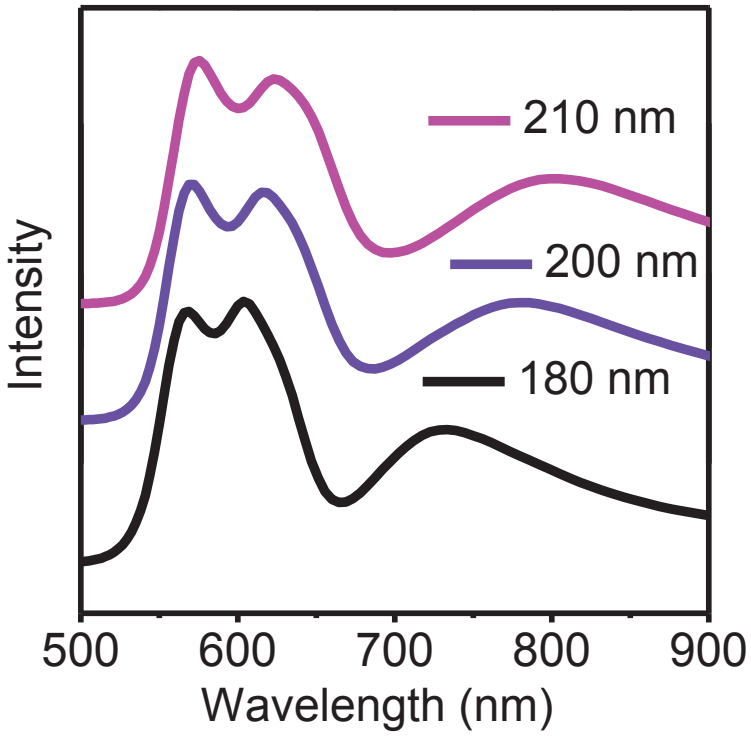

Figure 5.5: *Calculated CL spectra taken at corner excitations on Au CNCs of side edge length (a) 180 nm, (b) 200 nm, and (c) 210 nm.*

and broadens with increasing particle size and ultimately appears at 810 nm (fwhm $\sim$ 230 nm) when CNC edge length becomes 225 nm (850 nm in the calculated spectrum). From Figure 5.3 (c), it is noted that with an increase of edge length of about 55 nm (from L=170 to 225 nm) the mode C_2 red-shifts by about 120 nm whereas, the modes C_1 and E red-shift by about 55 and 20 nm, respectively. With increasing particle size, due to the retardation effects, the observed red-shift (associated to the dynamic depolarization) and broadening (associated to the radiative damping) of all the modes are consistent with the previous published works [57, 58].

To gain a deeper understanding on the spatial evolution of the specific plasmon mode giving rise to the radiative response, we performed wavelength selected CL imaging

(Figure 5.6) on the Au CNC particles. For each row of Figure 5.6, the first column represents the SEM image of the Au CNC particle of a particular size and the second, third, and fourth column represent CL maps of that particle corresponding to three resonant wavelengths associated to the LSP modes (E, C_1, and C_2) observed here.

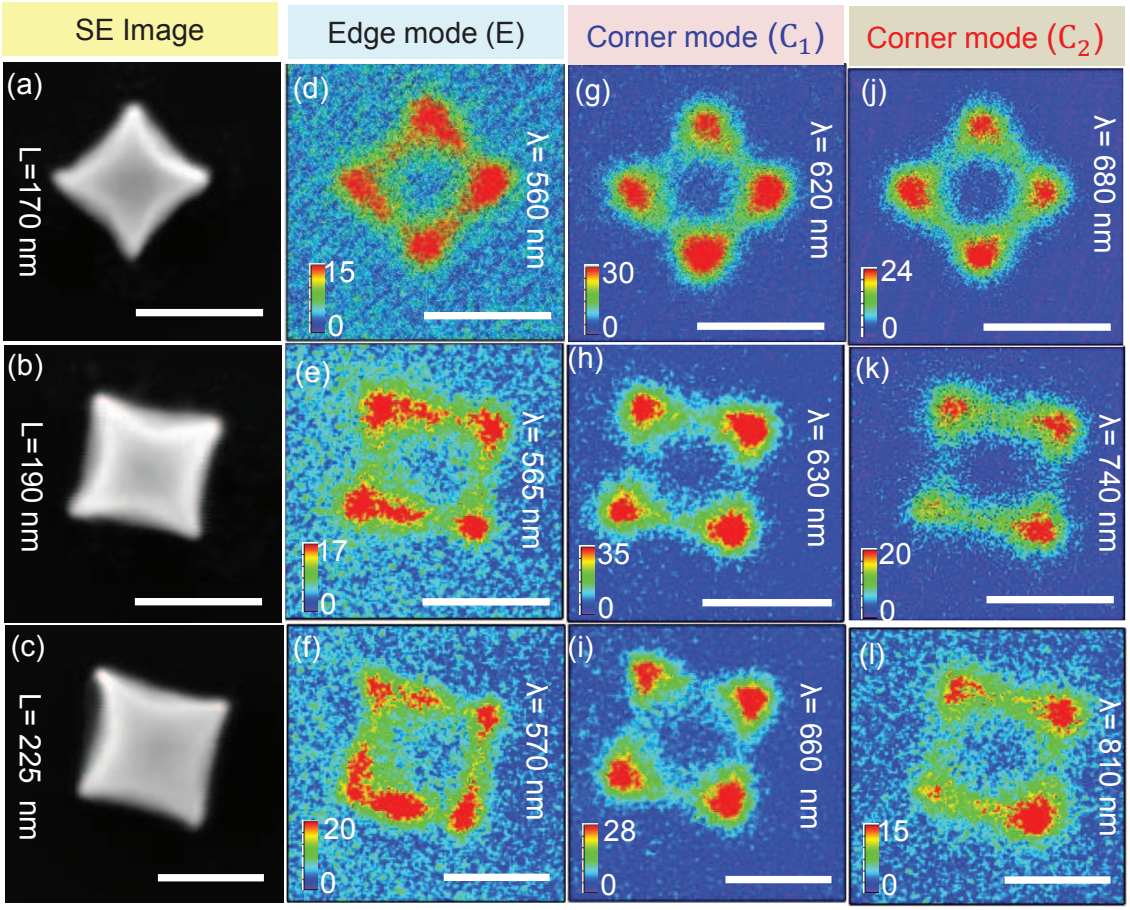

Figure 5.6: *Evolution of edge (E) and corner (C_1 and C_2) modes observed experimentally in monochromatic CL map as a function of the particle size. Scale bar is 200 nm in all the panels.*

From the monochromatic CL images, a change in spatial distribution of the luminescence intensity at different resonant wavelengths is clearly observed over a length scale much smaller than the wavelength of the emitted light. The monochromatic CL

image of mode E at 560 nm (Figure 5.6 (d)) for the Au CNC L=170 nm, shows that the photon emission is not concentrated along the corner only but is rather towards the edge of the CNC. As the edge length of the CNC increases (Figure 5.6 (e,f)), the spatial distribution of mode E gradually becomes stronger along the edges, indicating an edge quadrupolar mode. Due to its quadrupolar nature, mode E is expected to be nonradiative (*i.e.* dark). However, due to the retardation effects and due to the substrate-induced symmetry breaking, mode E become radiative and observable in CL [13, 103]. The monochromatic CL maps of mode C_1 and C_2 corresponding to CNCs of three different sizes show that the luminescence is prominent at the corners compared to that at the edges. The spatial distribution of mode C_1 is, however, more localized in corner than mode C_2 as reflected in the CL maps of larger CNCs of size 190 and 225 nm, respectively.

To further investigate the origin of the experimentally observed peaks and their corresponding modal distributions, we first discuss the case of isolated, free standing CNCs and focus on size effects using both optical and CL responses. Then using electrodynamic simulations we explore the substrate effect and compare the results to the experimentally obtained CL spectra (Figure 5.2 (a) and Figure 5.3 (a,b)). The right-most panel of Figure 5.7 (a-e) shows FDTD calculated optical (dashed lines) and CL spectra (solid lines) of Au CNCs in vacuum (n=1) for different edge legths (L= 60, 130, 170, 190, and 225 nm). The center panels (Figure 5.7 (f-i)) and Figure 5.7 (j-l)) depict near-field intensity maps at the peak wavelengths of the CL and optical spectra denoted by the color-coded arrows. For the optically excited Au CNC particle, the contribution of absorption in the extinction spectra is maximum with

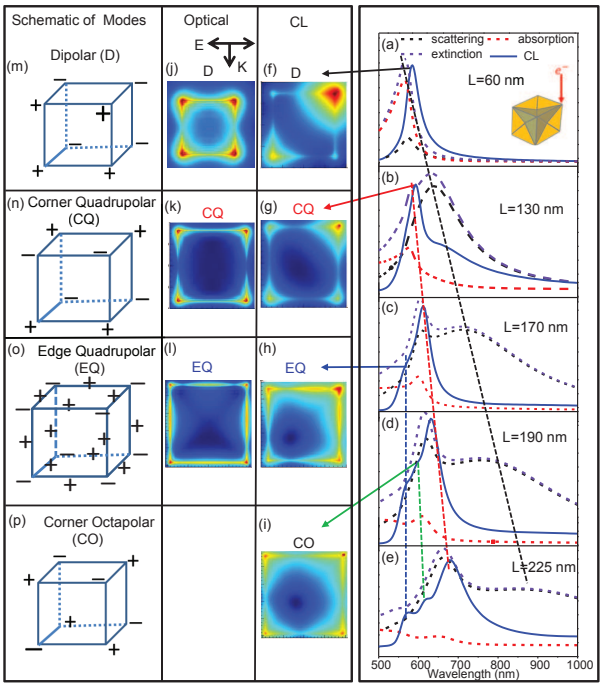

Figure 5.7: *FDTD calculated optical and CL responses for Au CNCs with various edge lengths (L= 60, 130, 170, 190, 225 nm) in vacuum. Right-most panels are the the optical extinction, scattering, and absorption (black, purple, and red dashed lines, respectively) and CL spectra (blue solid line) for each of the five CNCs (a-e). The CL spectra are obtained for an electron beam excitation at the corner of the CNC particle (inset of panel a). Schematic charge distribution of different modes and their corresponding near-field intensity map at top surface of the CNCs are plotted in the left-most(m-p) and center panels(f-l), respectively.*

the resonance peak at $\sim$ 570 nm for the smallest CNC with the edge length L=60 nm (Figure 5.7 (a)) and the absorption peak gradually decreases (Figure 5.7 (b-e)) with increasing particle size. For smaller nanoparticle the optical extinction spectra is dominated by the absorption, in agreement with previous published works [6, 7, 104]. The near-field intensity (Figure 5.7 (f,j) shown by black arrow) and charge pattern (top panel of Figure 5.8) for the optically excited particles confirm that the single resonance peak of the smallest particle corresponds to dipolar charge oscillation. The

dipolar peak is red-shifted to 636 nm in the extinction spectra when the particle size increases from 60 to 130 nm. Concurrently, a shoulder appears at 580 nm in the

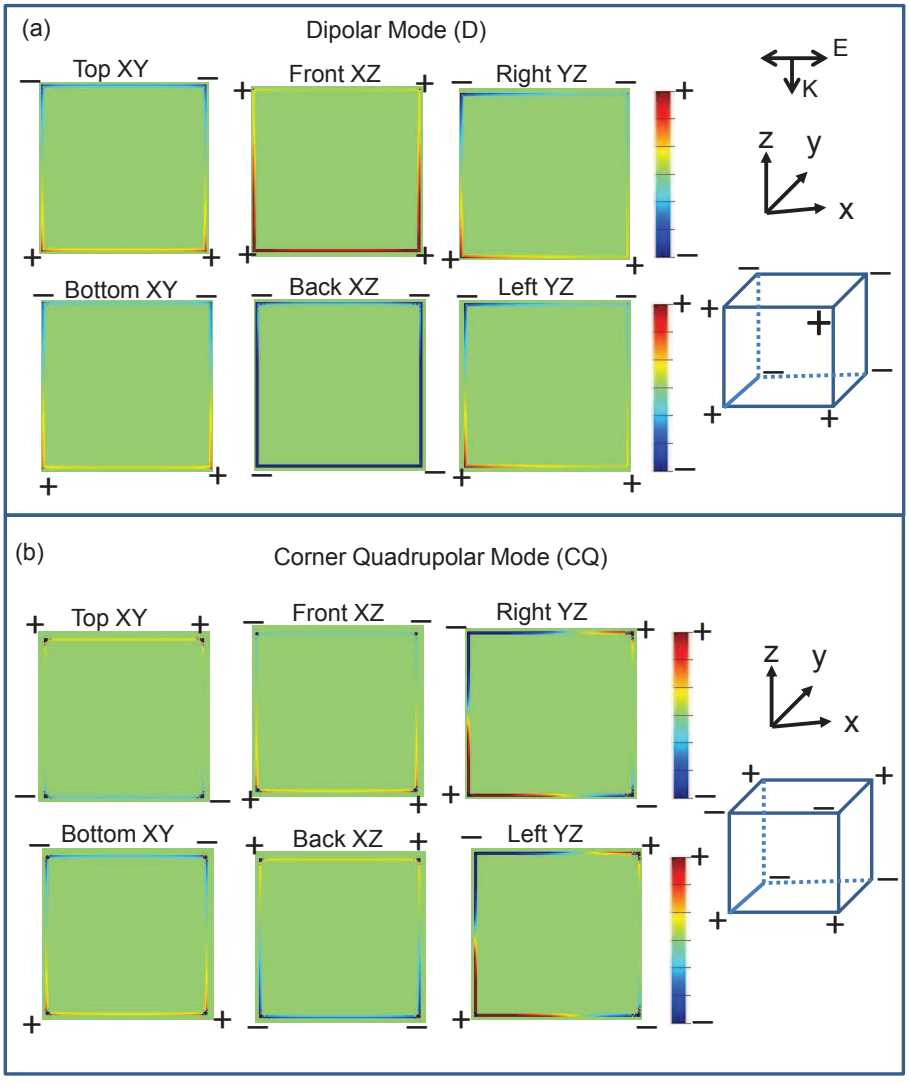

Figure 5.8: *Calculated surface charge distribution corresponding to (a) Dipolar mode and (b) Corner Quadrupolar mode.*

absorption spectrum, supporting the appearance of a nonradiative LSP mode. The near-field intensity (Figure5.7 (g, k), red arrow) and charge pattern (bottom panel of Figure 5.8) confirm that the shoulder at 580 nm corresponds to a corner quadrupolar

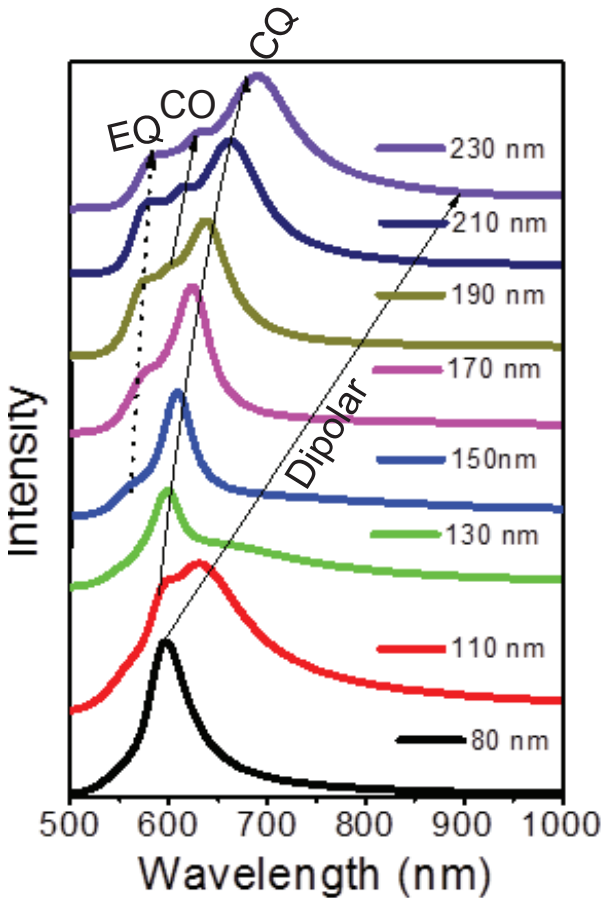

Figure 5.9: *Size dependence of the CL spectra calculated for CNC in absence of substrate showing dipolar mode vanishes for CNC larger than 130 nm and that higher order modes appear with increasing particle size.*

(CQ) charge oscillation. The optically excited dipolar mode is degenerate in energy with the CQ mode for small particle size. With increasing paticle size the degeneracy is lifted and the dipolar (D) mode gradually broadens and weakens (Figure 5.7 (c-e)). Similar observation is also reported by Kociak *et al.* for Ag nanocubes [36]. The calculated CL spectra (Figure 5.7 (a), solid line) for the smallest CNC particle also show dipolar mode at around 580 nm, close to the optical extinction peak. In contrast to optical scattering spectra we observed that electron beam preferentially

interacts with dipolar modes in free space for small particle size. However, with increasing particle size it cannot excite the dipolar mode efficiently. The disappearance of dipolar mode in electron-based CL spectroscopy with increasing particle size is shown in Figure 5.9. This is consistent with the previous observation by Li *et al.* [35] who showed that, in the case of EELS, the electron beam preferentially interacts with low order modes, *i.e.,* dipolar mode, for small size truncated Ag sphere in free space. The calculated CL spectra also confirm the appearance of CQ mode at 590 nm similar to the optical excitation for particle of size L=130 nm (Figure 5.7 (b)). The calculated CL spectra for the particle of size L=170 nm (Figure 5.7 (c), solid line) shows the presence of CQ mode at 610 nm as well as an edge quadrupolar (EQ) mode at 560 nm as confirmed from the intensity maximum along the edge in the field intensity map (Figure 5.7 (h,l), blue arrow). The modes CQ and EQ red-shifts with increasing particle size. For particles larger than 170 nm, one can see the appearance of a new LSP mode in the CL spectra (Figure 5.7 (d, e), solid line) between the EQ and CQ modes. This new peak becomes prominent at around 620 nm (Figure 5e) for the largest particle (L= 225 nm). The LSPR peak observed at 620 nm in the CL spectra can be attributed to a corner octupolar (CO) mode, exhibiting a field intensity maximum along all the corners of the CNC (Figure 5.7 (i), green arrow). However, for the largest particle analyzed here, we do not observe the CO mode in the optical spectra. However, we do see a prominent CQ mode and a weak EQ mode along with a broad dipolar mode. The absence of higher order octupolar mode and along with the weak appearance of EQ mode in optical excitation is due to the fact that light can couple to low frequency plasmon eigen modes more effectively than

that at high frequency (or low wavelength) due to larger momentum mismatch.

It is worth noting, whether the particle is excited optically or electron-beam driven, the resulting D, CQ, and CO modes show a near-field intensity distributions (Figure 5.7 (f,g,i-k)) with an extremum at each of the eight corner of the CNC with the spatial extension of the intensity of higher order modes (CQ and CO) being much sharper than the D mode. One can also have a heuristic picture of the three modes in their relative sign or phase of the charge density at each corner of the CNC (Figure 5.7 (m, n, p)). The D mode exhibits the well-known dipolar charge distribution pattern where positive and negative charges are distributed on opposite sides of the particle. For CQ mode, the surface charges are alternating from one edge to the other around an axis passing through the center of a face, while for the CQ mode, the charge density is alternating in each corner of the CNC.

5.3.3 Substrate effect

So far, we have discussed the modal distributions of the Au CNC particle in the absence of substrate. In our actual experimental study the CNC particle is in contact with a substrate (Si) with high dielectric constant. However, the surface contact area between the CNC and the substrate is significantly smaller than that of a perfectly flat nanocube. Therefore, it is interesting to note what significant changes arise in the plasmonic response of Au CNC located on the Si substrate. When the e-beam probe passes along the corner edge of the CNC (about 1 nm from the cube edge), it excites both the upper and the lower corner simultaneously due to the interaction of the evanescent field as shown in the schematic Figure 5.10 (a). While the upper

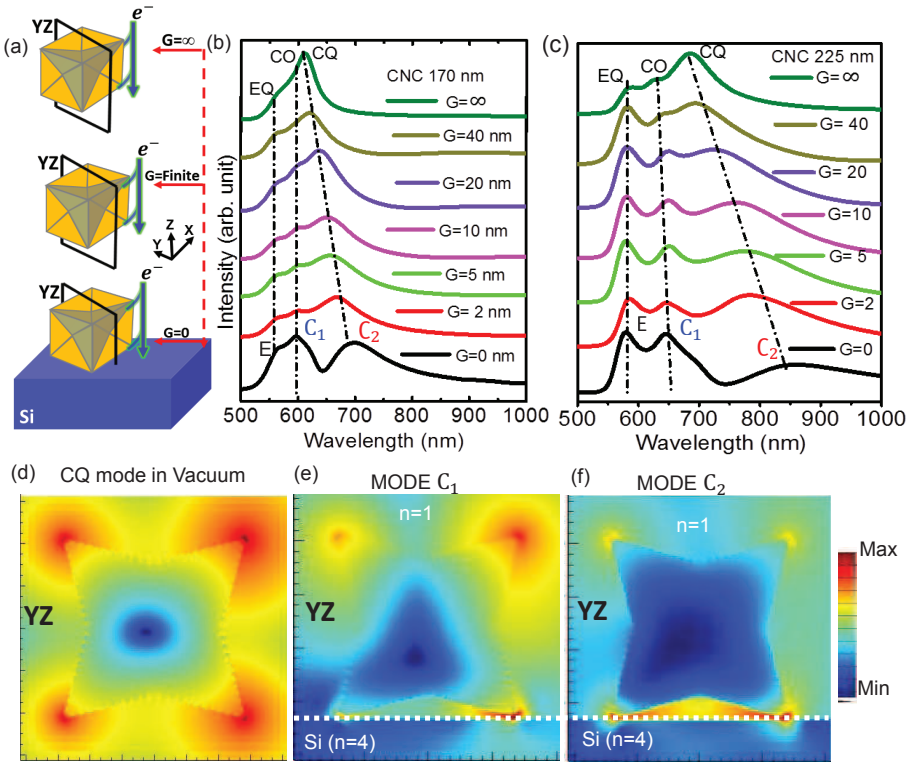

Figure 5.10: *(a) Schematic diagram of particle to substrate gap (G) variation. FDTD calculated CL spectra of an individual Au CNC of edge length (b) 170 nm (c) 225 nm on silicon substrate for different particle-substrate gaps.(d-f) Scattered electric field intensity distribution in YZ plane (X=0) as shown by black rectangle passing through the center of Figure 6a of CNC. The white dashed line indicates the upper surface of the substrate for mode C_1 and C_2.*

corners experience a surrounding medium with a low refractive index (n=1, vacuum), the lower corners experience a much larger refractive index medium (n=4, silicon). Figure 5.10 (b,c) shows the changes in the calculated CL spectra with decreasing nanoparticle-substrate (Si) separation (G) for two Au CNC particles with edge lengths 170 and 225 nm, respectively. For the L=170 nm CNC, in absence of substrate (G=∞), two resonant peaks associated to the EQ and CQ appear at 560 and 610 nm, respectively. As the CNC approaches towards the substrate, the EQ mode (560

nm) remains almost at the same position, whereas the CQ mode gradually red-shifts and ultimately splits into two peaks, a red-shifted peak at 700 nm and a slightly blue-shifted peak at around 600 nm when the particle touches the Si substrate. For the L=170 nm CNC particle, the CO mode which is not visible in absence of substrate (Figure 5.10 (b)) is nearly degenerate in energy with CQ mode. When the CNC particle approaches the substrate, the asymmetric dielectric environment leads to the strong interference between this CO and CQ mode to form hybridized modes. The hybridized mode C_2, originated from the CQ mode, gradually red-shifts and weakens with decreasing particle-substrate separation and ultimately appears at 680 nm (700 nm in the simulations) when the CNC touches the substrate (G=0 nm). On the other hand, the hybridized mode C_1, which originates from the CO mode, gains significant intensity with decreasing particle-substrate separation. However, C_1 does not shift much with decreasing gap and ultimately appears at 620 nm experimentally (600 nm in the simulations). Figure 5.10 (c) shows similar gap variation between the particle and the Si substrate for Au CNC of edge length 225 nm. When the CNC is far from the substrate (G=∞), a weak CO mode is already observed in the CL spectrum at 620 nm, as opposed to the L=170 nm case. As the CNC approaches towards the substrate, the CQ mode gradually red-shifts, weakens, and broadens with decreasing particle-substrate separation and ultimately appears as C_2 at 810 nm (850 nm in the simulations) when the particle touches the Si substrate (G=0 nm). On the other hand, the CO mode red-shifts slightly and gains significant intensity with decreasing particle-substrate separation. Finally, it appears as C_1 at 650 nm when the particle touches the substrate. The evolution of the calculated CL spectra as a function of

the particle-substrate separation (Figure 5.10 (b,c)) thus clearly shows a significant substrate-induced hybridization effect on the CNC LSP modes.

In the absence of substrate, (i.e., in vacuum) the CQ mode shows symmetric near-field pattern (Figure 5.10 (d)) where field maxima are located at the four corners of the cube's X=0 cross-sectional plane (YZ plane shown by black rectangle in the schematic of Figure 5.10 (a)). However, when the particle is in contact with the substrate, the symmetry is broken and the field intensity strongly localizes within the gap between the lower concave face and the substrate (Figure 5.10 (f)). This field localization, results from the particle-substrate hybridization, induced by the formation of image charges in the substrate. Interestingly, in spite of the proximity of the substrate, most of the field intensity of the C_2 mode is concentrated within this concave gap space. This is in contrast to the situation for an optically excited Ag simple nanocube of small dimension, where due to the planar particle-substrate interface, maximum fraction of the induced near-field intensity of the dipolar mode penetrated towards the substrate [13, 60]. On the other hand, the CO mode, in presence of the substrate, turns into hybridized mode C_1 and shows dominant field distribution at the particle-vacuum interface (Figure 5.10 (e)). Due to the confinement of the C_2 mode in the concave gap region, a small part of the radiated power is leaked to the surrounding vacuum environment. As a result, we can notice that the gradual red-shift and weakening of the CQ mode with decreasing particle-substrate separation, observed in the calculated CL spectra (Figure 5.10 (b,c)), is more pronounced for the larger CNC particles. Experimentally, we do not expect sufficient photon to reach to the CL detector, which is the reason why the C_2 mode only weakly appears even

with increasing particle (Figure 5.6 (j-l)). However, because the mode C_1 is associated with large field intensity at the particle-vacuum interface, it is not affected as significantly as mode C_2 at the small particle-substrate separation limit, thus giving stronger intensity in the calculated and experimental CL spectra as well in the mono CL maps (Figure 5.6 (g-i)).

Recently, a large number of studies have shown the occurrence of substrate-induced mode splitting for the case of Ag nanocubes through the formation of so called distal and proximal modes [13, 38, 39, 60]. In these works, the distal LSPR mode is the anti-bonding mode resulting from the hybridization of the bright dipolar and dark quadrupolar modes. It exhibits strong localized field on the cube's top surface (i.e., cube-vacuum interface), resulting in maximum field expansion into the surrounding environment. On the other hand, the proximal mode originates from the bonding combination of the dipolar and quadrupolar modes leading to maximum field intensity at the cube's bottom surface, mostly penetrating into the substrate. Here, our numerical study shows that the modes C_1 and C_2 behave as distal and proximal as reported in literature [13, 38, 39, 60]. Recent works on single Au/Pd octopods, [105, 106] which is quite similar to the concave cubic-symmetry nanostructures, also show substrate-induced mode splitting in the form of distal and proximal modes. Although the numerical simulations suggest that the mode C_2 is mostly confined to the gap space between the bottom face of CNC and the Si substrate, the experimental demonstration of the effect of gap mode in the form of spatially distributed photon map is only possible if the CL imaging / mapping be recorded in the tilting configuration of the sample stage as is done in the EELS experiments by the Ringe *et al.* [106]

for octopod nanoparticles and by Nicolleti *et al.* for simple nanocubes [38]. However, in the present case such measurement cannot be performed due to the tilting limitations of the sample stage used during the CL experiments. Moreover, unlike the distal and proximal modes of the silver cube of the previous studies [13, 38, 39, 60], which originate from the dipolar and quadrupolar modes, the present analogous C_1 and C_2 modes are of higher orders, originating from corner octupolar and corner quadrupolar mode respectively.

The FDTD-calculated spectral evolution with particle-substrate separation as depicted in Figure 5.10 (b,c) also reveals another interesting aspect. As the dip between hybridized C_1 and C_2 modes becomes deeper and broader with increasing particle size, an asymmetric line shape characteristic of a Fano resonance becomes more pronounced. This Fano-like line shape is also observed in the experimental CL spectra (Figure 5.2 (a) and Figure 5.3 (a,b)) and appears to be very sensitive to particle-substrate separation [13, 60, 77, 78]. In order to observe a CL-driven Fano resonance there must be an electron-induced radiative emission of energy carried to the far-field, meaning, plasmon modes that have a net dipole moment will be contributing to CL-driven Fano resonance. Hybridized LSP modes having a net dipole moment can broadcast electromagnetic energy into the far-field showing, in principle, asymmetric Fano line shapes to be observable in CL has been predicted theoretically quite recently [107]. Signatures of Fano interferences in CL should usually be expected in situations where there is a corresponding optically driven Fano resonance. However, there is no report up-to-date for Fano resonance of optically excited Au CNC particles of the sizes employed in the present work although Fano resonance has been reported

for optically excited Ag nanoparticle [13] with simple cube geometry of size less than 100 nm or Fano-dip in the cluster system [108]. Consequently, it remains difficult to say unambiguously if the dip observed in between the hybridized modes C_1 and C_2 in the present CL spectra results from Fano interference without further detail analysis.

Although nanostructures with concave faces are not common [109], they present

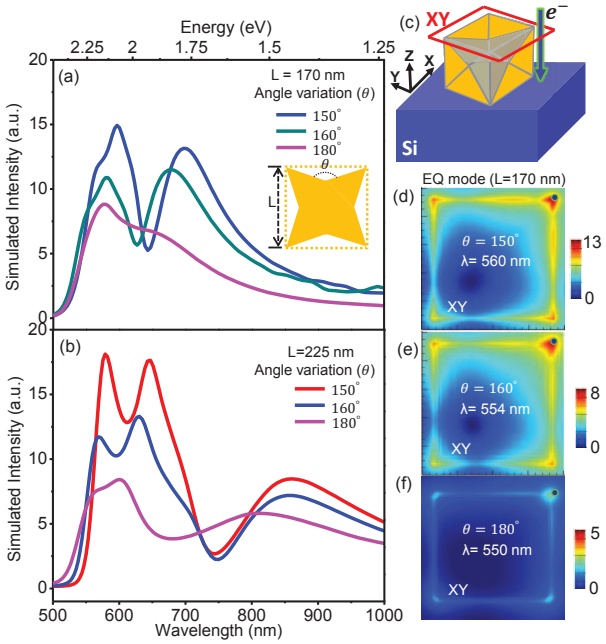

Figure 5.11: *Calculated CL spectra of Au CNC of side edge length (a) L=170 nm and (b) L=225 nm for varying indentation angle θ. With decreasing indentation angle one clearly observes a red-shift of different LSPR mode as well as increase in intensity. (c) Schematic diagram showing the plots of field intensity maps calculated on red rectangular XY plane of the top surface of the CNC for the electron beam trajectory as shown with blue arrow head. (d-f) Near-field intensity maps at the top surface of the CNC (L=170 nm) for varying indentation angle are shown in right panel. Dots at the upper right corner of each of the field maps (d-f) denote the point of electron beam impact.*

a great potential for multifunctional SERS-catalysis platforms as they exhibit high index facets and strong localized field enhancements. Therefore, it is interesting to

compare the plasmonic response of the Au CNC with that of cubes with flat surfaces and of dimensions similar to the CNC particles used in the present work. For this purpose, we have plotted in Figure 5.11 (a,b), the FDTD calculated CL spectra (for e-beam injection at one of the four corners) as a function of concaveness or indentation angle (θ) for two CNC particles with L= 170 and 225 nm. It is clear from Figure 5.11 (a,b) that the spectral peaks at high wavelengths for concave cubes are red-shifted and enhanced in intensity with respect to the simple cubes with flat surfaces (θ=180°). Figure 5.11 (d-f) show the near-field intensity maps at the top surface of the CNC (L=170 nm with varying θ) for the lower wavelength LSP mode. It is interesting to note that the lower wavelength mode, i.e., the edge quadrupolar mode, becomes prominent with increasing concaveness (decreasing indentation angle) as shown in Figure 5.11 (d-f). The plasmon resonance for the CNC is expected to be red-shifted with respect to simple cube with flat surfaces [102, 110].

5.4 Conclusions

In summary, we have addressed several new aspects in the plasmonic response of concave gold nanocube. First, the experimental CL spectral and spatial data analyzed with detail FDTD-based simulations show the existence of edge quadrupolar mode as well as hybridized corner quadrupolar and octupolar modes which have not been reported so far to the best of our knowledge for Au CNC particles. The higher order modes arise due to the phase retardation of electromagnetic signal with larger particle size. Our analysis also points out that the lower wavelength edge quadrupolar mode becomes prominent with increasing concaveness of the CNCs. Second, we

have shown that, for free standing concave nanocube, the octupolar mode cannot be excited using light beam whereas it can be excited via electron beam based CL as demonstrated by electrodynamics simulations. Finally, we have found a prominent dip in our experimental, supported by CL simulations, which is presumed to be a Fano-like interference resulting from the substrate-mediated hybridization between broad corner quadrupolar mode and narrow corner octupolar mode of the CNC particle. Our detailed analysis allow to point out that large Au CNC particles with high concaveness constitute strong candidates for multifunctional SERS-catalysis platforms as they exhibit strong localized electric fields for SERS and high index facets suitable for catalysis.

Chapter 6

Summary and outlook

In this chapter a brief, chapter wise summary of the thesis along with the scope for future study is outlined.

6.1 Summary

The study of plasmon assisted photon emission from single metal nanostructures is becoming extremely crucial due to its huge application in chemical and biological sensing [12, 111], drug delivery [28], cancer therapy [26, 27], solar energy harvesting [112, 113] and surface enhanced spectroscopy [5–11]. However for advancing different applications a solid knowledge of electromagnetic field distribution associated with nanoparticle SPs, with a sufficient degree of energy and spatial resolution, is of major importance. In this respect cathodoluminescence (CL) combined with scanning electron microscopy (SEM) gradually become an emerging tool to spectrally resolve and spatially image SPs on metallic nanostructures with truly nanometer spatial resolution. The present thesis reports mainly plasmon assisted photon emission from isolated gold NP of three different geometry (decahedron, octahedron and concave nanocube) using CL combined with finite-difference time-domain (FDTD) simulations with special emphasis on higher order modes and substrate effect. Investigation and identification of higher order modes and substrate effect are important from fundamental understanding as well as application point of view.

In Chapter 1, a broad overview about the importance of studying surface plasmon assisted photon emission from MNPs especially from Au NPs has been described. Also it has been discussed, why single particle spectroscopy and imaging with a nanometer-resolved energy and spatial resolution is essential to probe the optical properties of individual nano objects.

In Chapter 2, basic concepts of the origin of localized surface plasmons (LSPs), effect

of retardation, light scattering and absorption by MNPs, as well as effect of substrate on LSPR have been discussed. Furthermore the physics of probing LSPR, with nanometer scale spatial resolution, using CL in a SEM has also been described. The basic principle of FDTD numerical simulation and its application in CL based MNP plasmonics have also been discussed in this chapter.

In Chapter 3, the chemical synthesis protocols of anisotropic gold nanostructures of different morphology have been discussed. The detail technical description of the the CL-SEM set up that is used as a major characterization tool in this thesis has been presented in this chapter. The basics of transmission electron microscope (TEM), energy dispersive X-ray (EDX) have been also discussed in this chapter.

In Chapter 4, CL spectroscopy and imaging of plasmon modes on isolated polyhedral gold nanoparticles has been presented. Two types of geometries, namely, decahedron and octahedron have been studied. For decahedron NP of side edge length 230 nm, we show that site selective electron beam excitation in a SEM gives rise multiple resonance peaks in the CL spectra which is very much dependent on the position of the electron beam. In order to understand the modal distribution of different resonant modes and to explore the effect of substrate, FDTD simulations have also been performed. Apart from a substrate induced LSPR mode in the near-infrared (750 nm) region, FDTD numerical analysis also identifies two prominent LSP modes in the visible region. While the shorter wavelength (560 nm) mode has a mixture of in-plane quadrupolar and out-of-plane quadrupolar charge distribution pattern, the longer wavelength (655 nm) mode has the dipolar charge pattern in both the direction. We also analyse numerically to show the critical size of the side edge length of

the decahedron particle where mode mixing is initiated.

In case of individual octahedron of side edge length 170 nm a single resonant peak was obtained at around 580 nm in the CL spectra. Stronger photon emission has been observed in the visible region from those corners and tip of the octahedron which are situated far from the substrate. Using extensive FDTD simulation we have also shown that the observed radiative mode is higher order mode other than the dipolar mode and also discussed their dependency on the Si Substrate.

In Chapter 5 the plasmonic response of an individual Au concave nanocubes (CNCs) with edge length of 170, 190, and 225 nm has been discussed using CL-SEM spectroscopy and imaging technique. Three prominent LSPR peaks are observed in the substrate supported CL spectra of CNC which red shifts with increase in particle size. We observe that site-selective electron beam excitation of individual Au CNC particles gives rise to simultaneous excitation of edge and corner LSP modes. We also show that spatial variation of the radiative modes are strongly localized at the corners and extended along the edges of the top surface of the CNCs. Extensive FDTD numerical analysis reveals that the substrate-induced plasmon hybridization leads to the activation of corner octupolar and corner quadrupolar LSP modes, in agreement with the CL measurements. Remarkably, the strength of the hybridization is shown to depend on the CNC size. Furthermore, it has been shown that the edge quadrupolar mode becomes prominent with increasing concaveness, thus opening up a new way of engineering the LSP modes.

6.2 Outlook

Overall, the studies presented in this thesis demonstrate that, CL-SEM can be regarded as an ideal nanoscale probe, with which one can perform spectroscopy and imaging on nanometer sized objects. More interesting is the application of CL combined with FDTD to probe and visualize the plasmon modes of isolated MNPs of different geometry. We believe that the experimental methodology and numerical approach discussed in this thesis will give an alternating pathway to understand the near field-optical properties and substrate-induced hybridization of complex shaped metal nanoparticles which may have stronger implication in novel applications, such as in surface enhanced Raman scattering, catalysis, sensing, and imaging.

The thesis addresses several problems and in doing that it arises few unanswered questions still remain to address in future and will be of importance to nanophotonics community. For the case of decahedral NP, we have shown the dependence of mode mixing as a fuction of size parameter using FDTD simulation. Better understanding in this direction is expected by experimentally probing decahedron NPs of varying size. In case of CNC, we have found Fano-like dip in the experimental CL spectra and appears to be very sensitive to particle-substrate separation. However we were not able to conclude whether it is Fano interference or not, as there is no result available corresponding to the optically driven Fano resonance for these type of structure. However, probing the same CNC particle with light and electron beam simultaneously can give more insight into this direction. Another interesting finding of our study for the case of CNC, is the existence of gap mode between the bottom

surface of the CNC and the Si substrate which is well supported by the FDTD simulations. However, experimental demonstration of these gap mode can not be performed due to the restriction of tilting sample stage during CL experiments in our commercial CL-SEM machine. It will be interesting to experimentally demonstrate the effect of gap mode in the form of spatially distributed photon map which would lend support to potential practical applications of this feature. In this thesis I have described the substrate effect on LSPR using FDTD based numerical simulation. However, it will be interesting to verify it experimentally by placing the same nanoparticle on different substrate. Also, the coupling between two or more very closely lying metal nanostructures is a hot issue of plasmonics as it can lead to huge local electric field enhancement (hot spot) between the gap of the dimer compare to the single NP.

Bibliography

[1] S. A. Maier, *Plasmonics: Fundamentals and Applications* (Springer Science+ Business Media, 2007).

[2] F. J. García de Abajo, Rev. Mod. Phys. **82**, 209 (2010).

[3] W. L. Barnes, A. Dereux, and T. W. Ebbesen, Nature **424**, 824 (2003).

[4] R. Ritchie, Physical Review **106**, 874 (1957).

[5] L. Rodriguez-Lorenzo, R. A. Alvarez-Puebla, I. Pastoriza-Santos, S. Mazzucco, O. Stéphan, M. Kociak, L. M. Liz-Marzán, and F. J. Garcia de Abajo, J. Am. Chem. Soc. **131**, 4616 (2009).

[6] P. Matteini, M. de Angelis, L. Ulivi, S. Centi, and R. Pini, Nanoscale **7**, 3474 (2015).

[7] J. Romo-Herrera, A. González, L. Guerrini, F. Castiello, G. Alonso-Nuñez, O. Contreras, and R. Alvarez-Puebla, Nanoscale **8**, 7326 (2016).

[8] Q. Zhang, N. Large, and H. Wang, ACS Appl. Mater. Interfaces **6**, 17255 (2014).

[9] H. Jing, Q. Zhang, N. Large, C. Yu, D. A. Blom, P. Nordlander, and H. Wang, Nano Lett. **14**, 3674 (2014).

[10] B. Sharma, R. R. Frontiera, A.-I. Henry, E. Ringe, and R. P. Van Duyne, Mater. Today **15**, 16 (2012).

[11] P. Alonso-González, P. Albella, M. Schnell, J. Chen, F. Huth, A. García-Etxarri, F. Casanova, F. Golmar, L. Arzubiaga, L. Hueso, et al., Nat. Commun. **3**, 684 (2012).

[12] J. N. Anker, W. P. Hall, O. Lyandres, N. C. Shah, J. Zhao, and R. P. Van Duyne, Nat. Mater. **7**, 442 (2008).

[13] S. Zhang, K. Bao, N. J. Halas, H. Xu, and P. Nordlander, Nano Lett. **11**, 1657 (2011).

[14] P. Bharadwaj and L. Novotny, Opt. Express **15**, 14266 (2007).

[15] Y. Bai, T. Butburee, H. Yu, Z. Li, R. Amal, G. M. Lu, and L. Wang, J. Colloid Interface Sci. **449**, 246 (2015).

[16] N. S. King, M. W. Knight, N. Large, A. M. Goodman, P. Nordlander, and N. J. Halas, Nano Lett. **13**, 5997 (2013).

[17] H. A. Atwater and A. Polman, Nat. Mater. **9**, 205 (2010).

[18] W. Hou and S. B. Cronin, Adv. Funct. Mater. **23**, 1612 (2013).

[19] M. Righini, P. Ghenuche, S. Cherukulappurath, V. Myroshnychenko, F. J. García de Abajo, and R. Quidant, Nano Lett. **9**, 3387 (2009).

[20] M. L. Juan, M. Righini, and R. Quidant, Nat. Photonics **5**, 349 (2011).

[21] S. A. Maier, P. G. Kik, H. A. Atwater, S. Meltzer, E. Harel, B. E. Koel, and A. A. Requicha, Nat. Mater. **2**, 229 (2003).

[22] J. B. Lassiter, F. McGuire, J. J. Mock, C. Ciracì, R. T. Hill, B. J. Wiley, A. Chilkoti, and D. R. Smith, Nano Lett. **13**, 5866 (2013).

[23] A. Manjavacas and F. J. García de Abajo, Nano Lett. **9**, 1285 (2008).

[24] N. L. Rosi and C. A. Mirkin, Chem. Rev. **105**, 1547 (2005).

[25] E. C. Dreaden, A. M. Alkilany, X. Huang, C. J. Murphy, and M. A. El-Sayed, Chem. Soc. Rev. **41**, 2740 (2012).

[26] X. Huang, I. H. El-Sayed, W. Qian, and M. A. El-Sayed, J. Am. Chem. Soc. **128**, 2115 (2006).

[27] N. S. Abadeer and C. J. Murphy, J. Phys. Chem. C **120**, 4691 (2016).

[28] P. Ghosh, G. Han, M. De, C. K. Kim, and V. M. Rotello, Adv. Drug Delivery Rev. **60**, 1307 (2008).

[29] A. V. Zayats, Nature **495**, S7 (2013).

[30] M. I. Stockman, Opt. Express **19**, 22029 (2011).

[31] M. Sandtke and L. Kuipers, Nat. Photonics **1**, 573 (2007).

[32] R. M. Bakker, A. Boltasseva, Z. Liu, R. H. Pedersen, S. Gresillon, A. V. Kildishev, V. P. Drachev, and V. M. Shalaev, Opt. Express **15**, 13682 (2007).

[33] M. Rang, A. C. Jones, F. Zhou, Z.-Y. Li, B. J. Wiley, Y. Xia, and M. B. Raschke, Nano Lett. **8**, 3357 (2008).

[34] M. Kociak and O. Stéphan, Chem. Soc. Rev. **43**, 3865 (2014).

[35] G. Li, C. Cherqui, Y. Wu, N. W. Bigelow, P. D. Simmons, P. D. Rack, D. J. Masiello, and J. P. Camden, J. Phys. Chem. Lett. **6**, 2569 (2015).

[36] S. Mazzucco, N. Geuquet, J. Ye, O. Stéphan, W. Van Roy, P. Van Dorpe, L. Henrard, and M. Kociak, Nano Lett. **12**, 1288 (2012).

[37] V. Iberi, N. W. Bigelow, N. Mirsaleh-Kohan, S. Griffin, P. D. Simmons Jr, B. S. Guiton, D. J. Masiello, and J. P. Camden, J. Phys. Chem. C **118**, 10254 (2014).

[38] O. Nicoletti, F. de La Peña, R. K. Leary, D. J. Holland, C. Ducati, and P. A. Midgley, Nature **502**, 80 (2013).

[39] G. Li, C. Cherqui, N. W. Bigelow, G. Duscher, P. J. Straney, J. E. Millstone, D. J. Masiello, and J. P. Camden, Nano Lett. **15**, 3465 (2015).

[40] O. Nicoletti, M. Wubs, N. A. Mortensen, W. Sigle, P. A. Van Aken, and P. A. Midgley, Opt. Express **19**, 15371 (2011).

[41] N. Kawasaki, S. Meuret, R. Weil, H. Lourenço-Martins, O. Stephan, and M. Kociak, ACS Photonics **3**, 1654 (2016).

[42] R. Arenal, L. Henrard, L. Roiban, O. Ersen, J. Burgin, and M. Treguer-Delapierre, J. Phys. Chem. C **118**, 25643 (2014).

[43] V. Myroshnychenko, J. Nelayah, G. Adamo, N. Geuquet, J. Rodríguez-Fernández, I. Pastoriza-Santos, K. F. MacDonald, L. Henrard, L. M. Liz-Marzán, N. I. Zheludev, et al., Nano Lett. **12**, 4172 (2012).

[44] E. J. R. Vesseur, R. de Waele, M. Kuttge, and A. Polman, Nano Lett. **7**, 2843 (2007).

[45] P. Chaturvedi, K. H. Hsu, A. Kumar, K. H. Fung, J. C. Mabon, and N. X. Fang, ACS Nano **3**, 2965 (2009).

[46] P. Das, T. K. Chini, and J. Pond, J. Phys. Chem. C **116**, 15610 (2012).

[47] P. Das and T. K. Chini, J. Phys. Chem. C **118**, 26284 (2014).

[48] P. Das and T. K. Chini, J. Phys. Chem. C **116**, 25969 (2012).

[49] A. Maiti, A. Maity, and T. K. Chini, J. Phys. Chem. C **119**, 18537 (2015).

[50] P. Das, A. Kedia, P. S. Kumar, N. Large, and T. K. Chini, Nanotechnology **24**, 405704 (2013).

[51] A. Maity, A. Maiti, P. Das, D. Senapati, and T. Kumar Chini, ACS Photonics **1**, 1290 (2014).

[52] A. Maity, A. Maiti, B. Satpati, A. Patsha, S. Dhara, and T. K. Chini, J. Phys. Chem. C **120**, 27003 (2016).

[53] A. Losquin and M. Kociak, ACS Photonics **2**, 1619 (2015).

[54] C. Noguez, J. Phys. Chem. C **111**, 3806 (2007).

[55] Z. Yong, D. Y. Lei, C. H. Lam, and Y. Wang, Nanoscale Res. Lett. **9**, 1 (2014).

[56] Y. A. Akimov, W. S. Koh, and K. Ostrikov, Opt. Express **17**, 10195 (2009).

[57] K. L. Kelly, E. Coronado, L. L. Zhao, and G. C. Schatz, J. Phys. Chem. B **107**, 668 (2003).

[58] E. Ringe, J. M. McMahon, K. Sohn, C. Cobley, Y. Xia, J. Huang, G. C. Schatz, L. D. Marks, and R. P. Van Duyne, J. Phys. Chem. C **114**, 12511 (2010).

[59] M. A. Mahmoud, M. Chamanzar, A. Adibi, and M. A. El-Sayed, J. Am. Chem. Soc. **134**, 6434 (2012).

[60] L. J. Sherry, S.-H. Chang, G. C. Schatz, R. P. Van Duyne, B. J. Wiley, and Y. Xia, Nano Lett. **5**, 2034 (2005).

[61] Y. Wu and P. Nordlander, J. Phys. Chem. C **114**, 7302 (2009).

[62] E. Martinsson, M. M. Shahjamali, N. Large, N. Zaraee, Y. Zhou, G. C. Schatz, C. A. Mirkin, and D. Aili, Small **12**, 330 (2016).

[63] J. C. Maxwell-Garnett, Philosophical Transactions of the Royal Society of London. Series A **203**, 385 (1904).

[64] J. C. Maxwell-Garnett, Philosophical Transactions of the Royal Society of London. Series A **205**, 237 (1906).

[65] G. Mie, Annalen der Physik **330**, 377 (1908).

[66] A. Sánchez-Iglesias, I. Pastoriza-Santos, J. Pérez-Juste, B. Rodríguez-González, F. J. García de Abajo, and L. M. Liz-Marzán, Adv. Mater. **18**, 2529 (2006).

[67] E. M. Purcell and C. R. Pennypacker, The Astrophysical Journal **186**, 705 (1973).

[68] B. T. Draine and P. J. Flatau, JOSA A **11**, 1491 (1994).

[69] B. T. Draine and P. J. Flatau, arXiv preprint arXiv:1305.6497 (2013).

[70] U. Kreibig and M. Vollmer, in *Optical Properties of Metal Clusters* (Springer, 1995), pp. 13–201.

[71] C. F. Bohren and D. R. Huffman, Absorption and Scattering of Light by Small Particles pp. 82–129 (1983).

[72] F. Borghese, P. Denti, R. Saija, G. Toscano, and O. Sindoni, Aerosol Sci. Technol. **3**, 227 (1984).

[73] M. W. Knight, Y. Wu, J. B. Lassiter, P. Nordlander, and N. J. Halas, Nano Lett. **9**, 2188 (2009).

[74] N. S. King, Y. Li, C. Ayala-Orozco, T. Brannan, P. Nordlander, and N. J. Halas, Acs Nano **5**, 7254 (2011).

[75] J. Lerme, C. Bonnet, M. Broyer, E. Cottancin, D. Manchon, and M. Pellarin, J. Phys. Chem. C **117**, 6383 (2013).

[76] Z. Li, K. Bao, Y. Fang, Z. Guan, N. J. Halas, P. Nordlander, and H. Xu, Phys. Rev. B **82**, 241402 (2010).

[77] H. Chen, L. Shao, T. Ming, K. C. Woo, Y. C. Man, J. Wang, and H.-Q. Lin, ACS Nano **5**, 6754 (2011).

[78] P. Spinelli, C. van Lare, E. Verhagen, and A. Polman, Opt. Express **19**, A303 (2011).

[79] M.-W. Chu, V. Myroshnychenko, C. H. Chen, J.-P. Deng, C.-Y. Mou, and F. J. García de Abajo, Nano Lett **9**, 399 (2009).

[80] A. Losquin, L. F. Zagonel, V. Myroshnychenko, B. Rodríguez-González, M. Tencé, L. Scarabelli, J. Forstner, L. M. Liz-Marzán, F. J. García de Abajo, O. Stéphan, et al., Nano Lett **15**, 1229 (2015).

[81] N. Yamamoto, K. Araya, and F. J. García de Abajo, Phys. Rev. B **64**, 205419 (2001).

[82] M. Kuttge, E. J. R. Vesseur, A. Koenderink, H. Lezec, H. Atwater, F. G. de Abajo, and A. Polman, Phys. Rev. B **79**, 113405 (2009).

[83] E. S. Barnard, T. Coenen, E. J. R. Vesseur, A. Polman, and M. L. Brongersma, Nano Lett **11**, 4265 (2011).

[84] K. Yee, IEEE Transactions on antennas and propagation **14**, 302 (1966).

[85] A. Taflove, A. Oskooi, and S. G. Johnson, *Advances in FDTD computational electrodynamics: photonics and nanotechnology* (Artech house, 2013).

[86] P. B. Johnson and R.-W. Christy, Phys. Rev. B **6**, 4370 (1972).

[87] E. D. Palik, *Handbook of optical constants of solids*, vol. 3 (Academic press, 1998).

[88] D. R. Lide, *CRC Handbook of Chemistry and Physics* (CRC press, 2004).

[89] H.-Y. Wu, W.-L. Huang, and M. H. Huang, Cryst. Growth Des. **7**, 831 (2007).

[90] H.-Y. Wu, H.-C. Chu, T.-J. Kuo, C.-L. Kuo, and M. H. Huang, Chem. Mater. **17**, 6447 (2005).

[91] J. Zhang, M. R. Langille, M. L. Personick, K. Zhang, S. Li, and C. A. Mirkin, J. Am. Chem. Soc. **132**, 14012 (2010).

[92] P. Das and T. K. Chini, Curr. Sci.(Bangalore) **101**, 849 (2011).

[93] I. Pastoriza-Santos, A. Sánchez-Iglesias, F. J. García de Abajo, and L. M. Liz-Marzán, Adv. Funct. Mater. **17**, 1443 (2007).

[94] K. M. Mayer, F. Hao, S. Lee, P. Nordlander, and J. H. Hafner, Nanotechnology **21**, 255503 (2010).

[95] J. Burgin, M. Liu, and P. Guyot-Sionnest, J. Phys. Chem. C **112**, 19279 (2008).

[96] E. C. Le Ru, J. Grand, I. Sow, W. R. Somerville, P. G. Etchegoin, M. Treguer-Delapierre, G. Charron, N. Félidj, G. Lévi, and J. Aubard, Nano Lett. **11**, 5013 (2011).

[97] J. Rodríguez-Fernández, C. Novo, V. Myroshnychenko, A. M. Funston, A. Sánchez-Iglesias, I. Pastoriza-Santos, J. Pérez-Juste, F. J. García de Abajo, L. M. Liz-Marzán, and P. Mulvaney, J. Phys. Chem. C **113**, 18623 (2009).

[98] E. Ringe, J. Zhang, M. R. Langille, C. A. Mirkin, L. D. Marks, and R. P. Van Duyne, Nanotechnology **23**, 444005 (2012).

[99] J. Zhang, Y. Gao, R. A. Alvarez-Puebla, J. M. Buriak, and H. Fenniri, Adv. Mater. **18**, 3233 (2006).

[100] C. Li, K. L. Shuford, M. Chen, E. J. Lee, and S. O. Cho, ACS Nano **2**, 1760 (2008).

[101] B. J. Soller, H. R. Stuart, and D. G. Hall, Opt. Lett. **26**, 1421 (2001).

[102] M. Rycenga, M. R. Langille, M. L. Personick, T. Ozel, and C. A. Mirkin, Nano Lett. **12**, 6218 (2012).

[103] M. W. Knight, L. Liu, Y. Wang, L. Brown, S. Mukherjee, N. S. King, H. O. Everitt, P. Nordlander, and N. J. Halas, Nano Lett. **12**, 6000 (2012).

[104] D. Sikdar, W. Zhu, W. Cheng, and M. Premaratne, Plasmonics **10**, 1663 (2015).

[105] A. F. Smith, R. G. Weiner, M. M. Bower, B. Dragnea, and S. E. Skrabalak, J. Phys. Chem. C **119**, 22114 (2015).

[106] E. Ringe, C. J. DeSantis, S. M. Collins, M. Duchamp, R. E. Dunin-Borkowski, S. E. Skrabalak, and P. A. Midgley, Sci. Rep. **5** (2015).

[107] N. W. Bigelow, A. Vaschillo, J. P. Camden, and D. J. Masiello, ACS Nano **7**, 4511 (2013).

[108] J. B. Lassiter, H. Sobhani, M. W. Knight, W. S. Mielczarek, P. Nordlander, and N. J. Halas, Nano Lett. **12**, 1058 (2012).

[109] H. Zhang, M. Jin, and Y. Xia, Angew. Chem., Int. Ed. **51**, 7656 (2012).

[110] R. Jin, Y. Cao, C. A. Mirkin, K. Kelly, G. C. Schatz, and J. Zheng, Science **294**, 1901 (2001).

[111] A. G. Brolo, Nat. Photonics **6**, 709 (2012).

[112] S. Pillai, K. Catchpole, T. Trupke, and M. Green, J. Appl. Phys **101**, 093105 (2007).

[113] J.-Y. Jheng, P.-T. Sah, W.-C. Chang, J.-H. Chen, and L.-H. Chan, Dyes Pigm. **138**, 83 (2017).